



Statistical information and signal processing for the underwater internet of things

Zi Ye

► To cite this version:

Zi Ye. Statistical information and signal processing for the underwater internet of things. Networking and Internet Architecture [cs.NI]. Institut Polytechnique de Paris, 2021. English. NNT : 2021IP-PAE004 . tel-03179373

HAL Id: tel-03179373

<https://theses.hal.science/tel-03179373>

Submitted on 24 Mar 2021

HAL is a multi-disciplinary open access archive for the deposit and dissemination of scientific research documents, whether they are published or not. The documents may come from teaching and research institutions in France or abroad, or from public or private research centers.

L'archive ouverte pluridisciplinaire **HAL**, est destinée au dépôt et à la diffusion de documents scientifiques de niveau recherche, publiés ou non, émanant des établissements d'enseignement et de recherche français ou étrangers, des laboratoires publics ou privés.

Traitement statistique de l'information et du signal pour l'internet des objets sous-marins

Thèse de doctorat de l'Institut Polytechnique de Paris
préparée à l'École nationale supérieure de techniques avancées

École doctorale n°626 École Doctorale de l'Institut Polytechnique de Paris (ED IPP)
Spécialité de doctorat: Réseaux, Informations et Communications

Thèse présentée et soutenue à Palaiseau, le 11 mars 2021, par

ZI YE

Composition du Jury :

Michel Kieffer Professeur des Universités, Université Paris-Saclay	Président
Laurent Ros Professeur des Universités, Université Grenoble Alpes	Rapporteur
Emanuel Radoi Professeur des Universités, Université de Bretagne Occidentale	Rapporteur
Laurent Mortier Professeur ENSTA Paris, Institut Polytechnique de Paris	Examineur
Benoît Geller Professeur ENSTA Paris, Institut Polytechnique de Paris	Directeur de thèse

To all my family and friends

Acknowledgements

I would like to thank my supervisor Professor Benoit GELLER, for his consistent support and guidance, encouragement, and patience which allowed me to evolve throughout this thesis.

I would like to thank Professor Laurent Ros and Professor Emanuel Radoi for the time they spent on reviewing this thesis manuscript despite their numerous responsibilities.

I am honored that Professor Michel Kieffer participate in my jury and contribute to the expertise of my defense. I am also indebted to Professor Laurent Mortier for his lead in the H2020 Bridge project.

I would like to thank Doctor Tarak ARBI for the mutual cooperation and exchanges between us that improved my work.

Finally, I would like to thank all members of U2IS for the good atmosphere and serenity environment, and in particular Professor David Filliat the Head of the U2IS laboratory.

Contents

General Introduction	11
1 Underwater Propagation Environment	15
1.1 Physical Properties of the Propagation Medium	17
1.1.1 Acoustic Wave Speed	17
1.1.2 Multiple Paths - Small Scale Effects	17
1.1.3 Propagation Losses - Large Scale Effects	18
1.1.4 Noise Sources and Models	20
1.1.5 Heterogeneities and Variability of the Underwater Environment	22
1.2 Impact of Environmental Physics on Communication Signals	23
1.2.1 Optimal Frequency and Bandwidth	23
1.2.2 Doppler Effects	24
1.2.3 Impulse Response of Doubly Dispersive Channel	25
1.3 The Underwater Acoustic Channel As an Interference Channel	28
1.4 Standardization	29
1.5 Conclusion	30
2 Digital Communications over Doubly Selective Channels	31
2.1 Presentation of the Transmission Chain	32
2.1.1 Transmission on a Limited Band Channel	32
2.1.2 Quadrature Amplitude Modulation (QAM)	37
2.1.2.1 The Transmitted QAM Symbol	37
2.1.2.2 Theoretical Principle of QAM Modulation	38
2.1.2.3 Concept of the Complex Signal Envelope	38

2.1.2.4	Real QAM Modulator and Demodulator	39
2.1.2.5	Performance of the AWGN Channel	39
2.1.2.6	Soft Demapper	41
2.1.3	Orthogonal Frequency Division Multiplexing (OFDM)	42
2.2	Peak-to-Average Power Ratio (PAPR)	45
2.2.1	PAPR Reduction Techniques	47
2.2.1.1	Signal Distortion Techniques	47
2.2.1.2	Coding Techniques	48
2.2.1.3	Probabilistic Techniques	48
2.3	Effect of a Fading Channel on Communications, Diversity Techniques	49
2.3.1	Fading Channel	49
2.3.1.1	Fading Channel Model	49
2.3.2	Diversity Techniques	52
2.3.3	The Rotated Constellation	53
2.3.3.1	Operating Principle	54
2.3.3.2	Selection of the Rotation Angle	57
2.3.3.3	Demodulation Complexity	58
2.4	Equalization	60
2.4.1	Linear Equalization	60
2.4.2	Adaptive Equalization	62
2.4.3	Turbo Equalization	63
2.5	Conclusion	67
3	Signal Space Diversity for Underwater Communications	68
3.1	Uniformly Projected Rotated and Cyclic Q-delayed QAM	69
3.1.1	System Model	70
3.1.2	Properties of the Rotated Constellation with Rotation Angle $\theta = \arctan(1/\sqrt{M})$	72
3.1.3	Soft Demapper for the UP-RCQD M-QAM Constellation	73
3.1.3.1	Calculation of LLRs in the Integer Domain	74
3.1.3.2	Determination of the Global Optimum T_{opt}	75
3.1.3.3	Search for Complementary Points T_{cplm}^i	76
3.1.3.4	Summary of the Studied Soft Demapping Algorithm	76

3.1.3.5	Complexity Analysis of the Studied Soft Demapping Algorithm	77
3.1.4	Numerical Results	78
3.1.4.1	BER Underwater Performance	78
3.1.4.2	Demapper Comparison	81
3.2	Low-Complexity Blind PAPR Reduction for OFDM Systems with Rotated Constellations	83
3.2.1	Overview of the Proposed Blind PAPR Reduction Technique with SSD	83
3.2.1.1	At the Transmitter Side	83
3.2.1.2	Interleaver Estimation at the Receiver Side	85
3.2.2	Detailed Proposal and Complexity Considerations	86
3.2.2.1	Low Complexity MMSE-based Decoder	87
3.2.2.2	Low Complexity Index Estimation for the Uniformly Projected RCQD Constellations	88
3.2.2.3	Complexity Analysis	90
3.2.3	Simulation Results	91
3.3	Conclusion	95
4	Equalization techniques for the time-varying underwater acoustic channel	96
4.1	Low-Complexity Adaptive Turbo Equalization for Multipath Underwater Communication	97
4.1.1	System Model	98
4.1.2	Adaptive Turbo Equalization	99
4.1.2.1	Adaptive Equalizer Algorithm	99
4.1.2.2	Symbol to Bit Converter (SBC)	100
4.1.2.3	Bit to Symbol Converter (BSC)	101
4.1.3	Numerical Results	101
4.1.3.1	Complexity Analysis	101
4.1.3.2	WATERMARK	102
4.1.3.3	Time-varying Channels	104
4.2	Fully Adaptive Equalizer for Fast-varying Doubly Selective Channels	105
4.2.1	The Proposed Adaptive Turbo Equalizer	106
4.2.1.1	Equalizer Structure	106
4.2.1.2	Adaptive Step-size Optimization	108
4.2.2	Simulation Results	112
4.3	Conclusion	116

General conclusion	117
Résumé	119

List of Figures

1	Comparison of underwater ranges according to the channel media.	12
1.1	(a) Example of a typical speed profile of a deep sea channel. (b) Ray tracing with a source at a depth of 1500 m. black: surface and bottom reflections, blue: bottom reflection, green: surface reflection, red: direct path.	18
1.2	(a) Example of a typical speed profile of a shallow water channel. (b) Ray tracing with a source at a depth of 10 m. black: surface and bottom reflections, blue: bottom reflection, green: surface reflection	18
1.3	Propagation losses in underwater acoustic channel. (a) damping coefficient. (b) propagation losses according to equation (1.2).	20
1.4	(a) Power spectral density of noise according to the model of equation (1.6). (b) Noise power spectral density by summing the different contributions. Simplified model according to equation (1.7) with $N_0 = 50$ dB/Hz.	22
1.5	Link budget for a sinusoid signal of frequency f propagating at different distances. Simplified noise model according to equation (1.7) with $N_0 = 50$ dB.	23
1.6	(a) Optimal frequency as a function of distance. (b) 3 dB bandwidth around the optimal frequency.	24
1.7	Impulse response of an underwater acoustics channel surveyed in the Mediterranean Sea	27
1.8	Levels and frequencies of some underwater acoustics sources: anthropogenic (orange), biological (green), abiotic (red and blue)	28
2.1	Complex equivalent representation in base-band.	33
2.2	Raised cosine filter.	36
2.3	The 4-QAM Constellation.	37
2.4	QAM modulator and demodulator	40
2.5	BER for several constellations.	41

2.6	Example for the LLR calculation.	43
2.7	Spectrum of different sub-carriers.	43
2.8	An example of the squared modulus of an OFDM symbol in the time domain.	45
2.9	An OFDM symbol with a large PAPR (see the right down corner of the figure), both the actual (in red) and ideal (in blue) response for an amplifier (see the right upper corner of the figure) and finally the amplifier output (on the left upper corner of the figure).	46
2.10	$CCDF(\gamma)$ for several N_p sub-carrier values. In dotted lines, the results of Monte-Carlo simulations and in continuous lines, the results of equation (2.39).	47
2.11	Trade-off between bandwidth and symbol length.	51
2.12	The error probability as a function of SNR for several orders of diversity L	54
2.13	The classic (in blue) and rotated (in red) QPSK constellations.	55
2.14	A receiver performing turbo equalization.	63
2.15	A SISO equalizer based on MMSE equalization.	64
3.1	BICM system model with RCQD constellation	70
3.2	Uniformly projected RCQD 4-QAM signal	72
3.3	(T_I, T_Q) and the corresponding binary representation $(b_0 b_1 b_2 b_3)$ of the 16-QAM signal.	74
3.4	Example of determining the two local optima and complementary points for the UP-RCQD 16-QAM.	77
3.5	Impulse responses at times $t = 0, 1$ and 2 s of KAU2.	79
3.6	Impulse responses at times $t = 0, 1$ and 2 s of NOF1.	79
3.7	BER comparison between the studied soft demapping method and α_1 and conventional QPSK signals on KAU2 channel.	80
3.8	BER comparison between the studied soft demapping method and α_1 and conventional QPSK signals on NOF1 channel.	80
3.9	Complexity comparison of several demappers	82
3.10	BER performance of several algorithms for uniformly projected RCQD 4-QAM signal on underwater channel KAU2	82
3.11	System model.	84
3.12	Interleaver Index Error Rate comparison between the full complexity Max-Log estimator, the proposed MMSE-based detector and the method for UP-RCQD constellations for several radii r_a (16-QAM, $N = 256$ and $D = 16$).	91

3.13 BER comparison between the ideal RSI, the full complexity Max-Log estimator, the proposed MMSE-based detector and the method for several radii r_a over the Rayleigh channel ($N = 256, D = 16$).	92
3.14 Computational complexity comparison for $N_p = 256$ and $D = 16$	93
3.15 CCDFs of the PAPR for the 64-QAM constellation and $N_p = 128$	94
3.16 CCDFs of the PAPR for the 16-QAM constellation and $N_p = 64$	94
4.1 System model	98
4.2 Joint equalizer and phase estimator structure	99
4.3 BER comparison between the full complexity equalizer and the proposed one over the channel NOF1 . .	103
4.4 BER comparison between the full complexity equalizer and the proposed one over the channel BCH1 . .	103
4.5 QPSK BER comparison between the full complexity equalizer and the proposed one, with and without phase synchronization over the Rayleigh multipath channel (4.12)	105
4.6 Impulse response over the Rayleigh multipath channel (4.12) for $\epsilon_{max} = 0.005$	113
4.7 Adaptive step-size μ over the channel (4.12) for $\epsilon_{max} = 0.005$ at different iterations and for the BPSK constellation at 6 dB.	113
4.8 MSE curve over the channel (4.12) for $\epsilon_{max} = 0.005$ for the fully adaptive step-size algorithm at different iterations and for the BPSK constellation at 6 dB.	114
4.9 BER comparison over the channel (4.12) for $\epsilon_{max} = 0.005$ and for the BPSK constellation	114
4.10 BER comparison over the channel (4.12) for $\epsilon_{max} = 0.005$ and for the QPSK constellation	115
4.11 BER comparison between the fully adaptive step-size algorithm and the CS tracking one over the channel BCH1 of Watermark for the QPSK constellation.	115

List of Tables

1.1	Correspondences between wind speed (in knots), see state in Beaufort and the constant N_0 in dB/Hz. . .	21
2.1	The rotation angle values for the DVB-T2 standard.	58
3.1	The measurement parameters.	78
3.2	Comparison of the complexity of different demapping method	81
3.3	Comparison of total computational complexities (M1: Max-Log, M2: MMSE-based detector, M3: Proposal, $r_a > 0$, M4: Proposal, $r_a = 0$ and M5: ML, blind SLM).	93
4.1	Complexity comparison between the proposed sparse adaptive and the full complexity equalizers	102

List of Acronyms

ACE	Active constellation Extension
AWGN	Additive White Gaussian Noise
BER	Bit Error Rate
BICM	Bit Interleaved Coded Modulation
BSC	Bit to Symbol Converter
CA	Code Aided
CCDF	Complementary Cumulative Distribution Function
CRLB	Cramer-Rao Lower Bound
CSI	Channel State Information
DA	Data Aided
DVB-T2	Digital Video Broadcasting- Terrestrial 2
FFT	Fast Fourier Transform
IFFT	Inverse Fast Fourier Transform
ISI	InterSymbol Interference
IIER	Interleaver Index Error Rate
LLR	Log-Likelihood Ratio
LMS	Least Mean Square
LoS	Line of Sight
LTE	Long-Term Evolution
MAP	Maximum A Posteriori
MIMO	Multiple Input Multiple Output
ML	Maximum Likelihood
MMSE	Minimum Mean Square Error

MSE Mean Squared Error
MRC Maximal Ratio Combiner
NDA Non Data Aided
OFDM Orthogonal Frequency-Division Multiplexing
OoB Out-of-Band
PAPR Peak-to-Average Power Ratio
PD-DEM Per Dimension Demapper
PLL Phase-Locked Loop
PSK Phase Shift Keying
PTS Partial Transmit Sequence
QAM Quadrature Amplitude Modulation
RCQD Rotated and Cyclic Q-Delayed
RF Radio Frequency
SBC Symbol to Bit Converter
SI Side Information
SIMO Single Input Multiple Output
SISO Single Input Single Output
SLM SeLective Mapping
SNR Signal to Noise Ratio
SSD Signal Space Diversity
TCM Trellis Coded Modulation
TI Tone Injection
TR Tone Reservation
UP-RCQD Uniformly Projected - Rotated and Cyclic Q-Delayed
WiFi Wireless Fidelity
WPAN Wireless Personal Area Network
ZF Zero-Forcing

General Introduction

Scientific Context

The earth is covered with about 70% water and approximately 95% of the oceans and 99% of the seabed remain unexplored. In other words, most of our blue planet and its resources are still to be discovered. Somehow, the hostility of the undersea environment has inherently protected this secret world until recently. But the interest for the marine world, as illustrated on one side by the link between the arctic melt and the rising water and on the other side by the competition for the exploitation of undersea energetic resources, opens the ethical question of how to find a satisfying balance between the ever-increasing humankind needs and the fragility of our eco-system faced to the ever-growing human population.

Research for understanding the underwater environment and exploiting its rich resources have led to the rise of underwater exploration for first military and then scientific and economic purposes. To be able to observe, monitor, and explore the oceans, we can use seabed observatories, sensor networks, or underwater vehicles either remotely operated (Remotely Operated Vehicles - ROV), or autonomous (Autonomous Underwater Vehicles - AUV).

All these exploration and observation systems require means of communication with the surface for instrumentation and control, or for data transfer. In the submarine environment, this communication can be achieved by a wired way with means of cables (although often equipped with optical fiber); this is the case with wired observatories such as NEPTUNE (Ifremer) located on the Juan de Fuca tectonics shelf, off Canada. This is also the case for ROVs for which the umbilical is used to control the robot and retrieve the acquired data. The interest of cable communication lies in its speed (up to several PetaBits/s for intercontinental submarine cables) and its very low latency, however, its price is very high (up to 600 k€/km) and the maintenance of such systems is complex. In addition, wired communication poses serious mobility problems as observed with ROVs.

Another approach is wireless underwater communication that does not require a physical link between the transmitter and the receiver, and therefore a lower cost of installation and maintenance. However, as we will see in the following the

Type	Frequency	Range							
		10 cm	1 m	10 m	100 m	1 km	10 km	100 km	1000 km
Light	Visible	→	→	→					
Laser	Blue-green	→	→	→	→				
HF	1 MHz	→							
VHF	100 kHz	→	→						
VLF	10 kHz	→	→	→					
Sound	100 kHz	→	→	→	→				
Sound	10 kHz	→	→	→	→	→			
Sound	1 kHz	→	→	→	→	→	→		
Sound	100 Hz	→	→	→	→	→	→	→	→

Figure 1: Comparison of underwater ranges according to the channel media.

reliability and transmission rate are lower compared to wired communication. To transmit information wirelessly in an underwater environment, the classic media are Radio frequency (RF) waves, optical waves and finally acoustic waves. A comparison of the range of these different transmission media is illustrated by figure 1 [1].

RF waves are very strongly attenuated by water (on the order of 3 to 5 dB/m depending on the frequency), therefore they require high transmission power and/or large transducers. Underwater RF communications can be thus interesting for transmitting high speed (of the order of Mbit/ s) at a very short distance (up to 10 m). At higher frequencies, optical waves allow communication at very high speed (up to a few Gbit/s) but quickly undergo diffusion and absorption phenomena due to water (1 dB/m and up to 11 dB/m in turbid water) limiting the range of communication to a few tens of meters. The alignment of light beams between the transmitter and the reception is also an important issue for such communications systems. The interest in optical waves is revealed when one wants to quickly transfer a large volume of data over a short distance, especially by means of underwater robots.

Finally, acoustic waves undergo relatively low attenuation in water (of the order of 0.1 to 4 dB/km) and allow communication over relatively large distances (from a few kilometers to several hundred kilometers). This has helped make acoustic waves, the transmission vector most used in an underwater environment. Underwater Acoustic Communications are however severely disturbed by the attenuations of the acoustic waves, noise, the phenomenon of multiple paths, the temporal spreading of the channel, and finally by the Doppler effect. All these effects combined make the underwater acoustics channel unique since it is variable in time, frequency, and space thereby limiting the transmission rates (depending on frequency) at a few tens of kbit/s per kilometer. Finally, the speed of sound waves in water (around 1500 m/s depending on various physical parameters) causes significant latency in communication.

Modern techniques of underwater acoustics communications began to be developed for military purposes during the Second World War In 1945, the first submarine communication system saw the day in the United States of America in order to establish a communication link between submarines [2]. This first modem used Single Side Band (SSB)

modulation in the frequency band 8 - 11 kHz for a distance of several kilometers. Up to the end of the 1970s, other acoustic modems were referenced in the literature, all based on analogue transmission techniques which is a serious limitation faced to distortions brought by the underwater acoustic channel. From the 1980s, with the development of highly integrated electronic circuits, Very-Large-Scale Integration (VLSI) and the advent of compact DSP processors with reduced consumption, it has become possible to implement, within transmitters/ submerged receivers, complex signal processing algorithms opening up the way to digital transmission technologies. Thus, during these last forty years, considerable progress has been made in the development of acoustic modems both in terms of communication range and transmission rate.

Outline of the Thesis

In this thesis, we are interested by the scientific context of the European H2020 project called Bridges for which UME and U2IS laboratories of ENSTA Paris were both involved. In this project, a glider (a rather non-expensive AUV of less than 2 meters long) navigates and exchanges information with various sensors deployed in a circle of about less than 1 km radius. In this underwater Internet of things (IoT) context, we focalize on the digital communication problems raised by the acoustic environment and we thus keep in mind that complexity is a key issue for those autonomous energy-efficient objects.

Chapter 1 recalls properties of the underwater propagation environment. We review the degradations brought by the channel on large and small scales and their impact on the communication channels. We also illustrate the double-selectivity of the acoustic channel.

Chapter 2 is a classical chapter that synthesizes several digital communication solutions to face the channel degradations. In particular, we review the choice of a modulation scheme, the Peak-to-Average Power Ratio (PAPR) limitation, the effect of diversity on the system performance and some results about equalization.

The following chapters propose some contributions to the previous problematic. In chapter 3, we concentrate on a form of diversity called Signal Space Diversity (SSD). We suggest to apply SSD for underwater communications because it is spectrally efficient. We also propose a PAPR reduction scheme for SSD OFDM modulations.

Chapter 4 is dedicated to the equalization problem. As the channel impulse response can be very long because of the relatively low celerity of acoustic waves, we propose a sparse equalizer with joint phase recovery. We also present a fully adaptive architecture with adaptive step-size.

Finally, we summarize this work and give some concluding remarks as well as suggestions for future research.

Thesis Publications

- Zi Ye, Tarak Arbi, François-Xavier Socheleau, Benoit Geller, "Fast Soft Demapping for Underwater Acoustic Communications With Signal Space Diversity," IEEE OCEANS 2018 – Charleston , Oct. 2018.
- Zi Ye, Tarak Arbi, Benoit Geller, "Low Complexity Adaptive Turbo Equalization for Multipath Underwater Communication," IEEE OCEANS 2019 - Marseilles, June 2019.
- Tarak Arbi, Zi Ye, Benoit Geller, "Low-complexity blind PAPR reduction for OFDM systems with rotated constellations," IEEE Transactions on Broadcasting, accepted, Dec. 2020.
- Zi Ye, Tarak Arbi, Benoit Geller, "Fully adaptive equalizer for fast-varying doubly selective channels", in preparation.

Chapter 1

Underwater Propagation Environment

Contents

1.1	Physical Properties of the Propagation Medium	17
1.1.1	Acoustic Wave Speed	17
1.1.2	Multiple Paths - Small Scale Effects	17
1.1.3	Propagation Losses - Large Scale Effects	18
1.1.4	Noise Sources and Models	20
1.1.5	Heterogeneities and Variability of the Underwater Environment	22
1.2	Impact of Environmental Physics on Communication Signals	23
1.2.1	Optimal Frequency and Bandwidth	23
1.2.2	Doppler Effects	24
1.2.3	Impulse Response of Doubly Dispersive Channel	25
1.3	The Underwater Acoustic Channel As an Interference Channel	28
1.4	Standardization	29
1.5	Conclusion	30

The goal of a digital communication system is to transmit information from transmitters to receivers, in the form of symbols or binary bits, at a rate usually measured in symbols or bits per second. This transmission takes place in an environment that dictates the propagation laws of waves which carry information signals. These signals correspond to the symbols containing the information and occupy a determined bandwidth in the frequency spectrum, around one or more carrier frequencies. The physical environment is called the communication channel. Communication channels have a capacity in terms of number of symbols per second that can be transmitted with an arbitrarily low error rate.

When a communication is established through a channel, a certain physical resource of this channel is used: typically, a certain frequency band is used by a system for a certain period of time. One of the main problems when designing communications networks is the sharing of the available resources to establish reliable transmissions between each element of the network. When several non-cooperative systems compete for the use of a resource, they interfere at the expense of both their robustness and reliability.

Besides the case of very short distances (less than 100 m), electromagnetic waves are not suited to underwater communications, as the water is a conducting medium that absorbs quickly most of the transmitted energy. Differently, the physical properties of the underwater environment allow acoustic waves to propagate over long distances. Underwater acoustic waves are thus the preferred medium for communication signals in this environment. However, physics also presents itself as a factor limiting the performance of underwater acoustic communication modems which operate at very low data rates compared to radio frequency (RF) modems. These performance differences reflect the differences in orders of magnitude between some basic physical parameters of the two propagation media. For example, the ratio between the speed of the electromagnetic wave in the air and that of the underwater acoustic wave is 10^5 ($3 \cdot 10^8$ m/s against around 1500 m/s, respectively). The carrier frequency of RF communications can reach a few gigahertz (10^9 Hz), while for underwater acoustic communications, they do not exceed a few tens of kilohertz. The bandwidth in this medium is strictly limited, especially as the transmission distance increases. Consequently, the underwater acoustics communication channel is often considered to be wide-band, the carrier frequency and the width of the transmission band having the same order of magnitude. **The current performance limit of underwater acoustic modems results in a transmission rate-distance product usually less than 40 kbits/s \times km [3].** On the one hand, due to the lack of interoperability, and on the other hand, due to the lack of resources available to communicate without interference between users, the coexistence of acoustic sources of different origins in the same channel is also difficult. This, coupled with the long propagation delays, leads to difficulties in designing reliable and efficient protocols adapted to communications networks. Finally, the underwater environment presents variability and heterogeneity on several spatial and time scales, which requires flexibility and the ability to adapt underwater acoustics modems to the dynamic environment in which they operate.

The objective of the first chapter is to present in detail the particularities of the underwater acoustics environment, considered as the communication channel, in order to give the reader a better understanding of the different working hypotheses that will be presented in the following chapters. First, the important physical properties of the underwater acoustics channel are introduced, and then the distortion suffered by the underwater communication signal is explained in detail.

1.1 Physical Properties of the Propagation Medium

1.1.1 Acoustic Wave Speed

The wave speed in the medium is the basic physical parameter which determines its propagation. The speed of the underwater acoustic wave is around 1500 m/s. This means that the information delay (e.g. $D = 0.667$ s for a distance of 1 km) is large compared to the electromagnetic case. This incompressible delay is problematic for real time applications and from the network point of view. In addition, as seen in next subsection, multi-paths adds some variable delays that corresponds to relatively small fractions of D but have additional small-scale effects. One can also note that 1500 m/s is only a coarse approximation and that the underwater environment is not ISO-standard. This speed c_a varies according to the temperature, the salinity and the depth (because of the pressure) according to the relation [4]:

$$c_a = 1449.2 + 4.6T_a - 0.055T_a^2 + 0.00029T_a^3 + (1.34 - 0.01T_a)(S_a - 35) + 0.016D_a, \quad (1.1)$$

where T_a is the temperature in Celsius, S_a is the salinity (in percentage (%)) and D_a is the depth (in meters). In a water column, the velocity curve gives the relationship between sound velocity and depth. Generally, the speed of sound waves in the marine environment is between 1440 and 1540 m/s.

There is a significant difference between the velocity distribution of the deep-sea environment and the shallow-water environment. In shallow water, where the depths of the water column rarely exceed one hundred meters, the speed of sound is mainly determined by temperature. It decreases with temperature, and therefore, generally, with depth. In the deep sea, the temperature becomes low and homogeneous from a certain depth, whereas the speed of sound increases due to an increase in pressure. These differences strongly limit the propagation of sound waves, which will be explained in the next section.

1.1.2 Multiple Paths - Small Scale Effects

The underwater acoustic wave follows multiple propagation paths as it passes through the environment. This phenomenon can be explained by two physical properties: the reflection interfaces formed by the surface of the water and the seabed, and the speed varying with depth.

The reflections at the interfaces are mainly responsible for the phenomenon of multiple paths in shallow channels. The variation in celerity is similar to the variation in refractive index and from Snell-Descartes laws, it is possible to show that the rays, defined as the perpendicular directions to the wave front, tend to bend towards the region of the water column where the celerity is minimal. Refraction is the main cause of the multi-path phenomenon in the case of long

distance transmissions in a deep sea channel. In addition, the curvature of the rays can create gray areas where no acoustic energy related to the wave considered can be perceived. The effects of the various phenomena responsible for multi-path propagation are illustrated in figures 1.1 and 1.2 [4, 5].

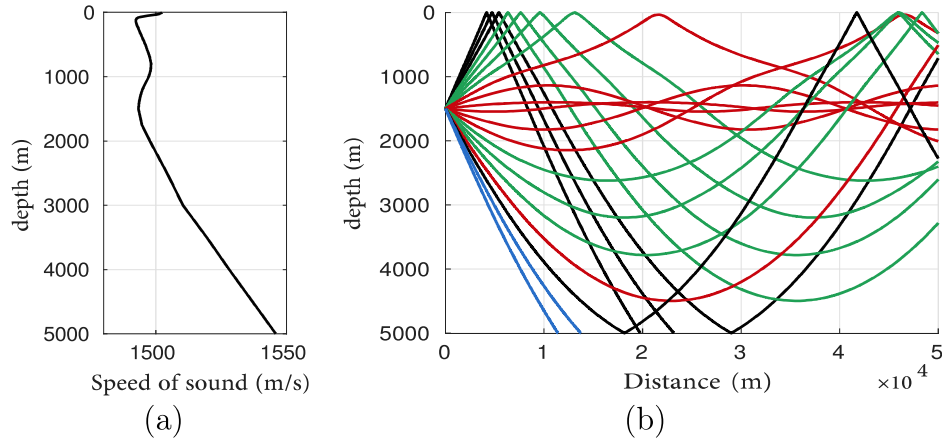


Figure 1.1: (a) Example of a typical speed profile of a deep sea channel. (b) Ray tracing with a source at a depth of 1500 m. black: surface and bottom reflections, blue: bottom reflection, green: surface reflection, red: direct path.

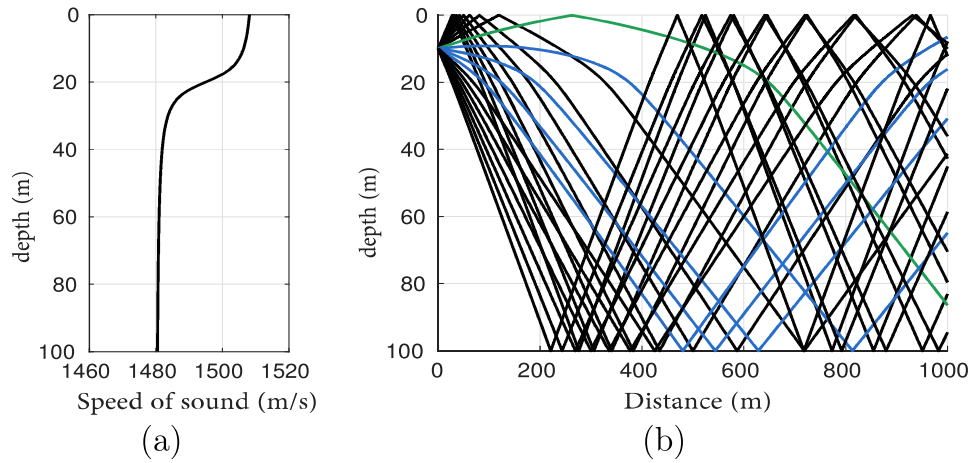


Figure 1.2: (a) Example of a typical speed profile of a shallow water channel. (b) Ray tracing with a source at a depth of 10 m. black: surface and bottom reflections, blue: bottom reflection, green: surface reflection

1.1.3 Propagation Losses - Large Scale Effects

Signal propagation in underwater acoustic channel suffers from propagation losses. This phenomenon is slowly varying when compared to the multiple paths effect of section 1.1.2 but it results in a continuous decreasing received power,

as the distance between the transmitter and the receiver becomes larger and larger, and it ultimately limits the range of the communication. These losses depend on both the frequency and the transmission distance. Frequency dependence comes from damping losses (in dB/km) which depend on the propagation medium; the distance dependence is explained by the losses caused by geometric divergence resulting from the spatial spread of acoustic energy when the wave propagates. In seawater, the attenuation of acoustic waves is due to, on one hand, the viscosity of water and the dissipation of thermal energy, and on the other hand, the quick response of chemical compounds such as boric acid [6]. These losses increase with frequency.

Assume that a signal of frequency f (in kHz) propagates in the acoustic channel along a path of length d (in meters). The propagation losses suffered by this signal (in dB), neglecting the reflection losses, are given by [7]:

$$A_{dB}(d, f) = K_d \times 10 \log_{10}(d) + 10^{-3} \times d \times \alpha_{dB}(f), \quad (1.2)$$

where K_d is a spatial dispersion factor between 1 and 2 (1: cylindrical diffusion, 2: spherical diffusion) and $\alpha_{dB}(f)$ is the damping coefficient as a function of frequency (in dB). Several models exist for this coefficient, where parameters such as salinity, water temperature and depth can be taken into account. In underwater acoustic communications, the commonly used model is that given by Thorp's formula [7, 8], that is:

$$\alpha_{dB}(f) \approx 0.11 \times \frac{f^2}{(f^2 + 1)} + 44 \times \frac{f^2}{(f^2 + 4100)} + 2.75 \times 10^{-4} \times f^2 + 0.003, \quad (1.3)$$

Figures 1.3 (a) and 1.3 (b) [5] show the influence of both the distance and the frequency of an underwater acoustic signal on the losses by diffusion and damping.

The reflections on bottoms and surfaces also lead to losses. These two interfaces are not perfectly flat and have random irregularities due to bulges and waves caused by wind and tides. A wave, in contact with an irregular surface, is reflected into a coherent specular component and a randomly distributed component in all directions. Part of the energy is also transmitted to the second medium. During the reflection, the incident wave suffers from losses in both the diffuse and transmission part, the importance of which depends on several parameters such as the state of the sea in the case of reflection on the surface, the landform of the seabed, and the sediments when reflection occurs on the seabed.

The energy loss of the reflected coherent component compared to the initial energy of the incident wave can be modeled by a reflection coefficient expressed as a function of the frequency f (in kHz), the speed c_a and the angle of incidence ψ on the ideal dioptric surface, given by [8]:

$$\tilde{R}(\psi) = \bar{R}(\psi) e^{-2 \left(\frac{2\pi f}{c_a} \sigma \right)^2 \cos^2 \psi}, \quad (1.4)$$

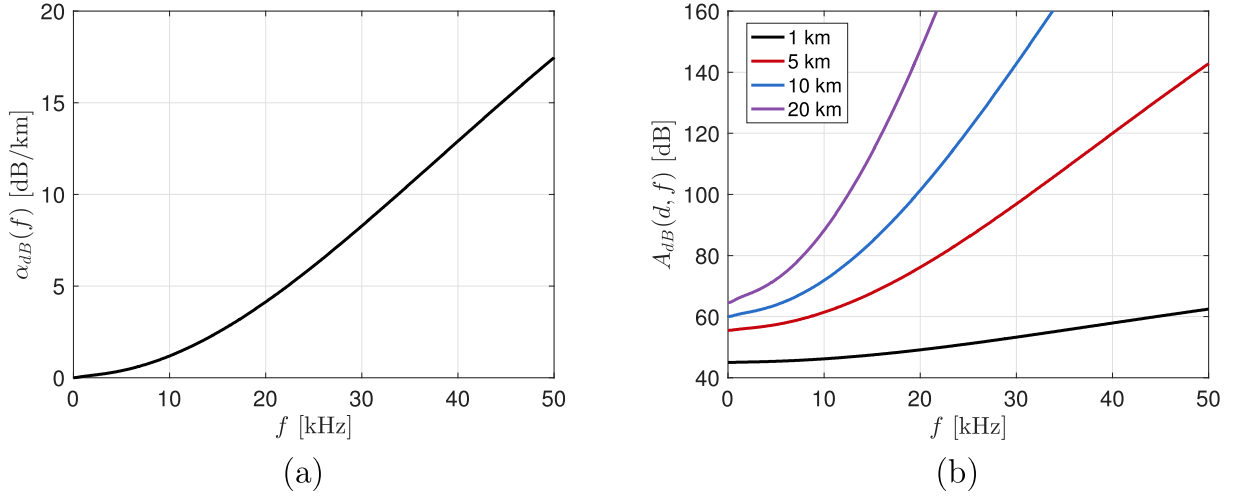


Figure 1.3: Propagation losses in underwater acoustic channel. (a) damping coefficient. (b) propagation losses according to equation (1.2).

where σ is the standard deviation of the random irregularities of the surface around the ideal diopter. $\overline{R}(\psi)$ depends on the acoustic characteristics of the water (ρ, c_a) and the second medium (ρ', c'_a) in terms of density and celerity, as well as the angle of refraction ψ' of the wave transmitted to the second medium. It is given by:

$$\overline{R}(\psi) = \frac{\rho c_a \cos \psi' - \rho' c'_a \cos \psi}{\rho c_a \cos \psi' + \rho' c'_a \cos \psi}. \quad (1.5)$$

Thus we see from equation (1.4) that the frequency of the signal also participates in losses by reflections. Its increase also contributes to reducing the ratio of the energy of the coherent specular component to the energy of the diffused component after reflection.

1.1.4 Noise Sources and Models

The underwater environment is noisy because apart from the noises caused by human activities, it is populated by many sources of sound, even in its natural state. The power spectral density of ambient noise can be described by empirical models [9–12]. In underwater acoustic communication, the model of [9] is commonly used [13]. This model offers turbulence, marine traffic, waves, and thermal noise as the main sources of ambient noise. These different contributions are each predominant in a frequency band. They are modeled by random variables whose respective power spectral densities are expressed by Hertz and in dB with respect to a pressure of $1\mu\text{Pa}$ at 1 meter from the

S_W	10	1-3	4-6	7-10	11-16	17-21	22-27
Sea state(Beaufort)	0	1	2	3	4	5	6
N_0 (dB/Hz)	44.5	50	55	61.5	64.5	66.5	68.5

Table 1.1: Correspondences between wind speed (in knots), sea state in Beaufort and the constant N_0 in dB/Hz.

source, according to the following formulas:

$$\begin{aligned}
\text{Turbulence : } N_T(f) &= 17 - 30 \log_{10}(f) \\
\text{Marine traffic : } N_S(f) &= 40 + 20(K_m - 0.5) + 26 \log_{10}(f) - 60 \log_{10}(f + 0.03) \\
\text{Waves : } N_W(f) &= 50 + 7.5\sqrt{S_W} + 20 \log_{10}(f) - 40 \log_{10}(f + 0.4) \\
\text{Thermal noise : } N_C(f) &= -15 + 20 \log_{10}(f)
\end{aligned} \tag{1.6}$$

where f is the frequency given in kHz, K_m is a factor of maritime traffic between 0 and 1, and S_W is the wind speed in m/s.

This model obviously does not take into account all possible noise sources encountered in the ocean. Biological sources (snapping of shrimps, marine mammals, etc.), for example, are neglected here. Examples of noise power spectral densities are illustrated in figure 1.4 (b) [5], and the details of different contributions of equation (1.6) are illustrated in figure 1.4 (a) [5] for several values of the wind speed and maritime traffic activity parameters. In the frequency band ranging from 100 Hz to 50 kHz, where the majority of underwater acoustics communication systems operate, the noise power spectral density can be approximated by a decreasing linear function on the logarithmic scale of frequencies [10]:

$$N_K(f) = N_0 + 18 \log_{10}(f), \tag{1.7}$$

where the frequency f is given in kHz and N_0 is a constant chosen according to the sea state. Table 1.1 gives the correspondence between the state of the sea, the wind speed and the constant N_0 of the simplified noise model. The latter model is useful for evaluating the performance of underwater acoustics communication systems by simulations when precise information about the intensity and the property of ambient noise sources is not available. You can also configure the constant N_0 according to a noise power specified in the considered transmission band.

Underwater acoustics ambient noise is often considered to be distributed according to normal law with a continuous power spectral density [8, 13]. However, it should be noted that, depending on the context, these assumptions may be in default. For example, the snapping of shrimps is rather modeled by a Lévy distribution than by a Gaussian [14], and boat noises may have power spectral density consisting of spectral lines at the rotational frequencies of the propellers and their harmonics.

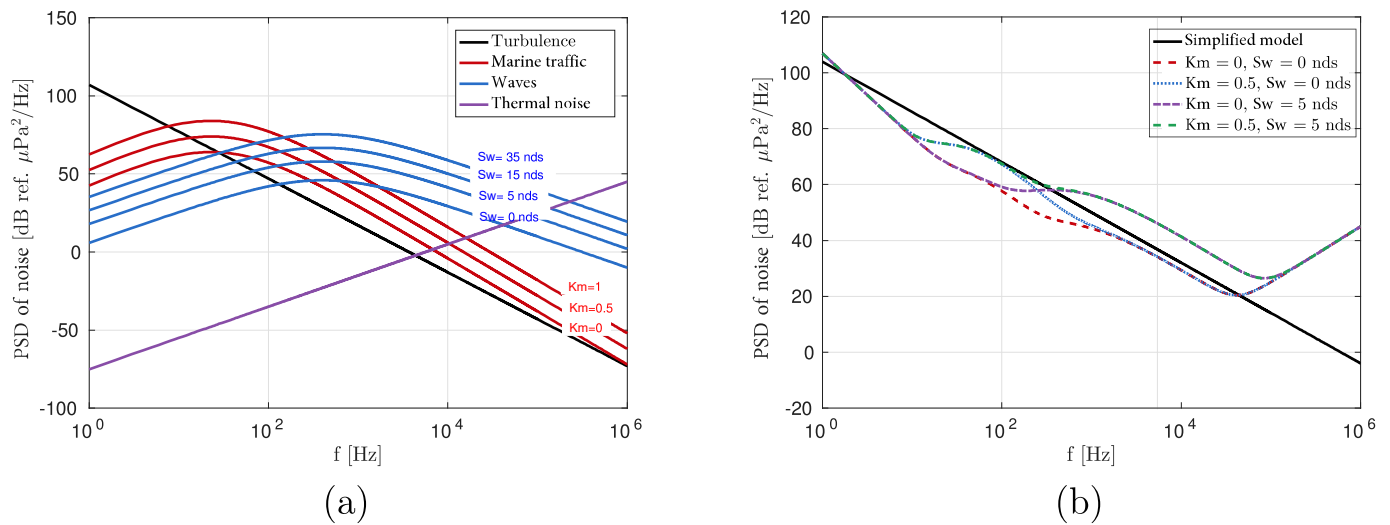


Figure 1.4: (a) Power spectral density of noise according to the model of equation (1.6). (b) Noise power spectral density by summing the different contributions. Simplified model according to equation (1.7) with $N_0 = 50$ dB/Hz.

1.1.5 Heterogeneities and Variability of the Underwater Environment

The underwater environment is heterogeneous and dynamic in essence. The physical properties that determine the propagation of acoustic waves fluctuate spatially and timely, and at different scales.

As mentioned in section 1.1.1, due to changes in temperature, salinity and pressure, the velocity curve varies according to geographic regions. Seasonal cycles and tides also decide the speed patterns, especially in shallow water due to temperature changes. The propagation conditions can therefore be very different depending on the location of the globe and the time of the year.

At more local scales, changes in propagation conditions from a source to a receiver may occur due to movements of the source and/or the receiver. These movements may be voluntary or the result of waves or drifting from the ocean current. The distortion effects produced by the propagation of the acoustic wave on the transmitted signal can vary with small variations in transmission distances and depths. The variable roughness of the bottom and surface interfaces is also a source of fluctuations in the amplitudes, phases and delays of the reflected echoes [15]. Certain more occasional phenomena cause unpredictable variations in noise levels, for example, human activity, chirping of marine mammals, or the formation of air bubbles on the surface due to waves.

From the point of view of communications theory, phenomena with time dynamics from day to season can be considered responsible for long-term variations in the signal-to-noise ratio (SNR), whose impact on the theoretical performance of the receiver is known [16, 17]. The phenomena whose variabilities occur on the symbol time, packet, or frame time scale affects the instant performance of the receiver.

1.2 Impact of Environmental Physics on Communication Signals

1.2.1 Optimal Frequency and Bandwidth

Based on the noise and propagation loss model given in the previous section, see equation (1.2) and (1.7), it is possible to establish link budget for a sinusoid signal of frequency f propagating on a path of length d [13]. Considering a direct path, the quantity $P_{dB}(d, f) = -A_{dB}(d, f) - N_K(f)$ expresses the loss in terms of signal-to-noise ratio suffered by the sinusoid in dB, where the frequency f is given in kHz and the distance d in km.

Figure 1.5 [5] illustrates several examples of this signal-to-noise ratio (SNR) as a function of frequency for different transmission distances. Several observations can be made. First, a propagation path is more selective in frequency as the distance increases. This implies that the bandwidth available for communication and therefore, the associated channel capacity decrease with distance. It then appears that there is an optimal frequency in the sense that the link budget losses are minimal for a fixed distance and transmission band. Finally, the underwater acoustics channel is generally wide-band because the width of the usable frequency band is of the same order as its center frequency.

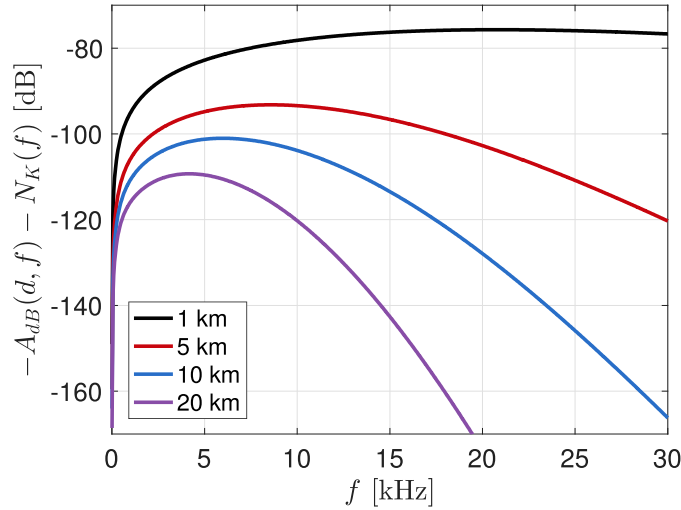


Figure 1.5: Link budget for a sinusoid signal of frequency f propagating at different distances. Simplified noise model according to equation (1.7) with $N_0 = 50$ dB.

Finally, we note that the link budget model is too optimistic to carry out realistic studies of underwater acoustics modem performance or channel capacity as detailed in the following section. In practice, one must add to the link budget, the effect of multi-path on the frequency selectivity of the channel, as well as its time variability. It is useful to give frequency bands which can be reasonably used for a fixed transmission distance. Figures 1.6 (a) and 1.6 (b) [5] show the optimal central frequency and 3 dB band, respectively, as a function of the transmission distance.

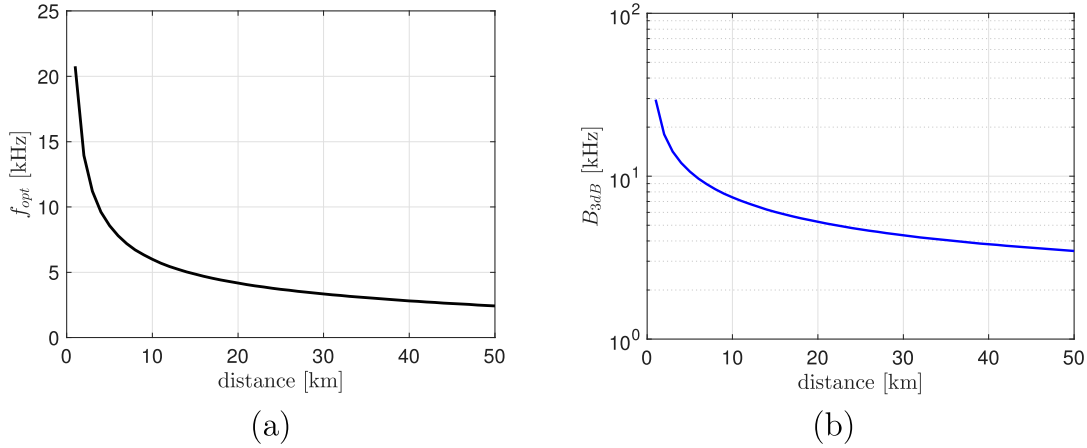


Figure 1.6: (a) Optimal frequency as a function of distance. (b) 3 dB bandwidth around the optimal frequency.

1.2.2 Doppler Effects

There are two sources of Doppler effect degradation on the communication link, namely environmental (moving waves, boats, currents...) and shifts with velocity \vec{v} of the transducers, the latter effect possibly being more important due to the relative low value of acoustic celerity ($c_m \simeq 1500$ m/s) through the parameter v/c_m . From the receiver's point of view, when it and/or the source are in motion, the low speed of underwater acoustics waves results in pronounced Doppler effects due to the perceived signal modified by the movement and speed of the terminals relatively to that of the wave. In a narrow band channel, where the carrier frequency is very large compared to the bandwidth of the signal, this effect is approximated by a simple shift in the central frequency of the received signal. In the wide-band underwater acoustics channel, this effect explicitly involves time compression/dilation of the signal by re-scaling the time variable [18]. Considering $s(t)$ as the signal from the acoustic source and $r(t)$ as the signal received after propagation through an ideal channel, only affected by the Doppler effect, we have:

$$r(t) = s((1 - \Delta)t), \quad (1.8)$$

where $\Delta = v/c_m$ is the Doppler factor, ratio (negative or positive) of the relative speed v of the movements between the source and the receiver to the speed c_m in the medium. As mentioned in the previous section, the movement of the source and the receiver can be voluntary or the result of the movement imparted to them by waves or currents.

The Fourier transform of the signal affected by the Doppler contraction/dilation effect $s((1 - \Delta)t)$ is given by $S(\frac{f}{\Delta})/|\Delta|$. Considering that the signal $s(t)$ occupies a band B around its center frequency f_c , the Doppler effect then causes a frequency dilation/compression and shift, so that it occupies a band $[-\frac{B}{2}(1 - \Delta); +\frac{B}{2}(1 - \Delta)]$ around $(1 - \Delta)f_c$.

1.2.3 Impulse Response of Doubly Dispersive Channel

A signal sent by a transmitter is received after propagation in the underwater acoustics channel, as a sum of delayed echoes whose amplitude and phase fluctuate over time (see section 1.1.2). Each echo is the result of a particular propagation path, frequency selective and whose time fluctuations reflect the marine environment. In addition, the delay of each echo is itself variable over time due to possible Doppler effects (see section 1.2.2). Mathematically summarized and using a complex baseband-equivalent model, we have the following general model for the impulse response of the underwater acoustics channel, expressed as a function of the delay τ and time t :

$$h(\tau, t) = \sum_{l=1}^K c_l(t) g_l(\tau - \tau_l(t)), \quad (1.9)$$

where K is the number of paths, $c_l(t)$ is a complex coefficient modeling the time fluctuations of the path l , $g_l(\tau)$ expresses its frequency selectivity due to absorption, and the dependency on time delay $\tau_l(t)$ reflects the wide-band characteristics of the channel and the Doppler effect. For a signal $s(t)$ transmitted through the channel $h(\tau, t)$, the received signal is expressed by :

$$r(t) = \int h(\tau, t) s(t - \tau) d\tau, \quad (1.10)$$

The channel is called time dispersive (or frequency selective) if for $s(t) = \delta(t)$, the duration of $r(t)$ is strictly positive. Conversely, a channel is frequency dispersive (or time selective) if for $s(t) = e^{j2\pi f_0 t}$, the bandwidth occupied by $r(t)$ is strictly positive. Time dispersion occurs when the number of paths K is larger than 1, while the frequency dispersion results in the time dependency of the phase, the amplitude and the delay of these paths, through the coefficients $c_l(t)$ and the delay $\tau_l(t)$. Due to the multi-path propagation of the acoustic wave and time fluctuations of the marine environment, the underwater acoustics channel is doubly dispersive.

Time fluctuations in the marine environment depend on a large number of physical parameters, which themselves vary on different time scales. It is therefore difficult to adopt a deterministic channel model. Therefore, the impulse response $h(\tau, t)$ is rather modelled as a stochastic process. When the channel can be considered as Wide-Sense Stationary Uncorrelated Scattering (WSSUS), it is possible to describe more easily how the channel disperses energy in the domain of delay and Doppler frequencies through the diffusion function [3, 19]. The diffusion function is defined as the Fourier transform of the autocovariance of the impulse channel response:

$$S_h(\tau, f) = \int R_h(\tau, u) e^{-j2\pi f u} du, \quad (1.11)$$

where:

$$R_h(\tau, u) = \mathbb{E}[(h(\tau, t) - \mathbb{E}[h(\tau, t)])(h(\tau, t + u) - \mathbb{E}[h(\tau, t + u)])^*], \quad (1.12)$$

is the autocovariance of the Wide-Sense Stationary channel with respect to time t and the time-varying impulse response $h(\tau, t)$ is defined in equation (1.9).

From this function, the Doppler spectrum can be derived:

$$S_\Delta(f) \triangleq \int |S_h(\tau, f)|^2 d\tau, \quad (1.13)$$

which characterizes the frequency dispersion of the channel, and the power-delay profile:

$$S_d(\tau) \triangleq \int |S_h(\tau, f)|^2 df, \quad (1.14)$$

that characterizes its time dispersion.

The time spread of the channel can be defined through the delay-power profile by [20]:

$$\tau_{rms} = \sqrt{\frac{\int (\tau - \tau_g)^2 S_d(\tau) d\tau}{\int S_d(\tau) d\tau}}, \quad (1.15)$$

where $S_d(\tau)$ is defined by equation (1.14) and $\tau_g = \frac{\int \tau S_d(\tau) d\tau}{\int S_d(\tau) d\tau}$. **The time spread of an underwater acoustics channel can be on the order of several tens of milliseconds for less than 1km distances and increases with the distance / depth ratio in shallow water channels [3, 13, 20].** The time dispersion of the channel is the dual phenomenon of its frequency selectivity, and knowledge of the time spread also informs us about the frequency band that can be used without suffering from ISI (see chapter 2). The channel coherence bandwidth is generally defined as the inverse of its time spread, as:

$$B_{coh} = \frac{1}{\tau_{rms}}. \quad (1.16)$$

It corresponds to an average bandwidth for which the channel can be approximated as non-frequency selective. **Considering the typical time spread of underwater acoustics channels, the corresponding coherence bandwidth can be in the order of a few hundred Hz.**

Frequency spread (or Doppler spread) is defined similarly to temporal spread, that is:

$$f_{Do} = \sqrt{\frac{\int (f - f_g)^2 S_\Delta(f) df}{\int S_\Delta(f) df}}, \quad (1.17)$$

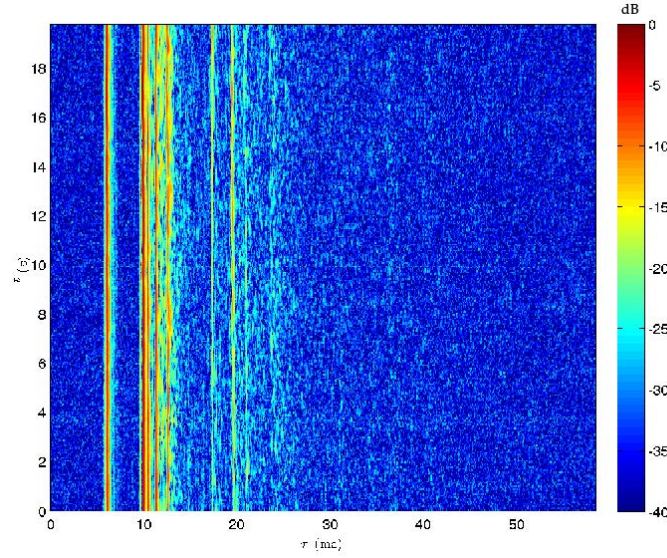


Figure 1.7: Impulse response of an underwater acoustics channel surveyed in the Mediterranean Sea

where $S_{\Delta}(f)$ is defined by equation (1.13) and $\tau_g = \frac{\int f S_{\Delta}(f) df}{\int S_{\Delta}(f) df}$. The coherence time is generally defined by:

$$T_{coh} = \frac{1}{f_{Do}}. \quad (1.18)$$

This coherence time corresponds to the average duration for which the channel can be considered as no time selective.

Typical underwater acoustics communication channels have a coherence time on the order of tens to hundreds of milliseconds, or even on the order of a second for the most stable channels [20]. When in addition, the transceivers are moving faster, the coherence time becomes smaller because of the relatively low value of the acoustic celerity (≈ 1500 m/s).

Unfortunately, the WSSUS hypothesis can be put in default by many underwater acoustics channels [20, 21] and its validity depends both on the observation time scale and the intrinsic properties of the channel; indeed, the statistics of the underwater acoustics channel can fluctuate more or less slowly, according to the phenomena of different time scales described in section 1.1.5. Finally, there is no consensus on statistical model of fading channel in the underwater acoustics communication. We can cite [21] where a Rice distribution is chosen for the fast fading model, which assumed to be stationary considering the long-term fluctuations of the channel as deterministic. These fluctuations are modelled by a log-normal distribution law in [22]. A Rayleigh distribution is chosen in [23] for the fast fading channels surveyed at sea, while other channels seem to be better modeled by a K distribution [24]. Thus, the choice of a statistical underwater acoustics channel model is still open to discussion, each real channel may be more or less close to the model depending

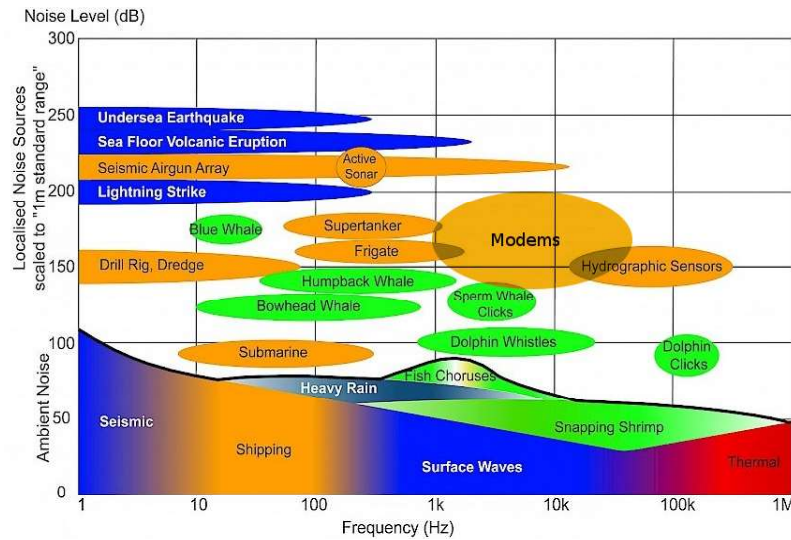


Figure 1.8: Levels and frequencies of some underwater acoustics sources: anthropogenic (orange), biological (green), abiotic (red and blue)

on where and when it was surveyed. Figure 1.7 [5] shows a channel probed in Toulon harbor (the time compression / dilation due to the Doppler effect has been compensated), at a frequency of 10.5 kHz on an 8 kHz band. This figure illustrates well the typical delay and time variability of underwater acoustics channels leading to a doubly-selective (time and frequency) medium.

1.3 The Underwater Acoustic Channel As an Interference Channel

Unlike terrestrial communication channels, the time and frequency activity of the acoustic sources occupying the underwater acoustic channel is not regulated. Many heterogeneous entities transmit their signals in similar frequency bands. In addition, there is no pre-established network infrastructure and standardized (or even commonly accepted) protocols for organizing and controlling access to the channel's physical resources. Figure 1.8 [25] shows the emission levels and frequency bands of the different underwater acoustic sources that can be encountered. When several of these sources coexist in the same geographical area, congestion of the underwater acoustic spectrum is likely to occur, and will occur more frequently as human activities linked to the world of the sea are increasing [25, 26].

1.4 Standardization

Until April 2017, the only existing standard for communication systems was the old standard NATO - STANAG 1074 for analog underwater telephones using single-sideband modulations. Recently, the JANUS digital communications protocol has been standardized by NATO [27]. This protocol aims at enabling interoperability between heterogeneous underwater acoustic systems by providing them with a framework for communication through modulation, coding, and framing. The physical layer implemented in JANUS has been designed to ensure, on the one hand, a certain robustness of the communication links and, on the other hand, an easy integration into the existing commercial modems [28]. In this first version, the standard offers a frequency-hopping spread spectrum modulator (FHSS-FSK) with 13 tone pairs distributed over a band of 4160 Hz centered on 11520 Hz. The media access layer protocol, based on carrier sense multiple access (CSMA), is also oriented towards simplicity of integration and implementation. However, it is limited in terms of the number of sources that can coexist without collisions and is sensitive to the typical long propagation delays of the underwater acoustic channel (given the low speed of the wave in the medium).

Although the standardization of JANUS is likely to mark the beginning of a new period in the development of underwater acoustic communications, the protocol does not provide all the answers to the problem of the coexistence between heterogeneous underwater acoustic sources. This is obvious for example for biological sources. Furthermore, the modulation proposed by this protocol is of limited applicability to low throughput applications or those requiring only sporadic exchange of small amount of data. The same goes for the method of access to the medium CSMA, for which the number of sources that can coexist without collision is limited. It is known that long propagation delays easily defeat this type of method, because depending on the transmission distances between users, listening to the channel before transmission can be done late or early with respect to the signals, which will conflict with the receiver receiving messages. Eventually, JANUS can be used to allow users to establish fair resource sharing before their respective transmissions. However, propagation delays can be problematic in a distributed framework, where repeating exchanges of messages between users are necessary to diffuse information on channel states perceived by each user. The centralization of this sharing in terms of a single receiver which would then send instructions to the different transmitters in the network is of limited applicability, as not all networks are centralized by nature. Finally, JANUS may suffer from a lack of adaptive capacity, in the sense that the variability of the submarine channel is not explicitly taken into account.

Generally speaking, underwater acoustic communications can be considered as non-cooperative: the emission of underwater acoustic waves can take place without great restriction, interoperability between systems of different origins is almost non-existent at present, and interference is caused and suffered unconsciously when several sources compete for the use of the physical resource offered by the channel. It is therefore very difficult to achieve effective sharing of this resource.

1.5 Conclusion

The underwater acoustic communication channel is often presented as difficult, due to its physical characteristics and the heterogeneities of the environment. These difficulties are one of the main reasons why the development of underwater acoustic communications has been slower than that of radio frequency communications, since the techniques used in this field cannot be transposed directly to the underwater environment. The widebandness of the channel, the different scales of environmental variability, as well as the lack of standardized network protocols and infrastructures for organizing access to the channel, pose great challenges. Next chapter recalls how digital communications systems try to face these challenges.

Chapter 2

Digital Communications over Doubly Selective Channels

Contents

2.1	Presentation of the Transmission Chain	32
2.1.1	Transmission on a Limited Band Channel	32
2.1.2	Quadrature Amplitude Modulation (QAM)	37
2.1.2.1	The Transmitted QAM Symbol	37
2.1.2.2	Theoretical Principle of QAM Modulation	38
2.1.2.3	Concept of the Complex Signal Envelope	38
2.1.2.4	Real QAM Modulator and Demodulator	39
2.1.2.5	Performance of the AWGN Channel	39
2.1.2.6	Soft Demapper	41
2.1.3	Orthogonal Frequency Division Multiplexing (OFDM)	42
2.2	Peak-to-Average Power Ratio (PAPR)	45
2.2.1	PAPR Reduction Techniques	47
2.2.1.1	Signal Distortion Techniques	47
2.2.1.2	Coding Techniques	48
2.2.1.3	Probabilistic Techniques	48
2.3	Effect of a Fading Channel on Communications, Diversity Techniques	49
2.3.1	Fading Channel	49

2.3.1.1	Fading Channel Model	49
2.3.2	Diversity Techniques	52
2.3.3	The Rotated Constellation	53
2.3.3.1	Operating Principle	54
2.3.3.2	Selection of the Rotation Angle	57
2.3.3.3	Demodulation Complexity	58
2.4	Equalization	60
2.4.1	Linear Equalization	60
2.4.2	Adaptive Equalization	62
2.4.3	Turbo Equalization	63
2.5	Conclusion	67

This chapter presents the general model of a digital communication chain and specifies the framework in which this thesis work was conducted.

The first section presents the components of the transmission chain and this chapter first focuses on the transmitter parameters. The digital Quadrature Amplitude Modulation (QAM) is first used as a vehicle of digital information through the transmission channel. Soft demapping is used in the rest of this work. Next part of this chapter introduces OFDM (Orthogonal Frequency Division Multiplexing) modulation and the PAPR (Peak-to-Average Power Ratio) problem is presented. The third section of this chapter illustrates how a digital communication system faces the channel degradation, the concept of diversity is introduced and the last section presents the equalization concept.

2.1 Presentation of the Transmission Chain

2.1.1 Transmission on a Limited Band Channel

Figure 2.1 [29] recalls the general structure of a digital transmission system.

- Source coding

The main purpose of source coding is to reduce the amount of information to be transmitted (compression), which consists in eliminating any unnecessary redundancy in the messages and thus maximising the entropy. The encryption of the transmitted message can also be considered as another function of source coding.

- Channel coding

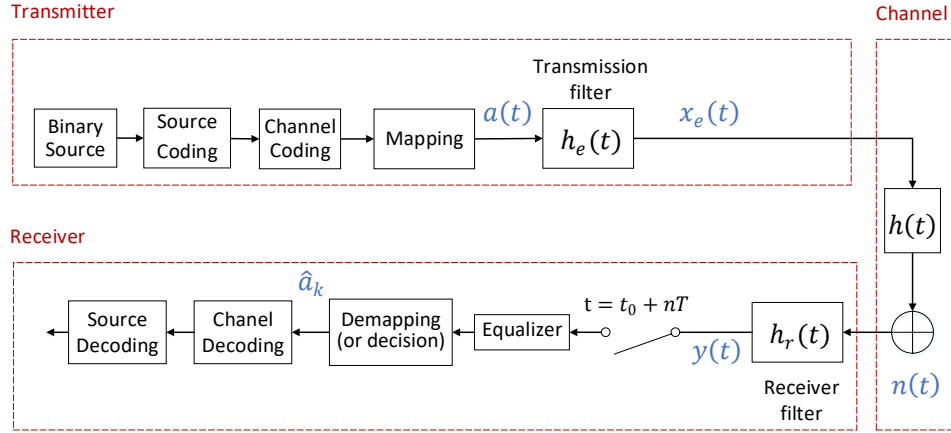


Figure 2.1: Complex equivalent representation in base-band.

The purpose of channel coding is to minimize the rate of bit error, obtained by introducing useful redundancies in the message. It is intended to combat the imperfect channel (random noise $n(t)$, fading, interference, etc.).

- Mapper

The digital message, as a series of bits, is an abstract quantity. To transmit this message, it is therefore necessary to associate it with a physical representation, in the form of a signal. This is the role of the concatenation of the mapper with the emission filter. The mapper uniquely associates a symbol denoted a_k chosen from an alphabet of $M = 2^m$ values with each binary word of m bits. At the output of the mapper, the signal $a(t)$ can be written as:

$$a(t) = \sum_k a_k \delta(t - kT), \quad (2.1)$$

where $\delta(t)$ is the Dirac function and T is the symbol period.

- Transmission filter

We convolute $a(t)$ by a pulse $h_e(t)$ to emit a continuous, band-limited signal. Typically, $h_e(t)$ is a root-raised-cosine filter, which can occupy a relatively limited bandwidth while facilitating the operation of the receiver (inter-symbol interference). After the convolution operation, the signal can be written as:

$$x_e(t) = a(t) \otimes h_e(t) = \sum_k a_k h_e(t - kT). \quad (2.2)$$

- Frequency carrier modulation / demodulation (not shown in fig. 2.1)

Several types of digital modulations can be considered for the transmission of the signal $x_e(t)$. For instance, we

consider the case of QAM (Quadrature Amplitude Modulation) modulation that will extensively be used in this work. Take the elementary case of a single carrier modulation. We know that the multiplication of $x_e(t)$ by $\exp(j2\pi f_0 t)$ (and keeping the real part) shifts the spectrum of $x_e(t)$ around $\pm f_0$. The information signal $x_e(t)$ thus modulates a sinusoidal carrier that carries energy. At the receiver side, the received signal is multiplied by the same wave $\exp(-j2\pi f_0 t)$ at the same frequency f_0 : a simple low-pass filter makes it possible to recover the transmitted signal $x_e(t)$ in the ideal case of perfect synchronization. Since these operations are transparent compared to the processes carried out in the modem (see 2.1.2.3), we only consider operations made in base-band.

- Transmission channel

The transmission channel in base-band can be considered, as a first approximation, as an invariant linear channel of impulse response $h(t)$. Ocean noise sources (see section 1.1.4) radio frequency disturbances and crosstalk can be modelled by adding random $n(t)$ noise. The components of the transmission chain also contribute to this noise. This part will be introduced in detail in section 2.3.

- Receiver filter and equalizer

Let us assume the transmission of only one BPSK symbol (i.e. $|a_0|^2$). On the receiver side, a matched filter (MF) with impulse response $h_r(t)$ maximizes the signal to noise ratio at the sampling instant $t_0 + nT$ and thus minimizes the error probability in the case of a Gaussian channel. For a Gaussian channel, (i.e. $h(t) = \delta(t)$), the optimum matched filter is defined by equation (2.3):

$$h_r(t) = h_e^*(T - t). \quad (2.3)$$

To recover this classic result, we observe that the received signal y can be written as:

$$\begin{aligned} y(t) &= (x_e(t) + n(t)) \otimes h_r(t) \\ &= x_e(t) \otimes h_r(t) + n(t) \otimes h_r(t) \\ &= X(t) + N(t), \end{aligned} \quad (2.4)$$

where $n(t)$ is the additive white Gaussian noise (AWGN). The signal power at time instant T and average noise power are given by:

$$\begin{aligned} |X(T)|^2 &= \left| \int_{-\infty}^{+\infty} X_e(f) H_r(f) e^{j2\pi f T} df \right|^2, \\ \mathbb{E}[N^2(T)] &= \frac{N_0}{2} \int_{-\infty}^{+\infty} |H_r(f)|^2 df. \end{aligned} \quad (2.5)$$

The output SNR at sampling instant T is given by:

$$SNR_o = \frac{|X(T)|^2}{\mathbb{E}[N^2(T)]} = \frac{|\int_{-\infty}^{+\infty} X_e(f) H_r(f) e^{j2\pi fT} df|^2}{\frac{N_0}{2} \int_{-\infty}^{+\infty} |H_r(f)|^2 df}. \quad (2.6)$$

Using Schwartz inequality, one simply obtains:

$$\frac{|\int_{-\infty}^{+\infty} X_e(f) H_r(f) e^{j2\pi fT} df|^2}{\frac{N_0}{2} \int_{-\infty}^{+\infty} |H_r(f)|^2 df} \leq \frac{\int_{-\infty}^{+\infty} |X_e(f) e^{j2\pi fT}|^2 df \int_{-\infty}^{+\infty} |H_r(f)|^2 df}{\frac{N_0}{2} \int_{-\infty}^{+\infty} |H_r(f)|^2 df}. \quad (2.7)$$

The equality is thus achieved in the frequency domain when $H_r(f) = [X_e(f) e^{j2\pi fT}]^*$ which is equivalent to equation (2.3). Hence, the MF maximizes the output SNR which equals to $2/N_0 \int_{-\infty}^{+\infty} |X_e(f)|^2 df$.

Indeed, at the receiver, in order to recover the value of the transmitted symbol a_k , the receiver samples the received signal at time instant $(t_0 + nT)$ as:

$$\begin{aligned} y(t_0 + nT) &= \sum_k a_k r_c(t_0 + (n - k)T) + n(t_0 + nT) \\ &= a_n r_c(t_0) + \sum_{k \neq n} a_k r_c(t_0 + (n - k)T) + n(t_0 + nT), \end{aligned} \quad (2.8)$$

where t_0 is the propagation time of the channel; in this expression, $r_c(t)$ denotes the concatenation of the shaping and reception filters with the transmission channel of impulse response $h(t)$, as summarized in equation (2.9):

$$r_c(t) = h_e(t) \otimes h(t) \otimes h_r(t). \quad (2.9)$$

Notice that $y(t_0 + nT)$ not only depends on symbol a_n , but also on other symbols. For a simple AWGN channel, that is to say $h(t) = \delta(t)$, the receiver filter eliminates ISI where $h_r(t)$ is chosen to satisfy the following condition:

$$r_c(t_0 + (n - k)T) = 0, \forall n \neq k. \quad (2.10)$$

Equation (2.10) represents the Nyquist criterion in the time domain; for the case of the AWGN channel with matched filter, this criterion can be written in the frequency domain as:

$$\sum_{n=-\infty}^{+\infty} |H_e(f - \frac{n}{T})|^2 = \text{constant}, \quad (2.11)$$

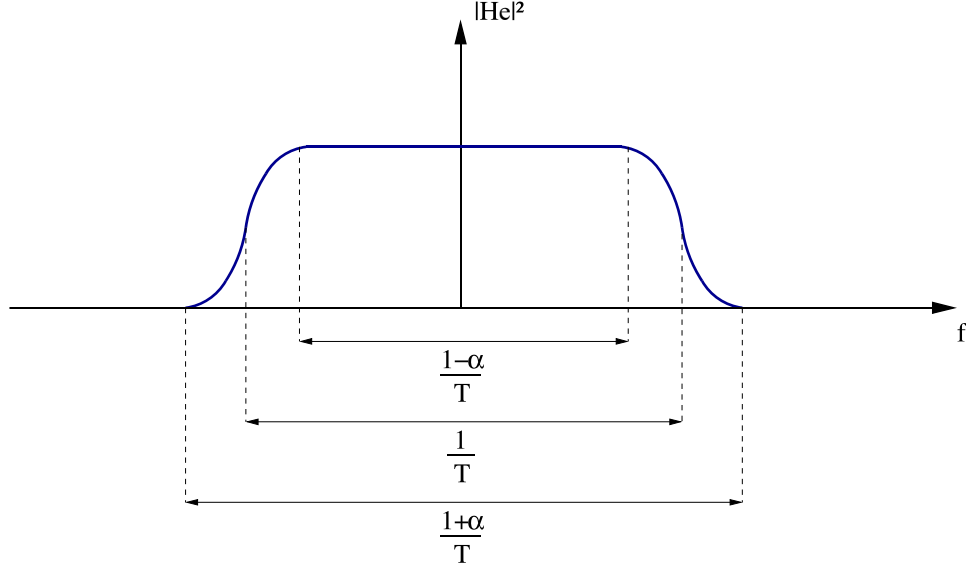


Figure 2.2: Raised cosine filter.

where $|H_e(f)|^2$ is the frequency response of the global (transmission and receiver) filter. In particular, when a root-raised-cosine filter is used as the transmission and receiver filter, the global filter (raised-cosine filter) fulfils this condition (see in Figure 2.2 [29]). This filter depends on the parameter α called the roll-off factor and is commonly used in transmission systems. For a high roll-off factor (near to 1), time synchronisation is facilitated at the expense of a large signal bandwidth. In our simulations, the roll-off factor is set at 0.3.

The AWGN channel is poorly suited to model wireless channels. Over such channels, the receiver receives many versions of the transmitted signal that arrive at distinct instants. Therefore, ISI emerge and seriously damage the system performance. To work around this issue, the receiver need to perform equalization before decoding the received signals, and the equalization function is described in detail in section 2.4.

The matched filter (MF) over the AWGN channel maximizes the signal-to-noise ratio, therefore it provides a reference for such channels and it is used as the basis for certain forms of equalization.

- Demapping

At the output of the equalizer, we obtain noisy symbols; the role of the Soft demapping is to calculate the Log-Likelihood Ratio value of the coded bits, noted LLR (see section 2.1.2.6), which will be transmitted to the soft-input soft-output channel decoder. The sign of the LLR corresponds to the hard decision on the bit considered and its absolute value represents a measure of the reliability of the decision.

- Channel decoding and source decoding

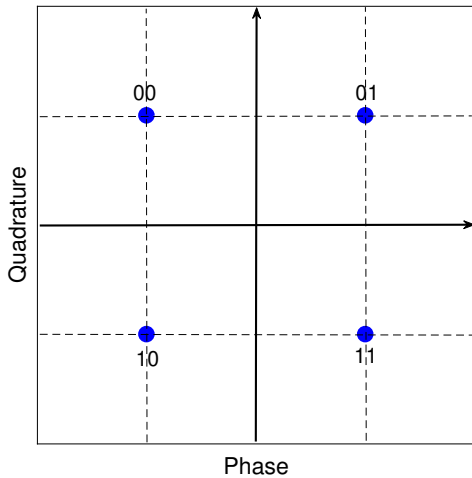
The purpose of these blocks is to perform the inverse functions of the source and channel coding to estimate the transmitted information bits.

2.1.2 Quadrature Amplitude Modulation (QAM)

As we mentioned earlier, the QAM modulation will extensively be used in this work. The presentation of some theoretical notions concerning QAM modulation is essential for understanding the modulation technique used.

2.1.2.1 The Transmitted QAM Symbol

In such a modulation system, two phase quadrature components of a carrier are each multiplied by a discrete value (data pair I_k and Q_k corresponding to the encoded bits) taken from a finite set of predefined values (constellation QAM, when assuming here a rectangular pulse of duration T for the transmit filter h_e). Then these two quadrature components are added together to build the desired QAM signal (modulated signal of duration T seconds). Each pair of values or coordinates I_k and Q_k can be represented by a point in a two-dimensional coordinate system. Figure 2.3 gives an example of a 4-QAM constellation



Phase: real part I_k of QAM symbol

Quadrature: imaginary part Q_k of QAM symbol

QAM symbol: $a_k = I_k + jQ_k$

Figure 2.3: The 4-QAM Constellation.

Note $M = 2^m$ the number of symbols in the QAM constellation; m represent the number of bits associated with a symbol of the QAM constellation.

The QAM symbol transmission rate D is then:

$$D = \frac{m}{T} \text{ bit/s.} \quad (2.12)$$

For $m > 1$, the symbol rate and thus the spectrum are reduced when compared to a binary modulation. Also, as displayed in section 2.3.1.1 "Fading channel model", the symbol duration T is a key factor on which the engineer can play to face the temporal degradation (delay spread, coherence time) of the channel. The price paid for this spectrum amelioration is a symbol error rate degradation (see section 2.1.2.3).

2.1.2.2 Theoretical Principle of QAM Modulation

Let f_c be the carrier frequency on which we want to transmit the desired QAM symbol:

$$s_k(t) = I_k \cos(2\pi f_c t) - Q_k \sin(2\pi f_c t), \quad (2.13)$$

where I_k (resp. Q_k) is the in phase (resp. quadrature) component of the QAM symbol. The QAM symbol in Equation (2.13) can be written as:

$$s_k(t) = r_k \cos(2\pi f_c t + \varphi_k), \quad (2.14)$$

where r_k and φ_k is the polar coordinate of the QAM symbol. If we consider a QAM modulation transmission of several symbols, each having a duration T , the transmitted signal becomes:

$$s(t) = \sum_k [I_k \cos(2\pi f_c t) - Q_k \sin(2\pi f_c t)] \Pi(t - kT), \quad (2.15)$$

where:

$$\Pi(t) = \begin{cases} 1, & t \in [0, T] \\ 0, & else \end{cases}. \quad (2.16)$$

2.1.2.3 Concept of the Complex Signal Envelope

Let the real signal $s(t) = \text{Re}(s_a(t))$ where $s_a(t)$ is given by:

$$s_a(t) = s(t) + j\tilde{s}(t), \quad (2.17)$$

where $\tilde{s}(t)$ is the Hilbert transform of the signal $s(t)$.

The signal in Equation (2.17) can be developed as:

$$s_a(t) = s(t) \otimes \left(\delta(t) + j \frac{1}{\pi t} \right). \quad (2.18)$$

We then have:

$$S_a(f) = \begin{cases} 2S_f, & f > 0 \\ S_f, & f = 0 \\ 0, & f < 0 \end{cases} . \quad (2.19)$$

$s_a(t)$ can be written in form:

$$s_a(t) = x_e(t) e^{j2\pi f_c t}, \quad (2.20)$$

where $x_e(t)$ is the complex signal envelope and represents the base-band signal. This notation allows to avoid modulation in the study of a transmission system. In the case of QAM modulation, the complex envelope is given by:

$$x_e(t) = \sum_k a_k \Pi(t - kT), \quad (2.21)$$

and we have:

$$s(t) = \text{Re} \left(x_e(t) e^{j2\pi f_c t} \right). \quad (2.22)$$

This representation is particularly interesting because frequency transposition by In phase / quadrature modulation can then be considered as a transparent operation to the receiver.

2.1.2.4 Real QAM Modulator and Demodulator

Figure 2.4 [29] presents a QAM modulator and demodulator scheme. In a QAM system, the two Digital-to-analog converters (DAC) deliver one pulse for each QAM symbol at a rate of $1/T$ pulses/sec. In the case of a shaping filter with rectangular response of duration T , in the frequency domain the spectrum of these pulses in $\sin(f)/f$ (sinc function) is slowly decreasing and too large (spectrum spoilage). In order to limit the signal band, other filters are most widely used in practice, such as the root-raised-cosine filter. The complex envelope of the signal can be written for a transmission filter of impulse response $h_e(t)$:

$$x_e(t) = \sum_k a_k h_e(t - kT). \quad (2.23)$$

2.1.2.5 Performance of the AWGN Channel

We consider the transmission of a QAM symbol over a AWGN channel of variance $\sigma^2 = \frac{N_0}{2} \int_{-\infty}^{+\infty} |h_r(t)|^2 dt$, where N_0 is the mono-lateral spectral density of the noise. The receiver decodes the received signal using the Maximum

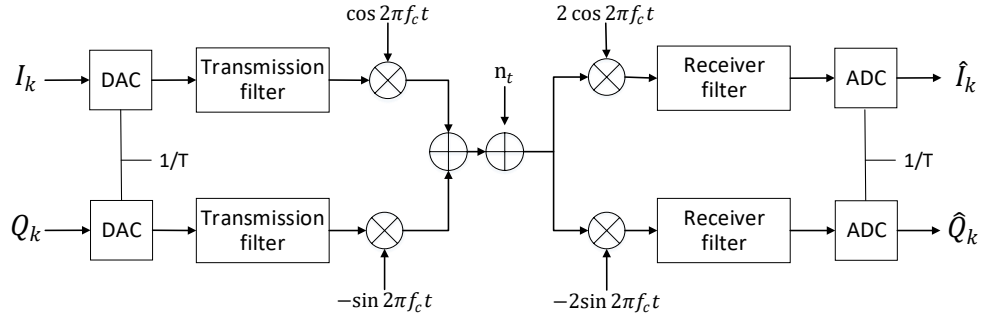


Figure 2.4: QAM modulator and demodulator

Likelihood criterion: it search the closest constellation point to the noisy received observation in terms of Euclidean distance.

Consider the case of a 2-PAM (two possible symbols $-A$ and A), the error probability for a unit energy transmission filter (given the normalisation $\int_{-\infty}^{+\infty} |h_r(t)|^2 dt = 1$ and $\sigma^2 = \frac{N_0}{2}$) is given by :

$$\begin{aligned}
 P_{es} &= \Pr(n > A) = \int_A^{+\infty} \frac{1}{\sqrt{2\pi\sigma^2}} e^{-\frac{x^2}{2\sigma^2}} dx \\
 &= \frac{1}{2} \operatorname{erfc}\left(\frac{A}{\sigma\sqrt{2}}\right) \\
 &= \frac{1}{2} \operatorname{erfc}\left(\sqrt{\frac{E_b}{2\sigma^2}}\right),
 \end{aligned} \tag{2.24}$$

where $\operatorname{erfc}(x) = \frac{2}{\sqrt{\pi}} \int_x^{+\infty} e^{-u^2} du$ and $E_b = A^2$.

For general case of M-QAM modulation, the QAM symbol error probability is [17]:

$$P_{es} = \frac{2(\sqrt{M} - 1)}{\sqrt{M}} \operatorname{erfc}\left(\sqrt{\frac{3mE_b}{4(M-1)\sigma^2}}\right), \tag{2.25}$$

and the bit error probability for Gray mapping can be approximated by:

$$P_{eb} = \frac{(0.2 + 3.6/m)(\sqrt{M} - 1)}{2\sqrt{M}} \operatorname{erfc}\left(\sqrt{\frac{3mE_b}{4(M-1)\sigma^2}}\right). \tag{2.26}$$

Figure 2.5 [17] shows the bit error rates for different QAM constellations, as a function of the signal to noise ratio. As announced in section 2.1.2.1, we can observe a degradation of the bit error rate when the number of the constellation

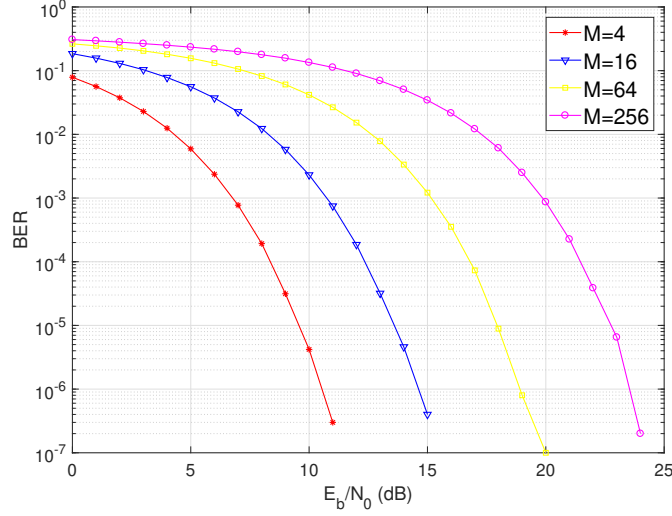


Figure 2.5: BER for several constellations.

points increases.

2.1.2.6 Soft Demapper

The soft demapping consists in calculating the LLR value, defined as:

$$\Lambda(s_i^k) = \ln \left[\frac{\Pr(s_i^k = 1 | y_k)}{\Pr(s_i^k = 0 | y_k)} \right], \quad (2.27)$$

where s_i^k is the i -th bit associated with the considered symbol and y_k is the received symbol at time instant k . The probability $\Pr(s_i^k = b | y_k)$ with $b \in \{0, 1\}$ can be developed as

$$\Pr(s_i^k = b | y_k) = \sum_{Q_m | q_i^m = b} \Pr(Q_m | y_k) \Pr(Q_m), \quad (2.28)$$

where $Q_m | q_i^m = b$ denotes the constellations symbols whose i -th bit is equal to b . We then have:

$$\Lambda(s_i^k) = \ln \left[\frac{\sum_{Q_m | q_i^m = 1} \Pr(Q_m | y_k) \Pr(Q_m)}{\sum_{Q_m | q_i^m = 0} \Pr(Q_m | y_k) \Pr(Q_m)} \right]. \quad (2.29)$$

Using the Bayes' law, for equiprobable symbols, we obtain:

$$\Lambda(s_i^k) = \ln \left[\frac{\sum_{Q_m | q_i^m=1} \Pr(y_k | Q_m)}{\sum_{Q_m | q_i^m=0} \Pr(y_k | Q_m)} \right]. \quad (2.30)$$

For a Gaussian noise, we simply have:

$$\Pr(y_k | a_k = Q_m) = \frac{1}{\pi\sigma^2} \exp\left(-\frac{|y_k - Q_m|^2}{\sigma^2}\right). \quad (2.31)$$

Using Equation (2.31), (2.27) can finally be written as:

$$\Lambda(s_i^k) = \ln \left[\frac{\sum_{Q_m | q_i^m=1} \exp\left(-\frac{|y_k - Q_m|^2}{\sigma^2}\right)}{\sum_{Q_m | q_i^m=0} \exp\left(-\frac{|y_k - Q_m|^2}{\sigma^2}\right)} \right]. \quad (2.32)$$

For example, consider for the 4-QAM constellation in Figure 2.6, the received symbol $y = 0.5 - 0.5j$, then the LLR value of the first bit of y can be calculated by:

$$\Lambda(b_1) = \ln \left[\frac{\exp\left(-\frac{|0.5-0.5j-(-1-j)|^2}{\sigma^2}\right) + \exp\left(-\frac{|0.5-0.5j-(1-j)|^2}{\sigma^2}\right)}{\exp\left(-\frac{|0.5-0.5j-(-1+j)|^2}{\sigma^2}\right) + \exp\left(-\frac{|0.5-0.5j-(1+j)|^2}{\sigma^2}\right)} \right]. \quad (2.33)$$

For $\sigma^2 = 1$, we get $\Lambda(b_1) = 2$, the sign indicates that the first transmitted bit is more likely to be equal to 1, as it could be expected when looking at figure 2.6.

2.1.3 Orthogonal Frequency Division Multiplexing (OFDM)

In order to satisfy the need for high flow rate, short bit and symbol duration are often required. As mentioned above, when T is not negligible compared to the maximum delay τ_{max} , ISI occurs, thus limits the system performance. To limit the ISI with low complexity, multi-carrier modulation was proposed. It consists in dividing the frequency band into sub-bands and simultaneously sending one part of the information on each of the available sub-carriers. This allows to have a large symbol duration T , hence, it limits the ISI while maintaining a high bit rate.

To benefit from good spectral efficiency in addition, the sub-carriers should be orthogonal, separated by $\frac{1}{T}$ (see

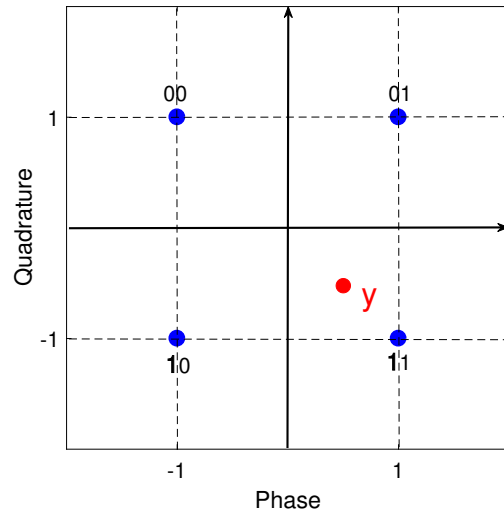


Figure 2.6: Example for the LLR calculation.

Figure 2.7 [30]). Indeed, despite the overlap between the spectrum of different sub-carriers, this allows to avoid interference between orthogonal sub-carriers. The spectrum of the different sub-carriers add up and the resulting spectrum is roughly flat in the band used, of width approximately $\frac{Np}{T}$ (ignoring side lobes at the edges) [31].

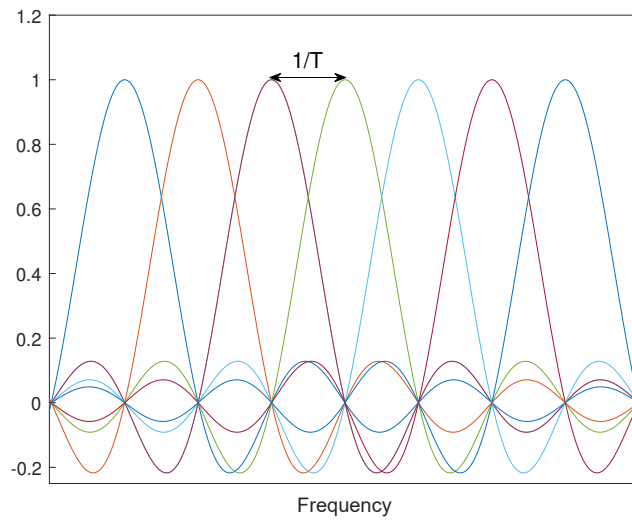


Figure 2.7: Spectrum of different sub-carriers.

During any given OFDM symbol duration, the analog base-band signal can be written as:

$$x_e(t) = \sum_{k=0}^{N_p-1} s_k e^{j2\pi \frac{kt}{T}}, \quad (2.34)$$

where N_p is the number of sub-carriers and s_k is an information symbol on the k -th sub-carrier. The occupied band is $[-f_{max}, f_{max}]$ where the maximum frequency is $f_{max} = \frac{N_p}{2T}$. With Shannon sampling theorem [32], the signal can be sampled with a frequency $f_e = 2f_{max}$ and the sampled signal is therefore written as:

$$x_e(i) = x_e\left(\frac{iT}{N_p}\right) = \sum_{k=0}^{N_p-1} s_k e^{j2\pi \frac{ki}{T}}. \quad (2.35)$$

Note that the modulation consists in simply carrying out a simple inverse discrete Fourier transform of the symbols which can be implemented efficiently by an Inverse Fast Fourier Transform (IFFT) block. Considering that each sub-carrier carries during a time of T seconds, a symbol taken among a fixed QAM constellation of size 2^m , the bit-rate is then given by:

$$D = N_p \frac{m}{T} \text{ bit/s}. \quad (2.36)$$

(2.36) generalizes (2.12) by transmitting even more bits in parallel. A cyclic prefix helps at padding the signal against inter-symbol interference and will facilitates the equalization process at the receiver. As explained below, considering a flat-fading for each sub-channel and a perfect synchronisation [33–35], the received signal discretized with the same frequency f_e is written as:

$$r(i) = r\left(\frac{iT}{N_p}\right) = \sum_{k=0}^{N_p-1} s_k h_k e^{j2\pi \frac{ki}{T}} + n(i), \quad (2.37)$$

where $n(i)$ designates the additive noise often considered as AWGN.

To recover each subchannel in parallel, the receiver reversely proceeds to a direct discrete Fourier transform of the received symbols, which can be implemented effectively by a Fast Fourier Transform (FFT); this allows to obtain for each subchannel of index k , the product $s_k h_k$ of the corresponding symbol and attenuation and then to recover the N_p symbols if the attenuations have been estimated on pilot subcarriers.

The spectral efficiency and simplicity of implementation of the OFDM using FFT, make this modulation particularly interesting for high speed communications [36]. Therefore, many telecommunications standards have adopted it such as LTE, WiFi, WPAN, DVB-T2.... Finally, note that the spectral loss due to the addition of the cyclic prefix, the out-of-band (OoB) emission due to the use of a rectangular shaping filter or the vulnerability to time or frequency synchronization

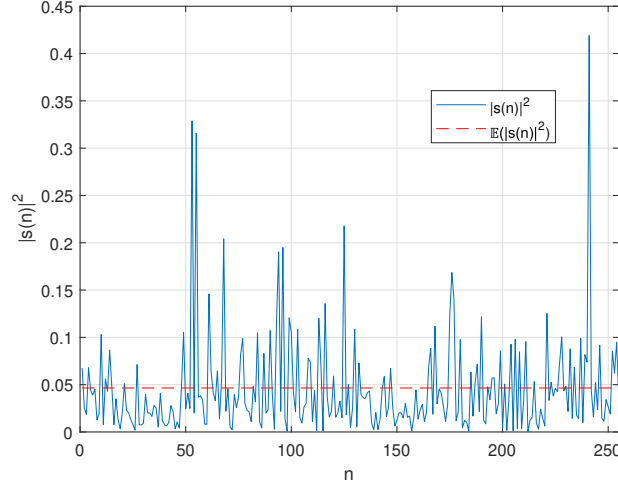


Figure 2.8: An example of the squared modulus of an OFDM symbol in the time domain.

errors has led to the emergence of alternative candidates for the implementation of multi-carrier modulations such as FBMC, UFMC, and GFDM in the literature [37].

For practical OFDM underwater communications, besides the Peak-to-Average Power Ratio problem that will be studied in the next section, the OFDM synchronization is a critical problem and OFDM is restricted to short (a few hundred meters long) line of sight communications, 20 Hz to 40 Hz being typical inter-subcarrier values.

2.2 Peak-to-Average Power Ratio (PAPR)

The OFDM signal is characterized by a strong fluctuation of the signal with large peaks over time. Indeed, since an OFDM signal is the sum of a large number of independently modulated sub-carriers (see Equation (2.35)), the resulting signal follows a distribution often considered to be near normal. This is problematic because, with large peaks, the analog amplifier must operate at a low level to prevent these peaks from reaching their saturation region (see Figures 2.8 [30] and 2.9) which results in a loss of energy efficiency and coverage. Otherwise, if the amplifier operates near its saturation region, a nonlinear distortion would appear leading to a significant loss of performance (see figure 2.9 [38]).

We can characterize the fluctuations of a signal by its PAPR; it is simply the ratio of the maximum instantaneous power to the average signal power. Thus, the PAPR is a dimensionless measurement of a waveform that indicates how wide the signal peaks are. For the discrete case, the PAPR is given by:

$$PAPR = \frac{\max_{n=0,\dots,N_p-1} |x_e(n)|^2}{\mathbb{E}(|x_e(n)|^2)}, \quad (2.38)$$

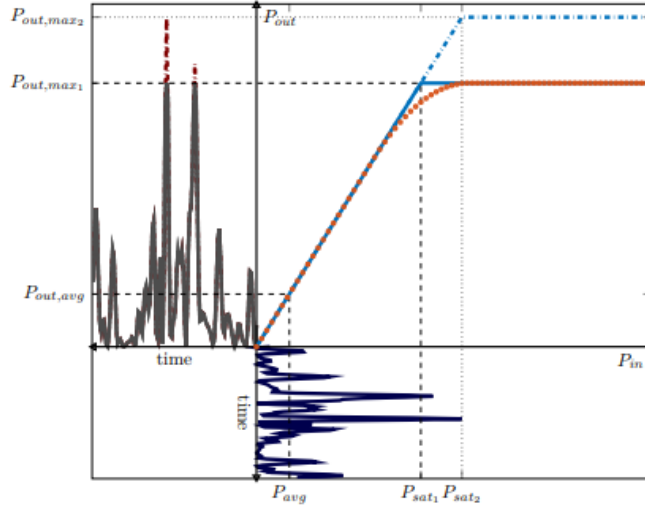


Figure 2.9: An OFDM symbol with a large PAPR (see the right down corner of the figure), both the actual (in red) and ideal (in blue) response for an amplifier (see the right upper corner of the figure) and finally the amplifier output (on the left upper corner of the figure).

where the expression of $x_e(n)$ is given by Equation (2.35) in the case of an OFDM signal.

The PAPR is generally analyzed by its Complementary Cumulative Distribution Function (CCDF), i.e. the probability that the PAPR exceeds a certain threshold γ . Assuming that the symbol s_k are independent and identically distributed (i.i.d.), therefore, the symbol $x_e(n)$ are also i.i.d and CCDF can be developed as follows:

$$\begin{aligned}
 CCDF(\gamma) &= \Pr(PAPR > \gamma) \\
 &= 1 - \Pr(PAPR \leq \gamma) \\
 &= 1 - \prod_{n=0}^{N_p-1} \Pr\left(\frac{|x_e(n)|^2}{\mathbb{E}(|x_e(n)|^2)} \leq \gamma\right) \\
 &= 1 - \left(\int_0^\gamma \exp(-z) dz\right)^{N_p} \\
 &= 1 - (1 - \exp(-\gamma))^{N_p},
 \end{aligned} \tag{2.39}$$

where the fourth line in Equation (2.39) comes from the fact that $\frac{|x_e(n)|^2}{\mathbb{E}(|x_e(n)|^2)}$ follows an exponential distribution with unit expectation (i.e. $|x_e(n)|$ follows a chi-square distribution with two degrees of freedom).

Figure 2.10 [30] compares the results of Monte Carlo simulations with the theoretical results based on the central limit approximation. We can see that the result of the simulations correspond well to the theory for $N_p \geq 64$ [38].

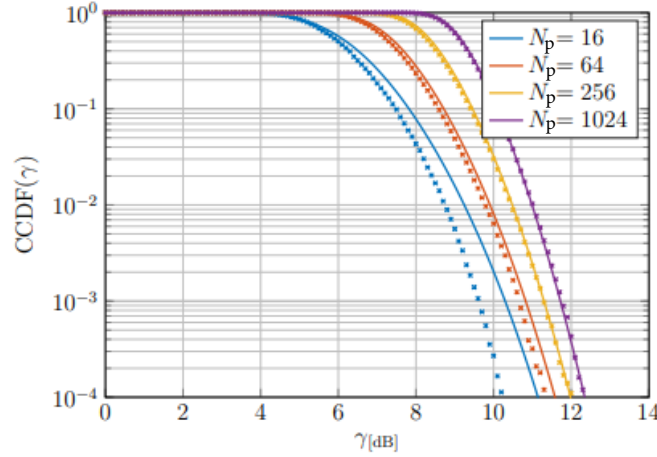


Figure 2.10: $CCDF(\gamma)$ for several N_p sub-carrier values. In dotted lines, the results of Monte-Carlo simulations and in continuous lines, the results of equation (2.39).

2.2.1 PAPR Reduction Techniques

To address the high PAPR problem, various PAPR reduction techniques have been proposed so far in the literature. These methods make it possible to reduce the PAPR at the cost of a degradation of BER performance, a loss of spectral or energy efficiency and/or an increase in computational complexity. Therefore, no technique can be suitable for all communication systems [39–42]. An appropriate method for a system should possibly meet its requirements as best as possible.

In the rest of this section, we'll briefly review the main techniques proposed. These methods can generally be classified into three main categories: signal distortion techniques, coding techniques and probabilistic techniques.

2.2.1.1 Signal Distortion Techniques

As the name suggests, these techniques intentionally introduce signal distortion in order to reduce the PAPR. The most basic method of this class is to simply replace the peaks of the OFDM signal with a predetermined value in case the peak amplitude exceeds it (clipping). The nature of the processing introduces a distortion of the signal as well as an out-of-band emission. To limit the latter, it is customary to filter the signal at the risk of seeing peaks reappear above the threshold. At the expense of high complexity, an iterative method can be used to limit out-of-band emission and ensure a desirable reduction in PAPR [43].

Contrary to clipping methods where the processing performed on the transmitter side is irreversible, other so-called compression-extension (companding) methods are proposed in the literature. Indeed, these techniques recommend

the use of a monotonic function to reduce the peak values and at the same time to increase the low values of the signal. However, the reduction of the PAPR is always achieved at the expense of a degradation of BER due to a relocation of the constellation symbols as well as an increase in the noise level during decompanding. Several techniques of compositions (companding) have been proposed in the literature such as " μ -law companding" and "exponential companding" [44–46].

2.2.1.2 Coding Techniques

The basic idea of these techniques is quite simple: it consists in choosing a subset of code words with a desirable PAPR. The input data bit blocks are then mapped to one of the pre-selected code words with a correction code (e.g. a cyclic code) [47, 48]. This method reduces the PAPR at the expense of a higher complexity on the transmitter and receiver side, as well as a reduction in spectral efficiency.

2.2.1.3 Probabilistic Techniques

Among the probabilistic methods, we first find the SeLective Mapping (SLM) algorithms [39, 42]. With this technique, the transmitter generates several possible OFDM symbols in parallel for the same information symbols block, by multiplying the symbols by different phase sequences and it chooses for transmission, the OFDM symbol with the lowest PAPR. This technique can statistically reduce the PAPR at the expense of high complexity on the transmitter side, since several IFFT blocks are required on the transmitter side, and a spectral loss because for each OFDM symbol, the phase sequence index used must be encoded and transmitted to the receiver, because the latter is essential for decoding in traditional SLM algorithms.

To avoid any spectral loss, blind SLM algorithms have been proposed in the literature [49–51]. They propose to use algorithms based on the ML criterion on the receiver side to estimate the index of the phase sequence used. The high complexity on the receiver side motivated the proposal of other detection algorithms such as the hard ML decoder and a two-step estimator based on a Viterbi algorithm followed by a verification and correction step [52].

Finally, it is important to note a saturation effect for SLM techniques, because the additional gain in PAPR decreases as the number of possible phase sequences increases.

Moreover, the principle of probabilistic interleaving techniques is quite similar to that of SLM techniques. Instead of multiplication by phase sequences, the transmitter swaps the original symbols in several ways and generates the corresponding OFDM symbols in order to transmit the one with the lowest PAPR [53]. Similar to the classic SLM technique, this method induces a spectral loss due to the emission of the index of the interleaver used by the transmitter. In order to preserve spectral efficiency [54], proposes to incorporate the interleaver index into the pilot symbols for

estimating the channel response. However, this may weaken the equalization performance on the receiver side and this technique is not suitable for the case of a slow fading channel [55].

The so-called Tone Reservation (TR) techniques sacrifice a few sub-carriers to transmit a PAPR reduction signal instead of information symbols. A good choice of this PAPR reduction signal can then reduce the peaks of the original signal and thus reduce the PAPR [56]. In addition to the loss of spectral and energy efficiency, there is also a complexity on the transmitter side in optimizing the choice of the PAPR reduction signal. By ignoring the reserved sub-carriers, the receiver decodes the information symbols without additional complexity.

The so-called Tone Injection (TI) methods consist in increasing the constellation size so that a point of the original constellation can be mapped differently. One point of the original constellation is then replaced by another in the extended constellation in order to reduce the PAPR [57]. These techniques can increase the average signal power and increase the complexity on the transmitter side.

Finally, the so-called Active Constellation Extension (ACE) methods map symbols on the outer edges of the original constellation to arbitrary positions without reducing the minimum distance between symbols. This freedom of mapping can be exploited to reduce the PAPR [58]. Unlike Tone Injection techniques, the increase in average signal power with ACE is smaller. However, the performance in terms of PAPR reduction decreases as the constellation size increases due to the nature of ACE.

2.3 Effect of a Fading Channel on Communications, Diversity Techniques

2.3.1 Fading Channel

2.3.1.1 Fading Channel Model

Fading can be classified based on their temporal and frequency characteristics which characterize the channel selectivity in two dimensions.

- Temporal characteristics

Fading can be divided into slow fading and fast fading. The terms slow and fast fading refer to the rate at which the magnitude and phase changes.

Slow fading occurs when the coherence time of the channel is large compared to the signal symbol period. In this case, the amplitude and phase changes can be considered to be approximately constant over the transmission period. Slow fading can for instance be caused by events such as shadowing, where a large obstruction such as a hill or large building obscures the main signal path between the transmitter and a slowly moving receiver. From the

digital communication point of view, it is often considered that $T_{coh} \geq 10^3 T$ is sufficient to consider the fading as slow. However, in addition, it is often necessary that the channel must be considered as stable within a frame, that is N consecutive symbol durations for a single carrier system, because in practice, the channel is often estimated only once during the training period (i.e. a fraction of few tens consecutive symbols).

On the contrary, fast fading arises when the coherence time of the channel cannot be considered as small compared to the signal symbol period. In practice, digital communications performances are degraded by fast fading when $T > \frac{T_{coh}}{1000}$; that is $f_{Do}T > 10^{-3}$ when the channel variation begins to be perceived within a fraction of the symbol duration.

- Frequency characteristics

Fading can also be classified into flat fading and frequency selective fading according to the multi-path effect of the wireless channel. Generally, multi-path signals arrive at the receiver at different times, and if the maximum delay is negligible compared to the symbol period (the coherent bandwidth of the channel is larger than the bandwidth of the transmitted signal), it can be considered that multi-path signals arrive at the receiver almost simultaneously. In this case, multi-path does not cause any significant ISI. It is often considered that this favorable case occurs when $T \geq \frac{\tau_{rms}}{10}$.

Conversely, if the maximum delay of multi-path signals is not negligible compared to the symbol period, symbols arriving at different times overlap, causing ISI. This fading is then called frequency selective fading, because the frequency response of this channel is not flat in the frequency band used. An equalizer is often needed to face this issue, as studied in the last section of this chapter.

To summarize, the wireless channel can be classified into 4 different cases according to the relative value of the symbol duration T compared to the timing characteristics of the channel (coherence time and delay spread):

- Slowly flat fading (simple equalization)
- Fast flat fading (difficult)
- Slowly frequency-selective fading (difficult)
- Fast frequency-selective fading (doubly selective: very difficult)

In particular, OFDM allows a degree of freedom by choosing an intercarrier bandwidth preventing frequency distortion but the symbol duration is still restricted by the time selectivity (see figure 2.11 [59]).

- Some well known models

Fading channel models are classically used to model the effects of electromagnetic transmission of information over the air in cellular networks and broadcast communication. The classic statistical models for wireless communication channel are the Rayleigh fading and the Rician fading models.

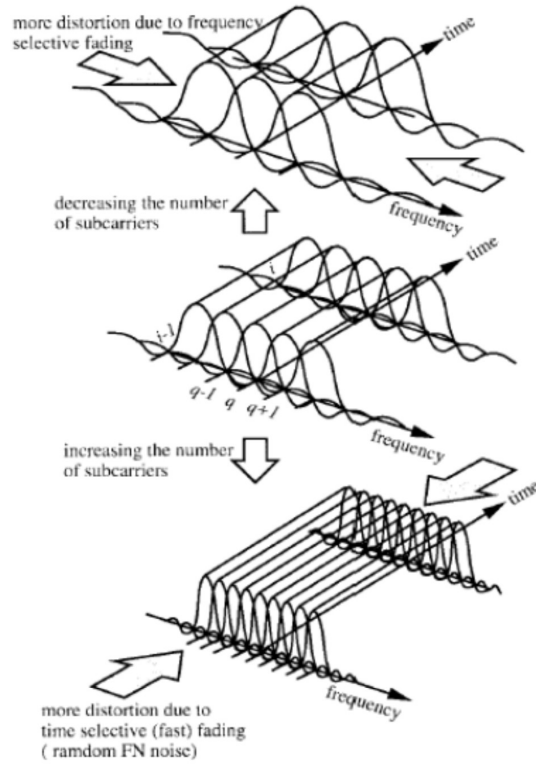


Figure 2.11: Trade-off between bandwidth and symbol length.

Rayleigh fading assumes that there is no line of sight between the transmitter and the receiver and that many (almost simultaneous) paths interfere.

According to central limit theorem, with a high number of multi-paths, the impulse response $h(\tau; t)$ is modeled as a complex-valued Gaussian process with zero-mean and variance $\sigma_{Rayleigh}^2$. Equivalently, the phase obeys a uniform distribution in 0 to 2π , and the envelope $|h(\tau; t)|$ at any instant t is Rayleigh-distributed. The probability density function of the Rayleigh distribution is:

$$f(z) = \frac{z}{\sigma_{Rayleigh}^2} e^{-\frac{z^2}{2\sigma_{Rayleigh}^2}}, z > 0. \quad (2.40)$$

In addition one can note that in 3GPP modes, one often finds channel models that consider several independent Rayleigh fading models that affect independently several consecutive symbols (frequency selective channel).

If, in addition to the signals received by reflection, refraction, scattering, etc., there is signal directly arriving from the transmitter to the receiver in the received signal, then the total signal strength obeys the Rician distribution. The Rician distribution can actually be understood as the sum of the main signal and the multi-path signal components that obey the Rayleigh distribution. The probability density function of the Rician distribution is:

$$f(z) = \frac{z}{\sigma_{Rician}^2} e^{-\frac{z^2 + A_p^2}{2\sigma_{Rician}^2}} \cdot I_0\left(\frac{zA_p}{\sigma_{Rician}^2}\right), z > 0, \quad (2.41)$$

where A_p is the peak value of the main signal amplitude, σ_{Rician}^2 is the power of the multi-path signal component, I_0 is the modified Bessel function of the first kind with order zero. There is no agreement among the ocean research community for a general model. Note that the Rayleigh fading is the most defavorable case as there is no direct path and therefore it is often chosen as the reference for the worst case.

2.3.2 Diversity Techniques

Diversity technique is widely used to combat random fading; the idea of this technique is to send various copies of the information symbols over independent fading channels. As there is a limited probability that all the attenuation of these channels are simultaneously below a critical threshold, this ensures that reliable communication can be carried out.

In the literature, several techniques to provide the receiver with L independent fading replicas of the signal carrying the same information have been proposed. For instance [60]:

- time diversity : the signal is transmitted at L different time instants, separated by at least the coherence time T_{coh} of the channel.
- frequency diversity : the signal is transmitted on L different carriers, separated by at least the coherence bandwidth B_{coh} of the channel.
- spacial diversity : the information is sent and/or received L times over several sufficiently separated antennas in space (of the order of a few wavelengths in practice).

In chapter 3, we will see that rotated constellation also allows to achieve diversity. All these techniques can be considered as a simple repetition code. All received versions can then be combined on the receiver side in a coherent way in order to increase the signal to noise ratio with the Maximal Ratio Combiner (MRC).

We now analyse the bit error rate for this technique. The received signal on the L independent flat channels can be written in vector form as:

$$\mathbf{r} = \mathbf{h}\mathbf{s}_1 + \mathbf{n}, \quad (2.42)$$

where $\mathbf{h} = [h_1, h_2, \dots, h_L]^T$, $\mathbf{r} = [r_1, r_2, \dots, r_L]^T$ and $\mathbf{n} = [n_1, n_2, \dots, n_L]^T$ are respectively the channel attenuation, the received observation and the Gaussian noise vector.

Consider BPSK modulation, with $s_1 = \pm a$ on L independent Rayleigh channels. Suppose the channel attenuations h_l are known to the receiver. By combining received observations with a MRC, we get:

$$\frac{\mathbf{h}^*}{\|\mathbf{h}\|} \mathbf{r} = \|\mathbf{h}\| s_1 + \frac{\mathbf{h}^*}{\|\mathbf{h}\|} \mathbf{n}. \quad (2.43)$$

The instantaneous error probability for the AWGN channel can simply be derived as [17]:

$$P_{err}|\mathbf{h} = \text{erfc} \left(\sqrt{2 \|\mathbf{h}\|^2 \text{SNR}} \right), \quad (2.44)$$

where $\text{SNR} = a^2/N_0$ is the signal-to-noise ratio, whereas $\|\mathbf{h}\|^2 \text{SNR}$ is the instantaneous SNR. To obtain the average error probability, we need to calculate the expectation over the fading attenuation of equation (2.44) over all values of $\|\mathbf{h}\|^2$. For Rayleigh channels, with unit variances, we obtain [61]:

$$P_{err} = \left(\frac{1 - \sqrt{\frac{\text{SNR}}{1+\text{SNR}}}}{2} \right)^L \sum_{l=0}^{L-1} \binom{L-1+l}{l} \left(\frac{1 + \sqrt{\frac{\text{SNR}}{1+\text{SNR}}}}{2} \right)^l, \quad (2.45)$$

where $\binom{L-1+l}{l}$ is the binomial coefficients.

At high SNR, the probability P_{err} can be approximated by:

$$P_{err} \approx \binom{2L-1}{L} \frac{1}{(4\text{SNR})^L}. \quad (2.46)$$

It is therefore clear that the order of diversity L has a great impact on the performance of the communication on such a fading channel. Instead of the traditional exponential BER decrease of the AWGN channel with the SNR, the decrease of the BER is only inversely proportional to $(\text{SNR})^L$ (i.e. inversely proportional to SNR if there is no diversity). Increasing L dramatically decreases the error probability (see Figure 2.12 [61]). Finally, other methods to increase diversity can be found in the literature, such as spread spectrum, channel coding with Bit-Interleaved Coded Modulation (BICM) and precoding technique [17, 60].

2.3.3 The Rotated Constellation

In chapter 3, we will study a form of diversity called signal diversity (or rotated constellations) which has the advantage of being implicitly included in the transmitted signal, without having the drawback of explicit repetition (as for diversity such as frequency, time, space...).

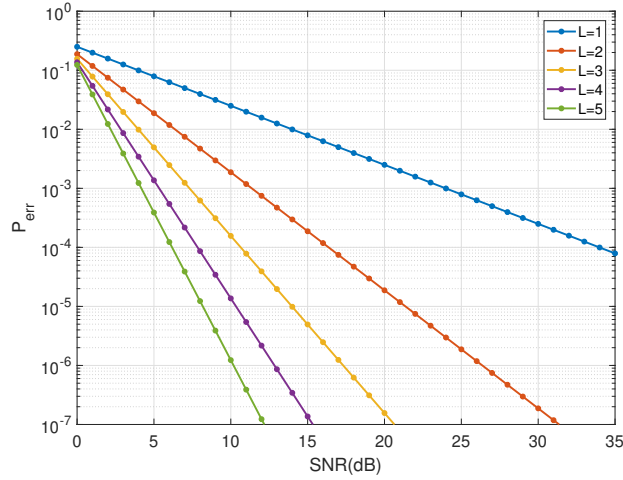


Figure 2.12: The error probability as a function of SNR for several orders of diversity L .

2.3.3.1 Operating Principle

The diversity techniques discussed in subsection 2.3.2 can be seen as one form of repetition code. [62–65] propose another more sophisticated form of coding known as Signal Space Diversity (SSD), which inherently increases diversity. This diversity allows a coding gain on selective fading channels and thus a gain in performance without compromising the spectral and energy efficiency of the communication system, though there might be some loss due to some residual interference between the channels [30, 66]. To do this, the first step consists of a simple rotation of the classical constellation noted \mathbb{S} by a rotation angle θ . The symbols of the rotated constellation are then given by:

$$x = \mathbf{R} \begin{bmatrix} s_1 \\ s_2 \end{bmatrix}, \quad (2.47)$$

where \mathbf{R} is the rotation matrix:

$$\mathbf{R} = \begin{bmatrix} \cos \theta & -\sin \theta \\ \sin \theta & \cos \theta \end{bmatrix}, \quad (2.48)$$

and $\theta \in [0, 2\pi]$ is a rotation angle. The rotation by itself does not allow again in diversity, however, it is essential to transmit the components x_1 and x_2 of a rotated symbol x on two independent channels, for example, to exploit frequency diversity on a frequency selective channel; this diversity could not be exploited if the symbols were not rotated before transmission. To better illustrate the operating principle, consider the classical QPSK constellation. The

corresponding rotated symbols are given by:

$$x_A = \mathbf{R} \begin{bmatrix} a \\ a \end{bmatrix}, \quad x_B = \mathbf{R} \begin{bmatrix} -a \\ a \end{bmatrix}, \quad x_C = \mathbf{R} \begin{bmatrix} -a \\ -a \end{bmatrix}, \quad x_D = \mathbf{R} \begin{bmatrix} a \\ -a \end{bmatrix}. \quad (2.49)$$

The received signal is written as:

$$r_i = h_i z_i + n_i, \quad i = 1, 2, \quad (2.50)$$

where z denotes the transmitted symbol, h_1 (resp. h_2) represents the fading coefficient of the in-phase component z_1 (resp. in quadrature z_2) and n_i is a white Gaussian noise of variance N_0 .

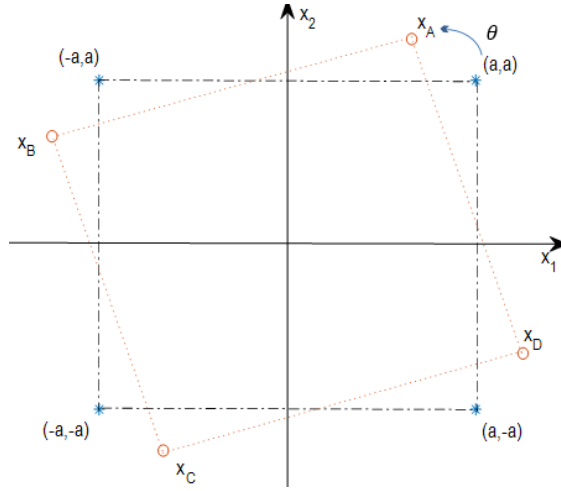


Figure 2.13: The classic (in blue) and rotated (in red) QPSK constellations.

Unlike the classical constellation (not rotated), each symbol of the rotated constellation has its own in-phase component and its own quadrature component (see figure 2.13 [30]), distinct from the other components of all other points (in red) of the constellation. If one of these two components is erased by the channel, it is lost with the classical constellations, while the receiver could still find all the information (in phase and in quadrature) with the rotated constellations, since the only component received carries both the original phase and quadrature information and uniquely identifies a symbol of the classical constellation.

To better understand the modulation diversity, we examine the error probability below [61]. Suppose the symbol x_A is transmitted; the probability of error can be upper-bounded with the union bound:

$$P_e \leq \Pr \{x_A \rightarrow x_B\} + \Pr \{x_A \rightarrow x_C\} + \Pr \{x_A \rightarrow x_D\}. \quad (2.51)$$

The conditional probability $\Pr \{x_A \rightarrow x_B \mid h_1, h_2\}$ is written as:

$$\Pr \{x_A \rightarrow x_B \mid h_1, h_2\} = \text{erfc} \left(\sqrt{\frac{h_1^2 (x_{A1} - x_{B1})^2 + h_2^2 (x_{A2} - x_{B2})^2}{2N_0}} \right) = \text{erfc} \left(\sqrt{\frac{SNR (h_1^2 d_1^2 + h_2^2 d_2^2)}{2}} \right), \quad (2.52)$$

where $SNR = a^2/N_0$ and:

$$d = \begin{bmatrix} d_1 \\ d_2 \end{bmatrix} = \frac{1}{a} (x_A - x_B) = \begin{bmatrix} 2 \cos \theta \\ 2 \sin \theta \end{bmatrix}. \quad (2.53)$$

Using inequality $\text{erfc}(x) \leq \frac{1}{2} e^{-\frac{x^2}{2}}$ [67] and then by making the expectation with respect to h_1 and h_2 , assuming that these two variables are independent and follow Rayleigh's law with unit variance, we obtain [61]:

$$\Pr \{x_A \rightarrow x_B\} \leq \left(\frac{1}{1 + SNR (d_1^2/4)} \right) \left(\frac{1}{1 + SNR (d_2^2/4)} \right). \quad (2.54)$$

For $\theta \neq [0, \frac{\pi}{4}]$ (so that $d_1 \neq 0$ and $d_2 \neq 0$), we can rewrite Equation (2.54) for a high SNR:

$$\Pr \{x_A \rightarrow x_B\} \leq \frac{16}{\delta_{AB}} SNR^{-2}, \quad (2.55)$$

where δ_{AB} is the so-called product distance between x_A and x_B and is written as:

$$\delta_{AB} = (d_1 d_2)^2. \quad (2.56)$$

Similarly, we obtain $\Pr \{x_A \rightarrow x_C\}$ and $\Pr \{x_A \rightarrow x_D\}$. We can finally rewrite Equation (2.51) :

$$P_e \leq \frac{48}{\min_{j=B,C,D} \delta_{Aj}} SNR^{-2}. \quad (2.57)$$

It is therefore clear that for any indexes i and j , $\delta_{ij} > 0$ and the diversity obtained by rotation is equal to 2. Several rotation angles make it possible to obtain a diversity equal to 2. In the next section, we examine the criteria proposed in the literature for the selection of the rotation angle.

2.3.3.2 Selection of the Rotation Angle

The rotation angle determines the performance of the system, it must therefore be chosen wisely [61, 63, 64, 68–73]. In the literature, some criteria have been proposed for this purpose. First, Equation (2.57) suggests that the optimal angle is the one which maximizes the minimum product distance between the symbols of the rotated constellation χ :

$$\theta = \arg \max_{\alpha} \left[\min_{x, y \in \chi} \prod_{i=1}^2 |x_i - y_i| \right]. \quad (2.58)$$

Regardless of the size of the constellation, this criterion leads to the angles of the golden number [63]:

$$\theta_1 = \arctan \left(\frac{1 \pm \sqrt{5}}{2} \right). \quad (2.59)$$

The high number of neighbors at the minimum product distance called "kissing number" can make the choice of θ_1 sub-optimal. An alternative criterion is to study the probability of an average symbol error [69, 70]:

$$P_s(\theta_i) \leq \frac{1}{|\chi|} \sum_{x \in \chi} \Pr(x) \sum_{\hat{x} \neq x \in \chi} \Pr\{x \rightarrow \hat{x}\}, \quad (2.60)$$

where $|\chi|$ is the constellation size; $\Pr\{x \rightarrow \hat{x}\}$ can be upper-bounded in the following expression which generalize Equation (2.54):

$$\Pr\{x \rightarrow \hat{x}\} \leq \frac{1}{2} \prod_{i=1}^2 \frac{1}{1 + \frac{(x_i - \hat{x}_i)^2}{8N_0}}. \quad (2.61)$$

Minimizing Equation (2.60) by a gradient descent algorithm, [69] then proposes some rotation angles for the QPSK, 8-PSK and 16-QAM constellations on a Rayleigh channel.

In addition, other criteria have been considered in the literature such as the minimum squared Euclidean distance between the components of rotated symbols, the average Hamming distance between neighboring symbols in terms of product distance, the maximization of the BICM capacity and the capacity of coded modulation [71–73]. In addition, rotation angles have also been proposed to give the best performance on a Rice and Nakagami channel and for a BICM-ID system [74–77].

Finally, the DVB-T2 standard recommends the use of a rotation angle for each constellation size [78, 79]. They are summarized in Table 2.1. There is therefore no optimum rotation angle in all cases because they depend on the modulation, the channel and the coding scheme, however it should be remembered that it is generally necessary to carry out preliminary simulations which can avoid certain less favorable angles while many rotation angles allow fairly

QPSK	16-QAM	64-QAM	256-QAM
29°	16.8°	8.6°	3.3°

Table 2.1: The rotation angle values for the DVB-T2 standard.

close performances.

2.3.3.3 Demodulation Complexity

The soft demapping process involves calculating the LLR value for each bit:

$$\begin{aligned}
\Lambda(l^i(x)) &= \log \left(\sum_{x \in \mathcal{X}_0^i} \Pr(r | x, h) \right) - \log \left(\sum_{x \in \mathcal{X}_1^i} \Pr(r | x, h) \right) \\
&= \log \left(\sum_{x \in \mathcal{X}_0^i} \exp \left\{ - \left(\frac{|r_1 - h_1 x_1|^2}{\sigma^2} + \frac{|r_2 - h_2 x_2|^2}{\sigma^2} \right) \right\} \right) \\
&\quad - \log \left(\sum_{x \in \mathcal{X}_1^i} \exp \left\{ - \left(\frac{|r_1 - h_1 x_1|^2}{\sigma^2} + \frac{|r_2 - h_2 x_2|^2}{\sigma^2} \right) \right\} \right),
\end{aligned} \tag{2.62}$$

where $l^i(x)$ represents the i -th bit of the symbol x , h is the channel vector (h_1, h_2) , σ^2 denotes the noise variance by dimension, \mathcal{X}_0^i (resp. \mathcal{X}_1^i) designates the set of symbols of the rotated constellation whose i -th bit is equal to 0 (resp. 1), and x_1 (resp. x_2) denotes the in-phase (resp. quadrature) component of the symbol x .

A soft demapping solution with negligible loss [79] often used in practice is obtained with the Max-Log approximation, written as:

$$\begin{aligned}
\Lambda(l^i(x)) &= \frac{1}{\sigma^2} \min_{x \in \mathcal{X}_1^i} \left\{ |r_1 - h_1 x_1|^2 + |r_2 - h_2 x_2|^2 \right\} \\
&\quad - \frac{1}{\sigma^2} \min_{x \in \mathcal{X}_0^i} \left\{ |r_1 - h_1 x_1|^2 + |r_2 - h_2 x_2|^2 \right\}.
\end{aligned} \tag{2.63}$$

Since the rotated modulations break the independence between the I and Q components, the two components must be considered together for the calculation of $\Lambda(l^i(x))$ for each transmitted bit b_i with $i = 0, 1, \dots, \log_2 M$, where M is the constellation size. Therefore, the calculation of the exact LLR (2.62) or obtained with the max-log approximation (2.63) requires exploring all constellation symbols. For high constellation size such as 64-QAM or 256-QAM, such demappers therefore have a high computational complexity which has a non-negligible impact on the design of the receiver [80].

In order to reduce this computational complexity, the use of a sub-optimal demapper based on the Max-Log approximation is generally preferred in practice. Moreover, in the literature, decorrelation methods such as Zero-Forcing (ZF) and Minimum Mean Square Error (MMSE) are proposed [81]; channel attenuation, along with the rotation matrix, are then processed by the receiver as the response of a MIMO channel with 2 inputs and 2 outputs. Therefore, with a classical equalization, the two components can be separated and the demapping of "equalized" symbols can therefore be done in a traditional way with a complexity in $\mathcal{O}(\log_2 M)$. However, the increase in noise level and the loss in performance when the channel response matrix is singular make these "one-dimensional" demapping methods highly sub-optimal and poorly suited to rotated modulations.

To address this performance loss, we will now summarize the contribution of several two-dimensional demappers proposed in the literature [82–86]. These methods allow better performance than one-dimensional demappers but with higher complexity.

[82] proposes to decompose the space of the QAM constellation into 4 sub-regions according to the sign of the real and imaginary part of the equalized symbol. The soft demapping is then carried out in one of these regions. Although this method reduces the complexity for an M-QAM and allows better performance than [81], the complexity of demapping always remains high in the order of $\mathcal{O}(M)$.

In addition, [83] propose to divide the constellation into $2\sqrt{M}$ sub-regions for I and Q components respectively, and to select two sub-regions for each bit according to the equalized symbol. This method is simpler than [82]. However, due to the low dependency among the bits of a QAM symbol, the total number of constellation points required for demapping the bits of a symbol is approximately equal to $\sqrt{M}((\log_2 M)/2)$, which makes the complexity of this technique finally comparable to that proposed in [82].

Moreover, [84] proposes to separate the space of the constellation into 16 independent sub-quadrants. For each of these sub-quadrants, [84] constructs a histogram of the constellation points involved in the calculation of the Max-Log LLR. Therefore, 16 histograms are used for demapping where the associated complexity and the total number of constellation points involved in the soft demapping procedure depend on the SNR.

Finally, [85, 86] proposes a method to select $2\sqrt{M}$ points of the constellation. The LLR values for the bits of a symbol are calculated with these points already selected. This method allows, with reduced complexity, to achieve the same performance as the Max-Log algorithm. In chapter 3, we will focus on a specific rotation angle that allows very low computational complexity without any performance loss and we will apply it to the underwater communication channel. Note that other geometric transformations than simple rotations can also be applied to constellations in order to obtain signal diversity [87].

2.4 Equalization

Equalization is the reversal operation for the distortion incurred by the frequency-selective multi-path channel [88]. It tends to reduce ISI and thus enhance the overall system performance. Somehow, by combining successive received symbols, it can be seen as a form of diversity.

2.4.1 Linear Equalization

Over multi-path channels, the received observation at time instant t contains copies of symbols belonging to other time instant. With linear equalization, this ISI is considerably reduced by multiplying these received symbols by certain *weights* and adding them can eliminate interference from neighbor symbols.

We now describe the Minimum Mean Square Error (MMSE) equalization. The goal of the MMSE approach is to minimize the sum of ISI and the Gaussian noise. Assuming filter matched at the front-end, and a sampler operating at frequency $1/T_s$ (i.e. in practice, usually $T_s = T$), the received samples $y(nT_s)$ can be modeled as [88]:

$$y(nT_s) = \sum_k r_c(nT_s - kT) s_k + n(nT_s), \quad (2.64)$$

where $r_c(t)$ denotes the concatenation of the filters in the transmission chain (see equation (2.9)) and $n(t)$ is the AWGN noise.

Suppose that the P received samples $y(k_0T + d_pT_s)$ are used to detect symbol s_{k_0} , $d_p = 0, \dots, P-1$; notice that the integer delays d_p are relative to k_0 and are parameters to be optimized as part of the equalizer design. These samples can be gathered in a vector \mathbf{y} , written as:

$$\mathbf{y} = \sum_k \mathbf{r}_c(k) s_k + \mathbf{n}, \quad (2.65)$$

where the j -th element of $\mathbf{r}_c(k)$ is given by:

$$r_c(k)_j = r_c(d_pT_s + (k_0 - k)T). \quad (2.66)$$

Observe that $r_c(k_0)_j = r_c(d_pT_s)$ is independent of k_0 , thus $\mathbf{r}_c(k_0)$ can be replaced by \mathbf{r}_c , where:

$$\mathbf{r}_c = [r_c(d_0T_s), r_c(d_1T_s), \dots, r_c(d_{P-1}T_s)]^T. \quad (2.67)$$

The output of the MMSE linear equalization is given by:

$$z_{k_0} = \mathbf{W}^H \mathbf{y}, \quad (2.68)$$

where \mathbf{W} is a P -dimensional column vector of the weight coefficients optimized according to a given criteria and $()^H$ is the Hermitian operator.

Thereafter, the receiver estimates the transmitted symbol \hat{s}_{k_0} among \mathbb{S} , the set of possible QAM constellation points, using the maximum likelihood criterion:

$$\begin{aligned} \hat{s}_{k_0} &= \arg \max_{S_j \in \mathbb{S}} \Pr(z_{k_0} | s_{k_0} = S_j) \\ &= \arg \max_{S_j \in \mathbb{S}} - |z_{k_0} - A_s(k_0) S_j|^2 \\ &= \arg \min_{S_j \in \mathbb{S}} |z_{k_0} - A_s(k_0) S_j|^2, \end{aligned} \quad (2.69)$$

where:

$$A_s(k_0) = \mathbf{W}^H \mathbf{r}_c(k_0) = \mathbf{W}^H \mathbf{r}_c. \quad (2.70)$$

Using Equation (2.69), the receiver simply searches the constellation point S_j such that $A_s(k_0) S_j$ is the closest to z_{k_0} in terms of Euclidean distance.

The weight vector \mathbf{W} is designed to minimize the cost function \mathbb{J} given by:

$$\begin{aligned} \mathbb{J} &= \mathbb{E} \{ |z_{k_0} - s_{k_0}|^2 \} \\ &= \mathbb{E} \{ (z_{k_0} - s_{k_0}) (z_{k_0} - s_{k_0})^* \} \\ &= \mathbb{E} (|s_{k_0}|^2) - \mathbf{W}^H \mathbb{E} (\mathbf{y} s_{k_0}^*) - \mathbb{E} (s_{k_0} \mathbf{y}^H) \mathbf{W} + \mathbf{W}^H \mathbb{E} (\mathbf{y} \mathbf{y}^T) \mathbf{W}. \end{aligned} \quad (2.71)$$

Using Equation (2.65), we obtain:

$$\begin{aligned} \mathbb{E} (\mathbf{y} s_{k_0}^*) &= E_s \mathbf{r}_c(k_0) = E_s \mathbf{r}_c, \\ \mathbb{E} (\mathbf{y} \mathbf{y}^H) &= E_s \mathbf{C}_y, \end{aligned} \quad (2.72)$$

where \mathbf{C}_y is the data correlation matrix.

Thus Equation (2.71) can be rewritten as:

$$\mathbb{J} = \mathbb{E} (|s_{k_0}|^2) - \mathbf{W}^H E_s \mathbf{r}_c - (E_s \mathbf{r}_c)^H \mathbf{W} + \mathbf{W}^H E_s \mathbf{C}_y \mathbf{W}. \quad (2.73)$$

To determine the MMSE solution, we take the derivation of \mathbb{J} with respect to the real and imaginary parts of each element in \mathbf{W} and set the derivatives to 0; we obtain:

$$-2E_s \mathbf{r}_c + 2E_s \mathbf{C}_y \mathbf{W} = 0. \quad (2.74)$$

Therefore, the MMSE weight vectors can be obtained by solving the following equation:

$$\mathbf{W} = \mathbf{C}_y^{-1} \mathbf{r}_c. \quad (2.75)$$

The MMSE solution requires the knowledge of channel characteristics at the receiver side; here, in practice, the receiver usually performs channel estimation to estimate \mathbf{r}_c before performing MMSE equalization.

2.4.2 Adaptive Equalization

In practice, the channel characteristics are unknown a priori, and in many cases, the channel response is time-varying. In this case, the equalizer is designed to be adjustable to the channel response and, for time-variant channels, to be adaptive to the time variations in the channel response. This section introduces the Least-Mean Squares (LMS) algorithm that can inherently adjust the equalizer coefficients in time-varying channel.

In the minimization of the MSE described in section 2.4.1, the optimum equalizer coefficients vector \mathbf{W}_{opt} are determined from the solution of Equation (2.75) by inverting the covariance matrix \mathbf{C}_y . Alternatively, to lower down the complexity burden, the receiver can use the gradient descent approach to find \mathbf{W}_{opt} ; it is arbitrarily initialized with a vector \mathbf{W}_0 ; after, the filter coefficients are updated such as:

$$\mathbf{W}_{k+1} = \mathbf{W}_k - \beta \left(\frac{1}{2} \frac{\partial \mathbb{J}}{\partial \mathbf{W}_k} \right), \quad (2.76)$$

where $\frac{1}{2} \frac{\partial \mathbb{J}}{\partial \mathbf{W}_k}$ is the gradient vector, given by:

$$\frac{1}{2} \frac{\partial \mathbb{J}}{\partial \mathbf{W}_k} = -\mathbf{y}_k^* (s_k - z_k). \quad (2.77)$$

The vector \mathbf{W}_k represents the set of coefficients at the k -th iteration and z_k is given by equation (4.42). The step size β is chosen to ensure convergence of the iterative procedure; not only it influences the convergence time, but also the asymptotic MSE, therefore, it needs to be carefully chosen.

Using Equation (2.77), (2.76) can be rewritten as:

$$\mathbf{W}_{k+1} = \mathbf{W}_k + \beta \mathbf{y}_k^* (s_k - z_k). \quad (2.78)$$

In practice, as the transmitted symbol s_k is generally unknown by the receiver, s_k in Equation (2.78) is replaced by the tentative decision on the equalizer output, which leads to the so-called decision-directed equalizer [89].

2.4.3 Turbo Equalization

Following the first step of Joachim Hagenauer, turbo equalization was proposed by Catherine Douillard in 1995 [90]; the data is protected by convolutional codes and the receiver consists of two trellis-based detectors, one for the equalizer and one for channel decoder. Turbo equalization approaches the performance of the maximum a posteriori (MAP) receiver via iterative soft information passing between a soft-in soft-out (SISO) equalizer and a SISO decoder. It has shown a significant improvement in bit error rate.

We now describe the system model of turbo equalization. At the transmitter side, a vector of bits $b_i \in \{0, 1\}$ of length K_b are first coded into coded bits of length K_c using a convolutional code, and then mapped to the alphabet \mathbb{S} of the signal constellation. For convenience, we consider the binary shift keying is used, i.e., $\mathbb{S} = \{+1, -1\}$, thus coded symbols $a_k \in \mathbb{S}, k = 1, \dots, K_c$. The interleaver then permutes a_k and transmits the symbols s_k .

The receiver input y_k is given by:

$$y_k = \left(\sum_{l=0}^{L-1} (r_c)_l s_{k-l} \right) + n_k. \quad (2.79)$$

- Turbo equalization using the MAP criterion [91]

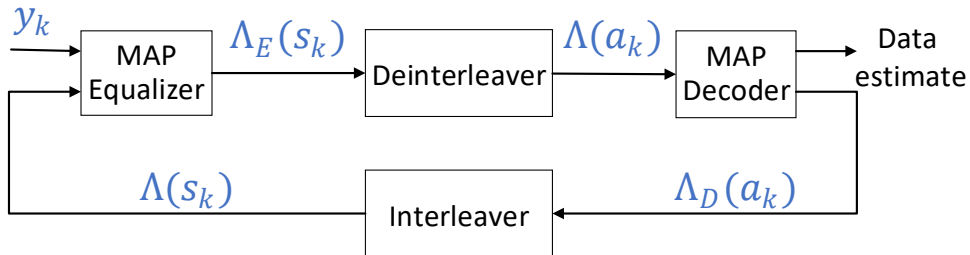


Figure 2.14: A receiver performing turbo equalization.

Figure 2.14 depicts the receiver structure for turbo equalization. The MAP equalizer computes the a posteriori probability

$\Pr(s_k = s|y_1, \dots, y_{K_C})$, given the K_C received symbols y_k , and outputs the extrinsic information to the decoder:

$$\Lambda_E(s_k) \triangleq \ln \frac{\Pr(s_k = +1|y_1, \dots, y_{K_C})}{\Pr(s_k = -1|y_1, \dots, y_{K_C})} - \ln \frac{\Pr(s_k = +1)}{\Pr(s_k = -1)}. \quad (2.80)$$

The LLR given by equation (2.80) is then used by the channel decoder as a priori information on the received symbol (s_k). The MAP decoder computes the a posteriori probabilities $\Pr(a_k = s|\Lambda(a_1), \dots, \Lambda(a_{K_C}))$, given K_C code bit LLRs $\Lambda(a_k)$, and outputs the difference:

$$\Lambda_D(a_k) \triangleq \ln \frac{\Pr(a_k = +1|\Lambda(a_1), \dots, \Lambda(a_{K_C}))}{\Pr(a_k = -1|\Lambda(a_1), \dots, \Lambda(a_{K_C}))} - \ln \frac{\Pr(a_k = +1)}{\Pr(a_k = -1)}, \quad (2.81)$$

where the equalizer output $\Lambda_E(s_k)$ is considered to be the a priori LLR $\Lambda(s_k)$ for the decoder. The decoder and the demapper may perform several iterations, at the end, the MAP decoder finally find the estimated data bit:

$$\hat{b}_i \triangleq \arg \max_{b \in \{0,1\}} \Pr(b_i = b|\Lambda(a_1), \dots, \Lambda(a_{K_C})). \quad (2.82)$$

This algorithm has good performance but with high complexity. In the next part, we examine another algorithm with lower complexity.

- Turbo Equalizer Using MMSE Equalization [89, 91]

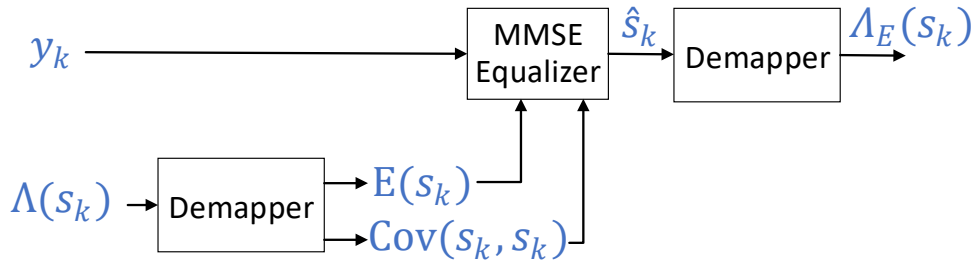


Figure 2.15: A SISO equalizer based on MMSE equalization.

In order to reduce the computational complexity of the turbo equalization (exponential in the number of $d = \frac{\tau_{rms}}{T}$ states), in practice $P = 4d$ where linear equalizer is usually used instead of the MAP equalizer. For the MMSE equalizer, the filter parameters are obtained by minimizing the cost function $J = \mathbb{E}(|s_k - \hat{s}_k|^2)$. Figure 2.15 depicts the general class of SISO equalizers for an MMSE equalizer.

The SISO equalizer output in Equation (2.80) is obtained using the estimate \hat{s}_k instead of y_k , which requires the

knowledge of the probability density function (PDF) distribution $f(\hat{s}_k | s_k = s)$, $s \in \mathbb{S}$; $\Lambda_E(s_k)$ can be rewritten as:

$$\begin{aligned}\Lambda_E(s_k) &\triangleq \ln \frac{\Pr(s_k = +1 | \hat{s}_k)}{\Pr(s_k = -1 | \hat{s}_k)} - \ln \frac{\Pr(s_k = +1)}{\Pr(s_k = -1)} \\ &= \ln \frac{\Pr(\hat{s}_k | s_k = +1)}{\Pr(\hat{s}_k | s_k = -1)}.\end{aligned}\tag{2.83}$$

To perform MMSE Equalization, the expectation $\bar{s}_k = \mathbb{E}(s_k)$ and covariance $\nu_k = \text{Cov}(s_k, s_k)$ of the symbols s_k are required:

$$\begin{aligned}\bar{s}_k &= \sum_{s \in \mathbb{S}} s \cdot \Pr(s_k = s) = \Pr(s_k = 1) - \Pr(s_k = -1) \\ &= \frac{e^{\Lambda(s_k)}}{1 + e^{\Lambda(s_k)}} - \frac{1}{1 + e^{\Lambda(s_k)}} = \tanh\left(\frac{\Lambda(s_k)}{2}\right), \\ \nu_k &= \sum_{s \in \mathbb{S}} |s - \bar{s}_k|^2 \cdot \Pr(s_k = s) = 1 - |\bar{s}_k|^2.\end{aligned}\tag{2.84}$$

The MMSE equalizer is a linear equalizer, consisting of a length P filter with time-varying coefficients $W_{k,p}$, $p = -P_1, 1 - P_1, \dots, P_2$, where $P = P_1 + P_2 + 1$. In practice $P \simeq 4d$, where $d = \frac{\text{Trms}}{T}$. Minimizing the MMSE [88] gives:

$$\hat{s}_k = \mathbb{E}(s_k) + \text{Cov}(s_k, \mathbf{y}_k) \text{Cov}(\mathbf{y}_k, \mathbf{y}_k)^{-1} (\mathbf{y}_k - \mathbb{E}(\mathbf{y}_k)),\tag{2.85}$$

where $\mathbf{y}_k \triangleq [y_{k-P_1}, y_{k-P_1+1}, \dots, y_{k+P_2}]^T$.

Equation (2.85) can be rewritten as:

$$\hat{s}_k = \bar{s}_k + \nu_k \mathbf{S}^H \left(\sigma_w^2 \mathbf{I}_P + \mathbf{C} \mathbf{V}_k \mathbf{C}^H \right)^{-1} (\mathbf{y}_k - \mathbf{C} \bar{s}_k),\tag{2.86}$$

where \mathbf{I}_P is the $P \times P$ identity matrix, \mathbf{C} is the $P \times (P + L - 1)$ channel convolutional matrix:

$$\mathbf{C} \triangleq \begin{bmatrix} (rc)_{L-1} & (rc)_{L-2} & \cdots & (rc)_0 & 0 & \cdots & 0 \\ 0 & (rc)_{L-1} & (rc)_{L-2} & \cdots & (rc)_0 & 0 & \cdots & 0 \\ & & & \ddots & & & & \\ 0 & & \cdots & 0 & (rc)_{L-1} & (rc)_{L-2} & \cdots & (rc)_0 \end{bmatrix}.\tag{2.87}$$

and

$$\begin{aligned}\bar{s}_k &\triangleq [\bar{s}_{k-L-P_2+1}, \bar{s}_{k-L-P_2+2}, \dots, \bar{s}_{k+P_1}]^T, \\ \mathbf{V}_k &\triangleq \text{Diag}(\nu_{k-L-P_2+1}, \nu_{k-L-P_2+2}, \dots, \nu_{k+P_1}), \\ \mathbf{S} &\triangleq \mathbf{C} \begin{bmatrix} \mathbf{0}_{1 \times (P_2+L-1)} & 1 & \mathbf{0}_{1 \times P_1} \end{bmatrix}^T.\end{aligned}\quad (2.88)$$

This yields to the final expression :

$$\hat{s}_k = \mathbf{W}_k^H (\mathbf{y}_k - \mathbf{C}\bar{s}_k + \bar{s}_k \mathbf{S}), \quad (2.89)$$

where the coefficient vector \mathbf{W}_k is given by:

$$\mathbf{W}_k \triangleq (\sigma_w^2 \mathbf{I}_P + \mathbf{C}\mathbf{V}_k\mathbf{C}^H + (1 - \nu_k) \mathbf{S}\mathbf{S}^H)^{-1} \mathbf{S}. \quad (2.90)$$

In the literature, the PDFs $f(\hat{s}_k | s_k = s)$, $s \in \mathbb{S}$ are generally considered Gaussian with parameters $\mu_{k,s} \triangleq \mathbb{E}(\hat{s}_k | s_k = s)$ and $\sigma_{k,s}^2 \triangleq \text{Cov}(\hat{s}_k, \hat{s}_k | s_k = s)$:

$$f(\hat{s}_k | s_k = s) \approx \phi\left(\left(\hat{s}_k - \mu_{k,s}\right) / \sigma_{k,s}\right) / \sigma_{k,s}, \quad (2.91)$$

where $\phi(s) = e^{-\frac{s^2}{2}}/2$. This assumption tremendously simplifies the computation of the SISO equalizer output LLR $\Lambda_E(s_k)$. From the expression of \hat{s}_k , the statistics $\mu_{k,s}$ and $\sigma_{k,s}^2$ are computed as:

$$\begin{aligned}\mu_{k,s} &= \mathbf{W}_k^H (\mathbb{E}(\mathbf{y}_k | s_k = s) - \mathbf{C}\bar{s}_k + \bar{s}_k \mathbf{S}) = s \cdot \mathbf{W}_k^H \mathbf{S}. \\ \sigma_{k,s}^2 &= \mathbf{W}_k^H \text{Cov}(\mathbf{y}_k, \mathbf{y}_k | s_k = s) \mathbf{W}_k \\ &= \mathbf{W}_k^H (\sigma_w^2 \mathbf{I}_P + \mathbf{C}\mathbf{V}_k\mathbf{C}^H - \nu_k \mathbf{S}\mathbf{S}^H) \mathbf{W}_k \\ &= \mathbf{W}_k^H \mathbf{S} (1 - \mathbf{S}^H \mathbf{W}_k).\end{aligned}\quad (2.92)$$

The output LLR follows as:

$$\begin{aligned}\Lambda_E(s_k) &= \ln \frac{\phi\left(\left(\hat{s}_k - \mu_{k,+1}\right) / \sigma_{k,+1}\right) / \sigma_{k,+1}}{\phi\left(\left(\hat{s}_k - \mu_{k,-1}\right) / \sigma_{k,-1}\right) / \sigma_{k,-1}} = 2 \frac{\hat{s}_k \mu_{k,+1}}{\sigma_{k,+1}^2} \\ &= 2 \mathbf{W}_k^H (\mathbf{y}_k - \mathbf{C}\bar{s}_k + \bar{s}_k \mathbf{S}) / (1 - \mathbf{S}^H \mathbf{W}_k).\end{aligned}\quad (2.93)$$

Note that similarly to linear equalization of section 2.4.1, the channel must be estimated to find \mathbf{C} .

2.5 Conclusion

In this chapter, we first recalled some elementary basics of digital communications, and then presented the main characteristics of fading channels. In general, the signals from the multiple paths can add up in a constructive or destructive way; fading channels are therefore unreliable, leading to a need for diversity techniques. In addition, when the link is frequency selective, the signal transmitted on this type of channel follows different paths to arrive at the receiver on successive symbols, so that equalization at the receiver side is thus required. Finally, this chapter introduces several equalizer proposed in the literature, the LMS algorithm, the MMSE equalizer and turbo equalization.

In the following chapter we will elaborate some more on a special angle to obtain signal diversity. This signal diversity does not spoil any channel resources and this is of particular interest for the acoustic underwater channel for which the bandwidth is particularly scarce.

Chapter 3

Signal Space Diversity for Underwater Communications

Contents

3.1	Uniformly Projected Rotated and Cyclic Q-delayed QAM	69
3.1.1	System Model	70
3.1.2	Properties of the Rotated Constellation with Rotation Angle $\theta = \arctan(1/\sqrt{M})$	72
3.1.3	Soft Demapper for the UP-RCQD M-QAM Constellation	73
3.1.3.1	Calculation of LLRs in the Integer Domain	74
3.1.3.2	Determination of the Global Optimum T_{opt}	75
3.1.3.3	Search for Complementary Points T_{cplm}^i	76
3.1.3.4	Summary of the Studied Soft Demapping Algorithm	76
3.1.3.5	Complexity Analysis of the Studied Soft Demapping Algorithm	77
3.1.4	Numerical Results	78
3.1.4.1	BER Underwater Performance	78
3.1.4.2	Demapper Comparison	81
3.2	Low-Complexity Blind PAPR Reduction for OFDM Systems with Rotated Constellations	83
3.2.1	Overview of the Proposed Blind PAPR Reduction Technique with SSD	83
3.2.1.1	At the Transmitter Side	83
3.2.1.2	Interleaver Estimation at the Receiver Side	85
3.2.2	Detailed Proposal and Complexity Considerations	86

3.2.2.1	Low Complexity MMSE-based Decoder	87
3.2.2.2	Low Complexity Index Estimation for the Uniformly Projected RCQD Constellations	88
3.2.2.3	Complexity Analysis	90
3.2.3	Simulation Results	91
3.3	Conclusion	95

The underwater acoustic channel is time-varying with a particularly limited bandwidth. This makes reliable communications difficult to achieve and limits the information rate. The rotated constellation is an effective technique that saves both bandwidth and energy, as it allows to take advantage of the channel diversity and thus to enhance performance of rotated constellations over some fading channels such as underwater acoustic channels. However, the real cost of this technique is the high complexity of the demodulation that prevented its wider use. To face this problem, this chapter proposes to focus on the M-QAM rotated modulation using a series of rotation angle $\theta = \arctan(1/\sqrt{M})$ which introduces several structural properties that can be used to tremendously ease up the soft demapping process.

This chapter is organized as follows in two main sections. In the first section, the first subsection introduces the BICM communication system model with the rotated constellation; then, the structural properties of the series of angles $\theta = \arctan(1/\sqrt{M})$ are presented in the second subsection and the following subsection details the soft demapping solution; the performance of the rotation angles $\theta = \arctan(1/\sqrt{M})$ on underwater channels and those of the demapper solution are given in the last subsection.

The second section describes an original PAPR reduction technique for OFDM systems using rotated constellations, the first subsection briefly outlines the proposed technique and describes the system model, the second subsection details the proposed low-complexity decoder and provides a complexity analysis of the proposal, some simulation results are shown in the following subsection. Finally, we draw conclusions at the end of this chapter.

3.1 Uniformly Projected Rotated and Cyclic Q-delayed QAM

As we showed in chapter 2, rotated constellations bring inherent diversity to a system without any spectral spoilage. The DVB-T2 standard was the first industrial standard to use rotated M-QAM constellations which theoretically performs better than conventional M-QAM constellations over fading channels. Nevertheless, this solution increases dramatically the complexity at the receiver side. Indeed, the two-dimensional demappers proposed in the literature have a high computational complexity which has a non-negligible impact on the design of the receiver.

In this section, we will be interested in a particular series of rotation angles with interesting structural properties. Building on these, we will detail a low complexity demapper dedicated to these angles and will test it on two underwater

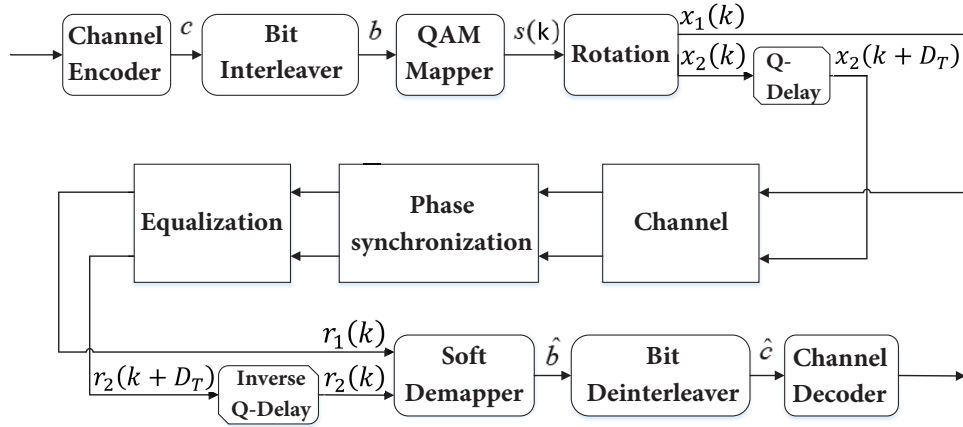


Figure 3.1: BICM system model with RCQD constellation

channels.

3.1.1 System Model

Figure 3.1 presents the system model and we consider the M-QAM constellations. A message frame passes through a channel encoder and generates a codeword c . The codeword is then interleaved to ensure that consecutive bits are transmitted through independent fading subchannels. Then every group of $\log_2 M$ bits is transformed, with Gray mapping, into a complex symbol of the M-QAM constellation:

$$s(k) = s_1(k) + js_2(k), \quad (3.1)$$

where $s_1(k)$ (resp. $s_2(k)$) is the in-phase (resp. quadrature) component at time k . The components s_m can be expressed in another way such as:

$$s_m(k) = -\sqrt{M} + 1 + 2p_m, \quad (3.2)$$

where index m is in $\{1, 2\}$ and p_m takes an integer value in $\{0, 1, \dots, \sqrt{M} - 1\}$. Note that similarly to the Gray mapping defined in DVB-T2 [79], $s_1(k)$ (or p_1) is mapped from the even-indexed bits whereas $s_2(k)$ (or p_2) is mapped from the odd-indexed bits.

The first step to generate rotated symbols (Rotated and Cyclic Q-Delayed (RCQD)) is to correlate the components $s_1(k)$ and $s_2(k)$ through the multiplication with a properly designed rotation factor $\exp(j\theta)$, so that the in-phase component $x_1(k)$ and quadrature component $x_2(k)$ of the rotated symbol $x(k)$ contain the complete information of the original

unrotated symbol $s(k)$:

$$x(k) = x_1(k) + jx_2(k) = s(k) \exp(j\theta), \quad (3.3)$$

where

$$\begin{cases} x_1(k) = s_1(k) \cos \theta - s_2(k) \sin \theta \\ x_2(k) = s_1(k) \sin \theta + s_2(k) \cos \theta \end{cases}. \quad (3.4)$$

The second step of the RCQD modulation consists in cyclically delaying the Q component $x_2(k)$, so that the components $x_1(k)$ and $x_2(k)$ of the rotated symbol $x(k)$ pass through independently attenuated subchannels as follows:

$$z(k) = \beta (x_1(k) + jx_2(k + D_T)), \quad (3.5)$$

$$z(k - D_T) = \beta (x_1(k - D_T) + jx_2(k)), \quad (3.6)$$

where β is the normalization factor of the QAM constellation (e.g., $\beta = 1/\sqrt{170}$ for a 256-QAM signal) and D_T is the integer delay.

At the output of the channel as already mentioned in chapter 2, the receiver must first achieve synchronization and equalization of the signal. We will elaborate some more on these topics in chapter 4, but to focus on the study of rotated constellations, we assume in a first step that there is no ISI and synchronization is absolutely perfect so that the received observation $r_1(k)$ (resp. $r_2(k)$) of the transmitted component $x_1(k)$ (resp. $x_2(k)$) is approximated by:

$$r_m(k) = \beta h_m(k) x_m(k) + v_m(k), \quad (3.7)$$

where m is in $\{1, 2\}$, $h_1(k)$ and $h_2(k)$ are the channel attenuation terms, and $v(k) = v_1(k) + jv_2(k)$ is a complex Gaussian noise of variance σ^2 . In order to simplify the notation, in the sequel, the index (k) is dropped. Subsequently, the receiver calculates the LLRs of the bits using equation (2.62). With a negligible loss in performance, the calculation of LLRs can also be done with the Max-Log approximation (2.63).

Finally, from the calculated and deinterleaved LLRs, channel decoding is performed in order to best estimate the information bits.

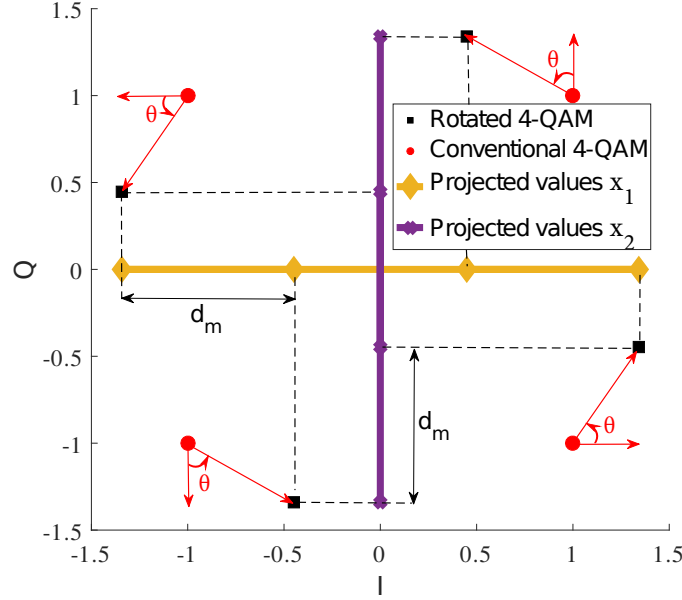


Figure 3.2: Uniformly projected RCQD 4-QAM signal

3.1.2 Properties of the Rotated Constellation with Rotation Angle $\theta = \arctan(1/\sqrt{M})$

We propose to use the rotation angle $\theta = \arctan(1/\sqrt{M})$ [30, 92]. x_1 and x_2 in equation (3.4) can then be rewritten as:

$$\begin{cases} x_1 = (\sqrt{M}s_1 - s_2) \sin \theta \\ x_2 = (\sqrt{M}s_2 + s_1) \sin \theta \end{cases}, \quad (3.8)$$

where s_1 (resp. s_2) is the in-phase (resp. quadrature) component (see (3.2)) of the non-rotated M-QAM symbol s .

Property 1 *The components $x_1(k)$ (resp. $x_2(k)$) of the rotated symbols are uniformly projected on I (resp. Q) axes with a constant minimum distance $d_m = 2 \sin \theta$ between two consecutive points.*

This property can be observed in Figure 3.2 for the 4-QAM constellation. Therefore, rotated constellations with the rotation angle $\theta = \arctan(1/\sqrt{M})$ are referred in the sequel to as the Uniformly Projected RCQD (UP-RCQD) constellations.

Property 2 *There is a one-to-one correspondence between the rotated component x_1 (resp. x_2) and an integer pair (p_1, p_2) .*

Define an integer pair $(T_{x,1}, T_{x,2})$ as:

$$\begin{cases} T_{x,1} = \frac{M-1}{2} + \frac{x_1}{2 \sin \theta} \\ T_{x,2} = \frac{M-1}{2} + \frac{x_2}{2 \sin \theta} \end{cases}, \quad (3.9)$$

where $T_{x,m}$ take integer values in $\{0, 1, \dots, M-1\}$, $m \in \{1, 2\}$ (see (3.8) and (3.9)). One value taken by $T_{x,1}$ can uniquely determine one integer pair (p_1, p_2) (recall definition in (3.2)) as:

$$\begin{cases} p_1 = \lfloor \frac{T_{x,1}}{\sqrt{M}} \rfloor \\ p_2 = \sqrt{M} - 1 - (T_{x,1} - \sqrt{M}p_1) \end{cases}, \quad (3.10)$$

where $\lfloor a \rfloor$ designates the integer part of a . Reversely, one value taken by $T_{x,2}$ can uniquely determine one integer pair (p_1, p_2) as:

$$\begin{cases} p_2 = \lfloor \frac{T_{x,2}}{\sqrt{M}} \rfloor \\ p_1 = -\sqrt{M}p_2 + T_{x,2} \end{cases}. \quad (3.11)$$

Property 3 Any \sqrt{M} consecutive integers $T_{x,1}$ (resp. $T_{x,2}$) contain every possibly taken integer values p_2 (resp. p_1).

This property is illustrated in Figure 3.3 for the UP-RCQD 16-QAM constellation.

These three properties will be used in the demodulator described in section 3.1.3 below, which exploits the regular structure of the rotated constellation and the fact of being able to work with the integer couple $(T_{x,1}, T_{x,2})$.

3.1.3 Soft Demapper for the UP-RCQD M-QAM Constellation

On the receiver side, the observation components r_m can be transformed as following:

$$\begin{aligned} R_m &= \frac{r_m}{2\beta h_m \sin \theta} + \frac{M-1}{2} \\ &= \frac{x_m}{2 \sin \theta} + \frac{v_m}{2\beta h_m \sin \theta} + \frac{M-1}{2} \\ &= T_{x,m} + \frac{v_m}{2\beta h_m \sin \theta}, \end{aligned} \quad (3.12)$$

where $m \in \{1, 2\}$ and $T_{x,m}$ is given by (3.9).

Therefore, the term $|r_m - h_m \beta x_m|^2$ can be expressed as:

$$|r_m - h_m \beta x_m|^2 = (2\beta \sin \theta)^2 |h_m (R_m - T_{x,m})|^2. \quad (3.13)$$

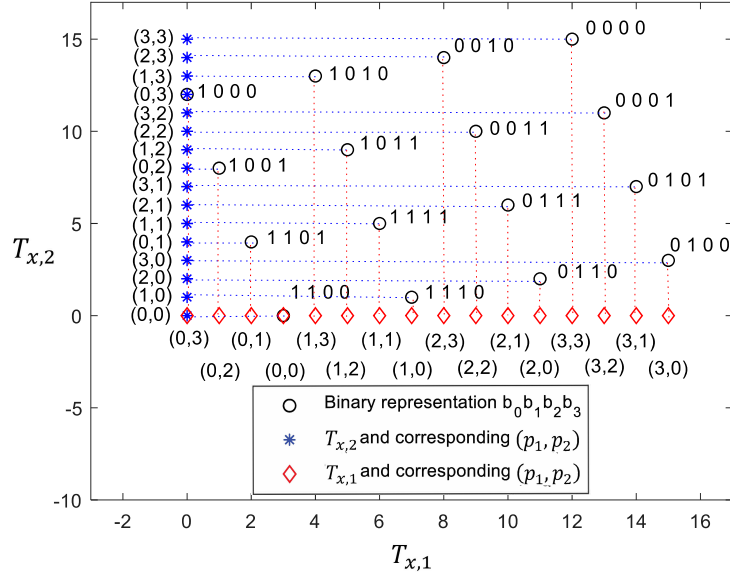


Figure 3.3: (T_I, T_Q) and the corresponding binary representation $(b_0 b_1 b_2 b_3)$ of the 16-QAM signal.

3.1.3.1 Calculation of LLRs in the Integer Domain

With (3.13), the Max-Log LLR computation (2.63) becomes:

$$\Lambda(l^i(x)) = \frac{(2\beta \sin \theta)^2}{\sigma^2} \min_{T_x \in \mathbf{T}_1^i} \left\{ |h_1(R_1 - T_{x,1})|^2 + |h_2(R_2 - T_{x,2})|^2 \right\} - \frac{(2\beta \sin \theta)^2}{\sigma^2} \min_{T_x \in \mathbf{T}_0^i} \left\{ |h_1(R_1 - T_{x,1})|^2 + |h_2(R_2 - T_{x,2})|^2 \right\}, \quad (3.14)$$

where \mathbf{T}_0^i (resp. \mathbf{T}_1^i) is the set of the constellation points whose i -th bit is 0 (resp. 1).

For the fading channel, the Max-Log demapper in (3.14) indicates that computing $\log_2 M$ LLR values requires $2\log_2 M$ minimal distance terms (i.e. $\min_{T_x \in \mathbf{T}_b^i} \left\{ |h_1(R_1 - T_{x,1})|^2 + |h_2(R_2 - T_{x,2})|^2 \right\}$). Among these Euclidean distances, half (i.e. $\log_2 M$ distance terms) can be found once the point which maximizes the likelihood (ML), denoted $T_{opt} = (T_{1,opt}, T_{2,opt})$ (i.e., the nearest constellation point to the received observation), is located; while the other $\log_2 M$ terms in (3.14) requires to find the closest constellation point (to the received point) $T_{cplm}^i = (T_{1,cplm}^i, T_{2,cplm}^i)$ whose i -th information bit is complementary to the i -th bit of the global optimum T_{opt} .

Therefore, the soft demapping algorithm comprises two steps: first locating the global optimum point and then

searching for complementary points. Finally, the receiver calculates the LLRs of the bits as follows:

$$\Lambda(l^i(x)) = \begin{cases} \frac{(2\beta \sin \theta)^2}{\sigma^2} \left(d(T_{cplm}^i, R) - d(T_{opt}, R) \right), & l^i(T_{opt}) = 0 \\ \frac{(2\beta \sin \theta)^2}{\sigma^2} \left(d(T_{opt}, R) - d(T_{cplm}^i, R) \right), & l^i(T_{opt}) = 1 \end{cases}, \quad (3.15)$$

where $d(T_o, R)$ denotes the two-dimensional Euclidean distance between the point T_o (T_{opt} or T_{cplm}^i) and the equalized observation R :

$$d(T_o, R) = |h_1(R_1 - T_{1,o})|^2 + |h_2(R_2 - T_{2,o})|^2. \quad (3.16)$$

3.1.3.2 Determination of the Global Optimum T_{opt}

Proposition 1 *For the UP-RCQD M-QAM constellation, the local optimum $T_{m,Loc opt}$ where $m \in \{1, 2\}$ denotes the I or Q component (i.e., the nearest point to the equalized observation R_m) is obtained by minimizing (3.13) as follows:*

$$T_{m,Loc opt} = \begin{cases} 0, & \text{if } R_m \leq 0, \\ \text{round}(R_m), & \text{if } 0 \leq R_m < (M-1), \\ M-1, & \text{if } R_m \geq (M-1). \end{cases} \quad (3.17)$$

This proposition indicates that each received observation R_m (where m is in $\{1, 2\}$) identifies a unique 1D local nearest point (see example on Figure 3.4); in the case where $T_{1,Loc opt}$ and $T_{2,Loc opt}$ given by (3.17) lead to the same (p_1, p_2) pair (see (3.10)-(3.11)), then this pair is necessarily the global optimum because the two Euclidean distances (3.13) are both minimized (see (3.14)). However, in poor channel conditions, the two local optima $T_{1,Loc opt}$ and $T_{2,Loc opt}$ can lead to two distinct pairs (p_1, p_2) and the global optimum which minimizes (3.14) may not be one of these two pairs. In this case, one may increase the number of candidate points by searching points centered around R_1 and R_2 . The integer radius of the searching region is r_a . This region can be rewritten as:

$$\tilde{\mathbf{T}}_m = \begin{cases} \{0, \dots, 2r_a - 1\}, & \text{if } R_m < r_a, \\ \{M - 2r_a, \dots, M - 1\}, & \text{if } R_m \geq M - r_a, \\ \{\lfloor R_m \rfloor - r_a + 1, \dots, \lfloor R_m \rfloor + r_a\}, & \text{otherwise.} \end{cases} \quad (3.18)$$

Each point T_x in $\tilde{\mathbf{T}}_m$ determines a pair (p_1, p_2) and this pair designates a unique symbol of the conventional (not rotated) constellation (s_1, s_2) . $\tilde{\mathbf{T}}_m$ contains exactly $2r_a$ points. Note that the probability of finding the true global

optimum T_{opt} among the $4d$ points of the sets $\tilde{\mathbf{T}}_1$ and $\tilde{\mathbf{T}}_2$ increases with the radius r_a .

Moreover, differently from the sphere decoding [93], the studied algorithm uses the equalized observation R_m rather than r_m . In addition, note that the radius r_a implies an exact number of points (see (3.18)) used in the calculation of LLRs, while in [93], one cannot predetermine the number of points involved in the demapping.

3.1.3.3 Search for Complementary Points T_{cplm}^i

According to property 3, the region centered on the local optimum $T_{1,Loc\ opt}$ (resp. $T_{2,Loc\ opt}$) with a radius $r_a = \sqrt{M}/2$ contains all possible values of p_2 (resp. p_1). Therefore, $\tilde{\mathbf{T}}_1$ and $\tilde{\mathbf{T}}_2$ guarantee to find the complementary point T_{cplm}^i for any index bit i corresponding to the complementary of $T_{1,Loc\ opt}$ or $T_{2,Loc\ opt}$ considered bit.

Example: For the UP-RCQD 16-QAM constellation mapped with Gray mapping, let $(R_1 = 4.4, R_2 = 9.3)$ be the received and equalized observations pair.

Using (3.17), we obtain these two local optima: the closest in-phase component point $T_{1,Loc\ opt} = 4$ (cf. $(p_1, p_2) = (1, 3)$) and the closest quadrature component point $T_{2,Loc\ opt} = 9$ (cf. $(p_1, p_2) = (1, 2)$) (see figure 3.4). The two regions centered on the received observation with a radius $r_a = \sqrt{16}/2 = 2$ are $\tilde{\mathbf{T}}_1 = \{3, 4, 5, 6\}$ and $\tilde{\mathbf{T}}_2 = \{8, 9, 10, 11\}$. The region $\tilde{\mathbf{T}}_1$ comprises the symbols $(p_1, p_2) = (0, 0), (1, 3), (1, 2), (1, 1)$ and the region $\tilde{\mathbf{T}}_2$ comprises the symbols $(p_1, p_2) = (0, 2), (1, 2), (2, 2), (3, 2)$ (see Figure 3.4). We can notice that the region centered on R_1 (resp. R_2) contains all the possible values of p_2 (resp. p_1), thus guarantee to find all the points complementary to $T_{1,Loc\ opt}$ (resp. $T_{2,Loc\ opt}$).

3.1.3.4 Summary of the Studied Soft Demapping Algorithm

Bringing together the results of the previous sections, we now briefly overview the 4 steps of the previously described soft demapping algorithm:

1. Using (3.12), r_1 and r_2 are transformed into R_1 and R_2 .
2. Finding \sqrt{M} points centered around R_1 and \sqrt{M} points centered around R_2 using (3.18) with $r_a = \sqrt{M}/2$, then find the global optimum point within $4r_a$ points by calculating the minimum distance from R . Note that the global optimum T_{opt} is directly obtained if the two local optima lead to the same (p_1, p_2) pair.
3. For each bit, all the points with i -th bit complementary to the i -th bit of T_{opt} are selected among $4r_a$ points, then calculate the minimum distance using (3.16).
4. Once the minimum Euclidean distances have been obtained for T_{opt} in the second step and for the complementary points in the third step, the calculation of the LLR is then performed for all the bits using (3.15).

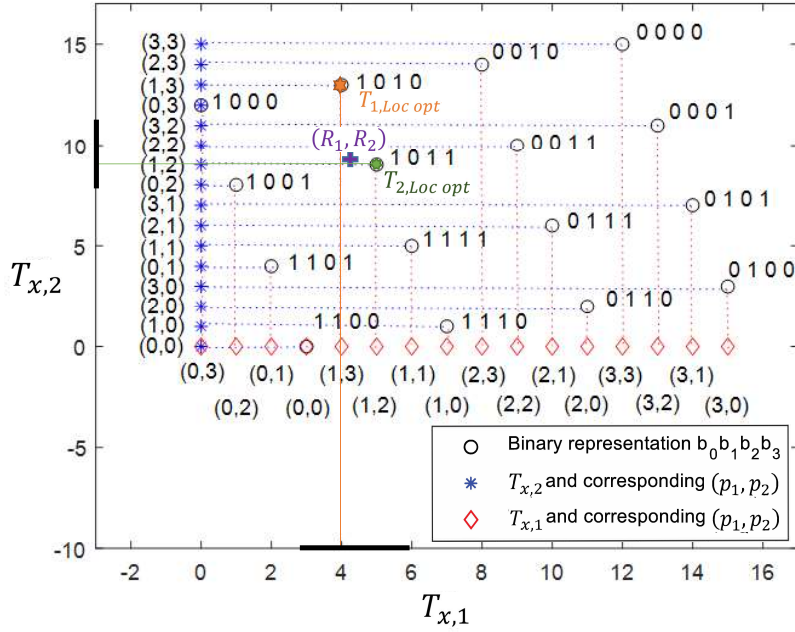


Figure 3.4: Example of determining the two local optima and complementary points for the UP-RCQD 16-QAM.

3.1.3.5 Complexity Analysis of the Studied Soft Demapping Algorithm

The complexity of the studied soft demapping algorithm is evaluated in number of Candidate Points (CP), Real Multiplications (RM), Real Comparisons (RC), Real Inversions (RI) and Real Summations (additions or subtractions) (Rs).

For a rotation angle θ , the x_1 and x_2 components of a symbol of the rotated M-QAM constellation are obtained with (3.4), this operation requires 4 RMs and 2 RSs. However, when the rotation angle is $\theta = \arctan(1/\sqrt{M})$, the x_1 and x_2 components are obtained with (3.8), the multiplication by a factor \sqrt{M} can be implemented by $(\log_2 M)/2$ left-shifts, the rotation operation in this case therefore only requires 2 RMs and 2 RSs.

The demodulation complexity on the receiver side is detailed below:

- In Step 1, $(\frac{1}{2\beta h_m \sin \theta})$ and $((M-1)/2)$ are constant and therefore do not need to be recalculated for each component received; the transformation (3.12) from r_1 to R_1 and r_2 to R_2 requires only 2 RSs, 2 RMs and 2 RIs.
- In Step 2, the selection of two regions requires 4 RCs (see (3.18)). Each term $|h_1(r_1 - T_{x,1})|^2 + |h_2(r_2 - T_{x,2})|^2$ requires 4 RMs and 3 RSs. So globally, $2\sqrt{M}$ distance terms need $8\sqrt{M}$ RMs and $6\sqrt{M}$ RSs and to compare $2\sqrt{M}$ distance terms in order to find the minimum distance needs $(2\sqrt{M}-1)$ RCs. So step 2 totally requires $8\sqrt{M}$ RMs, $6\sqrt{M}$ RSs and $(2\sqrt{M}+3)$ RCs.
- In Step 3, $\log_2 M$ minimum distances are required for the $\log_2 M$ complementary bits. Since each bit requires $2(\sqrt{M}-1)$ RCs, this step requires a total of $2(\sqrt{M}-1)\log_2 M$ RCs.

Table 3.1: The measurement parameters.

Parameters	NOF1	NCS1	BCH1	KAU1	KAU2
Environment	Fjord	Shelf	Harbour	Shelf	Shelf
Time of the year	June	June	May	July	July
Water depth	10 m	80 m	20 m	100 m	100 m
-3dB freq. band	10–18 kHz	10–18 kHz	32.5–37.5 kHz	4–8 kHz	4–8 kHz
Duration	32.9 s	32.6 s	59.4 s	32.9 s	32.9 s
Type	SISO	SISO	SIMO	SIMO	SIMO
Hydrophones	1	1	4	16	16

- In Step 4, multiply the term $\frac{(2\beta \sin \theta)^2}{\sigma^2}$ requires 1 RMs. There is therefore a total of $\log_2 M$ RMs and $\log_2 M$ RSs for $\log_2 M$ bits.

Summing the complexity of the previous four steps, we find that the total complexity of calculating LLR values (3.15) of one symbol equals to $2\sqrt{M}$ CPs, $(8\sqrt{M} + \log_2 M + 2)$ RMs, $(5 + (2\sqrt{M} - 2)(1 + \log_2 M))$ RCs, 2 RIs and $(6\sqrt{M} + \log_2 M + 2)$ RSs.

3.1.4 Numerical Results

This section contains two parts. The first part presents the performance of the UP-RCQD M-QAM constellations in terms of BER over some underwater acoustic channels. The second one compares the demapper complexity and BER of the studied soft demapping algorithm to other methods currently in use.

3.1.4.1 BER Underwater Performance

Several physical layer algorithms and modulation techniques have been proposed in recent years for underwater communications. However, it is difficult to compare the performance of these proposals objectively because the simulation conditions are different. WATERMARK is a Matlab platform which includes a library containing impulse responses from 5 actual underwater acoustic channels measured in Norway, France and Hawaii [94]. The measurement parameters are summarized in Table 3.1. Figure 3.5 and 3.6 shows the impulse responses obtained at times $t = 0, 1, 2s$ of two submarine channels (a submarine channel measured off the western side of Kauai, HI, USA, noted KAU2 and a submarine channel from Norway-Oslofjorden noted NOF1 [95]). These two figures point out that the considered channels are frequency and time selective. The coherence time (resp. the symbol duration) is equal to 128 ms (resp. 0.25 ms) for both channel.

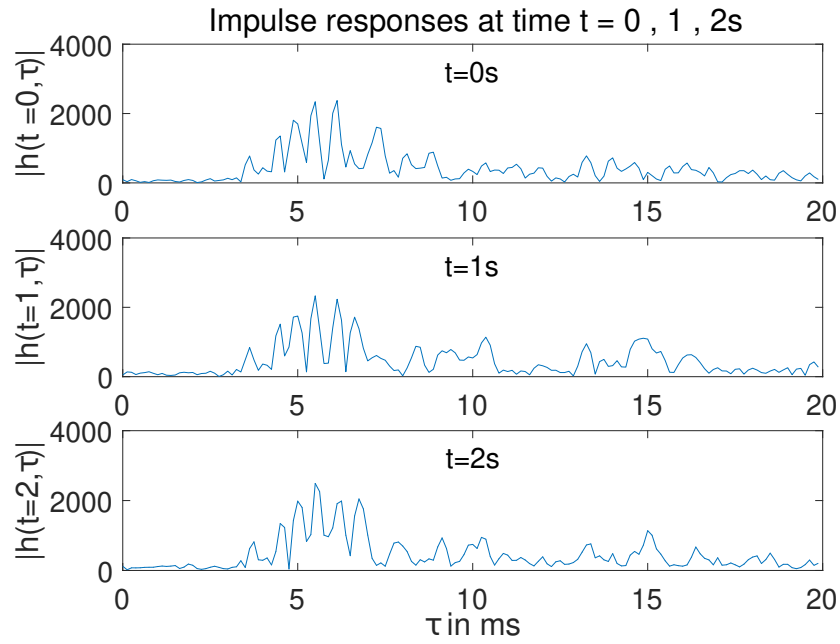


Figure 3.5: Impulse responses at times $t = 0, 1$ and 2 s of KAU2.

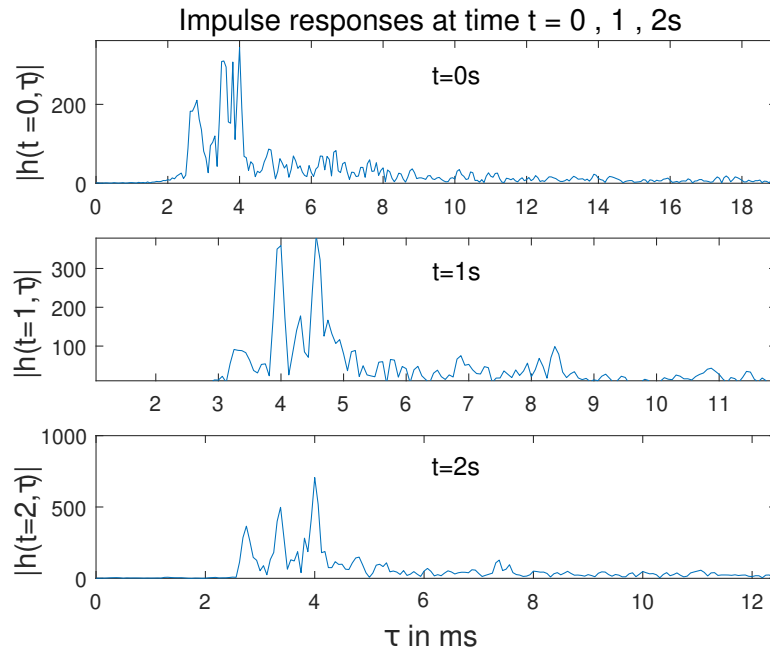


Figure 3.6: Impulse responses at times $t = 0, 1$ and 2 s of NOF1.

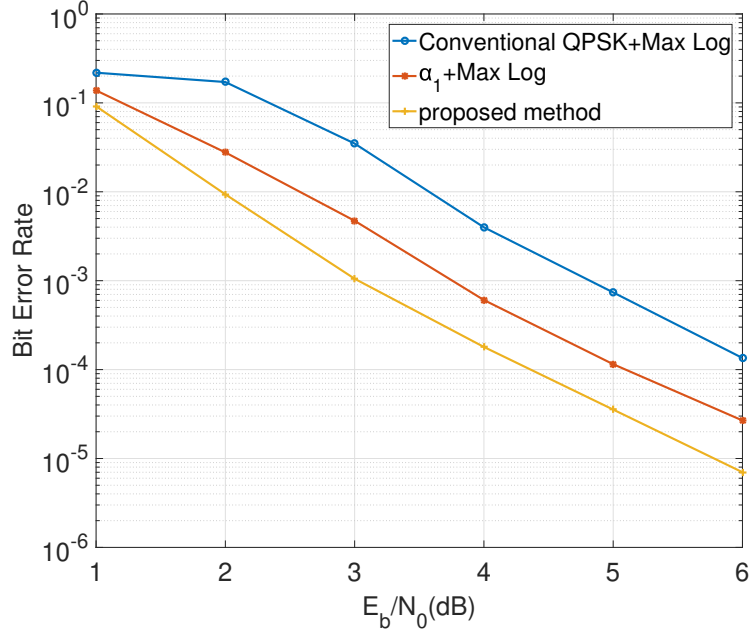


Figure 3.7: BER comparison between the studied soft demapping method and α_1 and conventional QPSK signals on KAU2 channel.

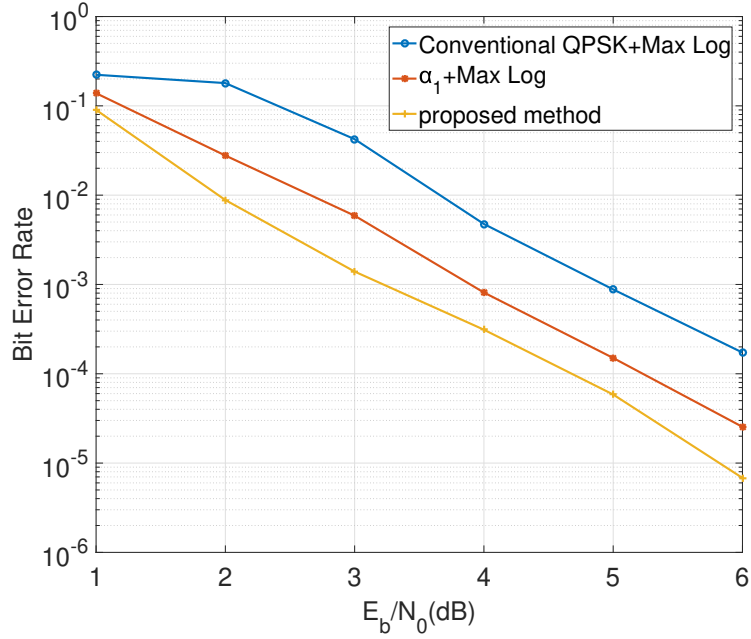


Figure 3.8: BER comparison between the studied soft demapping method and α_1 and conventional QPSK signals on NOF1 channel.

Figure 3.7 and 3.8 show the performances in terms of Bit Error Rate (BER) of the rotation angle $\theta = \arctan(1/\sqrt{M})$,

Table 3.2: Comparison of the complexity of different demapping method

	CP	RC	RI
Studied soft demapping method	$2\sqrt{M}$	$5 + (2\sqrt{M} - 2)(1 + \log_2 M)$	2
Max-Log	M	$(M - 2)\log_2 M$	0
Sub-Region	$\left(\frac{\sqrt{M}}{2} + 1\right)^2$	$\left(\left(\frac{\sqrt{M}}{2} + 1\right)^2 - 2\right)\log_2 M$	0
MMSE	\sqrt{M}	$(\sqrt{M} - 2)\log_2 M$	6
PD-DEM	$\sqrt{M}\left(\frac{\log_2 M}{2} + 1\right)$	$3\sqrt{M} + \left(\frac{7}{4}\sqrt{M} - \frac{7}{2}\right)\log_2 M - 3$	0

	RS	RM
Studied soft demapping method	$6\sqrt{M} + \log_2 M + 2$	$8\sqrt{M} + \log_2 M + 2$
Max-Log	$3M + \log_2 M$	$4M + \log_2 M$
Sub-Region	$3\left(\frac{\sqrt{M}}{2} + 1\right)^2 + \log_2 M$	$4\left(\frac{\sqrt{M}}{2} + 1\right)^2 + \log_2 M$
MMSE	$2\sqrt{M} + \log_2 M + 8$	$2\sqrt{M} + \log_2 M + 24$
PD-DEM	$\sqrt{M}\left(\frac{3}{2}\log_2 M + 5\right) + \log_2 M - 1$	$\sqrt{M}(2\log_2 M + 8) + \log_2 M - 2$

the reference angle $\alpha_1 = \arctan((1 - \sqrt{5})/2)$ which is often considered as asymptotically optimal [63], and the conventional non-rotated QPSK constellation on KAU2 and NOF1 channels. In this simulation, we use a 5/6 rate Turbo code and each simulated packet contains 512 bits (64 bytes). As the considered underwater channels are multi-path, the received signals are turbo-equalized as detailed in chapter 4, and the BER curves are estimated through Monte Carlo simulations.

Figure 3.7 and 3.8 show that the performances of the studied soft demapping method exceed those of the conventional QPSK signals by approximately 2 dB and exceed those of the rotated signals with angle α_1 by 0.75 dB for both channels. Once again, these results underline that the UP-RCQD signal allows good performance and that the inherent diversity provided by the rotation results in better performance than non-rotated constellations.

3.1.4.2 Demapper Comparison

Table 3.2 compares for different algorithms the complexity required, in terms of number of CPs, RMs, RSs, RCs and RIs, for the demodulation of a symbol of the M-QAM constellation. In addition, the complexity cost function of different demapping methods for demapping one received rotated symbol are compared in Figure 3.9, including the studied soft demapping method, the full-complexity Max-Log method, the Sub-Region method, the MMSE method and PD-DEM method. We assume that the cost of RC and RS are one, RM or RI is two or four respectively. It can be observed that the MMSE demapper has the lowest complexity among the considered demappers; nevertheless, it gives the worst performances in terms of BER because algorithms based on decorrelation are not optimal for rotated constellations

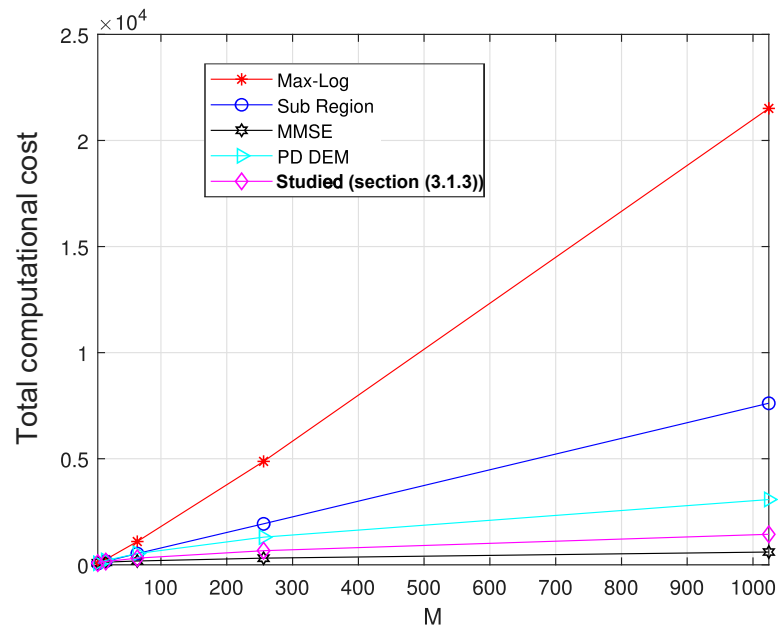


Figure 3.9: Complexity comparison of several demappers

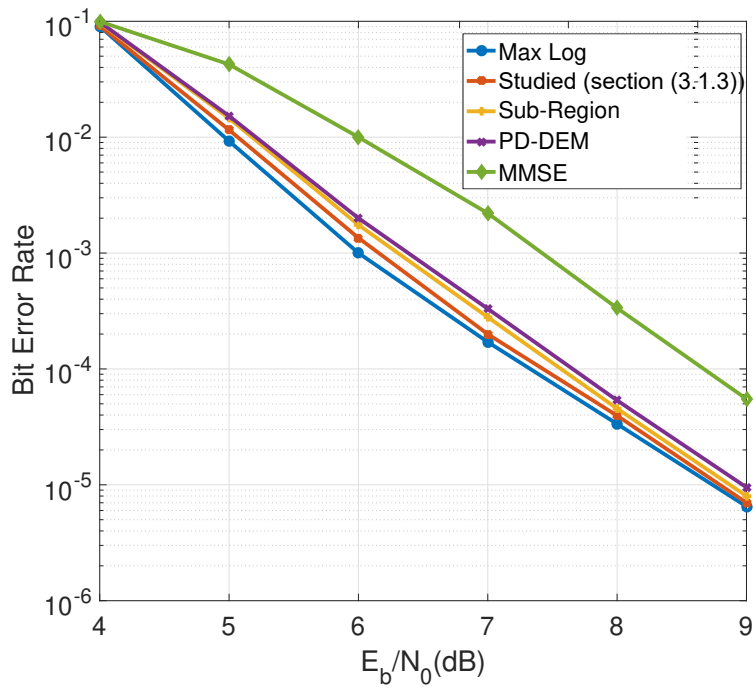


Figure 3.10: BER performance of several algorithms for uniformly projected RCQD 4-QAM signal on underwater channel KAU2

(see [93] and Figure 3.10). We can also note that, among the algorithms studied, the two-dimensional demappers can achieve near-optimal performance. In particular, the studied soft demapping method achieves almost the same performance as the Max-Log algorithm. Moreover, in comparison with the PD-DEM method, the 2D method of lowest complexity in the literature, the studied soft demapping algorithm reduces the complexity and allows better performance.

3.2 Low-Complexity Blind PAPR Reduction for OFDM Systems with Rotated Constellations

As recalled in chapter 2, the OFDM solution can be an alternative to underwater mono-carrier communications for short range (a few hundred meters) stable channels; this is because its good spectral efficiency is paid at the price of a high sensitivity to both synchronization and PAPR problems. The high PAPR of OFDM signals leads to a serious system performance degradation which in particular limits the communication range.

To work around this issue, several algorithms have been proposed in the literature (see chapter 2) to reduce the PAPR, but, they often suffer from multiple limitations; in particular, the main issue with interleaving techniques is the spectral efficiency loss, as the transmission of a Side Information (SI) is generally required.

In contrast to previous works, this section proposes a blind interleaving technique for OFDM systems with Signal Space Diversity (SSD) [96]. Indeed, with Rotated and Cyclically Q-Delayed (RCQD) constellations, the In-phase (I) and Quadrature (Q) components of constellations symbols are correlated, which allows the receiver to estimate the interleaver index without any SI. Moreover, to lower down the complexity burden at the receiver side, we first design a blind decoder based on the Minimum Mean Square Error (MMSE) criterion and we then propose a low complexity decoder for the Uniformly Projected RCQD (UP-RCQD) QAM, as we have shown in the first part of this chapter that this constellation has several interesting structural properties and achieves near optimum BER performance.

3.2.1 Overview of the Proposed Blind PAPR Reduction Technique with SSD

We now describe the communication system depicted in Figure 3.11.

3.2.1.1 At the Transmitter Side

Each message frame is first channel encoded and interleaved; then every block of $N_p (\log_2(M))$ bits are converted into a series of N_p complex-valued M-QAM symbols $s(k)$ (see 3.1) with Gray mapping. Then, the proposed transmitter rotates the QAM symbol as $x(k)$ (see (3.3 and 3.4)). Traditionally, the second step of the RCQD modulation is to cyclically delay

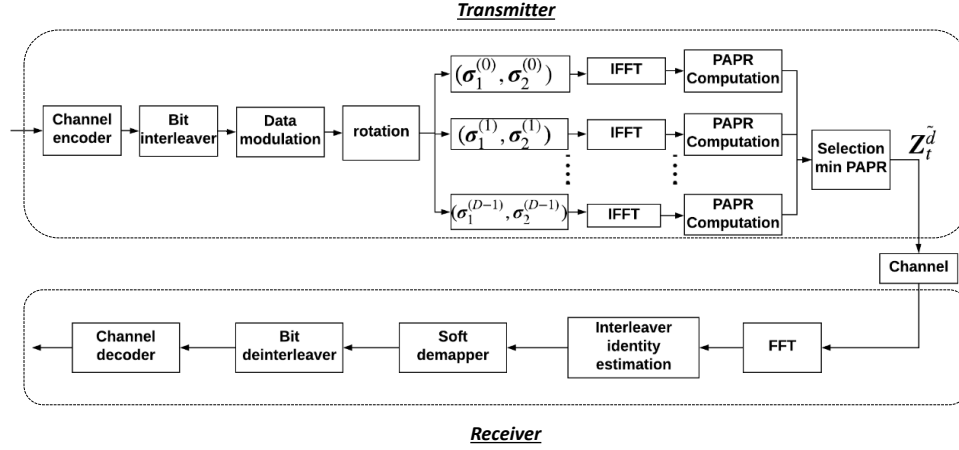


Figure 3.11: System model.

the Q components $x_2(k)$ so that the components $x_1(k)$ and $x_2(k)$ of the rotated symbol $x(k)$ experiment independent channels. In this section, the transmitter possesses an alphabet of D two-component interleavers $\{(\sigma_1^{(d)}, \sigma_2^{(d)}), d = 0, 1, \dots, D-1\}$; the transmitter generates in parallel D OFDM symbols by applying each possible two-component (in-phase and quadrature) interleavers; one thus obtains, for every index d , the sequence:

$$z_f^{(d)}(k) = x_1(\sigma_1^{(d)}(k)) + jx_2(\sigma_2^{(d)}(k)). \quad (3.19)$$

The transmitter then builds in parallel D OFDM symbols:

$$z_t^{(d)}(k) = \sum_{n=0}^{N_p-1} z_f^{(d)}(n) e^{\frac{2\pi n k}{N_p}}. \quad (3.20)$$

Before proceeding to any transmission, for each two-component interleaver $(\sigma_1^{(d)}, \sigma_2^{(d)})$, the transmitter computes the corresponding $PAPR(d)$ as:

$$PAPR(d) = \frac{\max_{k=0, \dots, N_p-1} |z_t^{(d)}(k)|^2}{\mathbb{E}(|\mathbf{Z}_t^{(d)}|)^2}, \quad (3.21)$$

where $\mathbf{Z}_t^{(d)} = (z_t^{(d)}(0), z_t^{(d)}(1), \dots, z_t^{(d)}(N_p-1))^T$ and \mathbb{E} denotes the expectation.

Finally, the transmitter selects index \tilde{d} such that:

$$\tilde{d} = \underset{d=0,1,\dots,D-1}{\operatorname{argmin}} PAPR(d), \quad (3.22)$$

and only delivers the corresponding OFDM symbol at the channel input.

3.2.1.2 Interleaver Estimation at the Receiver Side

The received signal after Fast Fourier Transform (FFT) can be expressed as:

$$y(k) = H(k)z_t^{(\tilde{d})}(k) + n(k), \quad (3.23)$$

where \tilde{d} is the actual interleaver index, $H(k)$ is a Rayleigh random variable with unit variance and $n(k) = n_1(k) + jn_2(k)$, where $n_1(k)$ and $n_2(k)$ are independent zero-mean Gaussian random variables with known variance N_0 . In addition, it is considered that the receiver has a perfect channel state information (CSI).

The receiver first has to deinterleave the received observations according to each possible two-component interleaver $(\sigma_1^{(d)}, \sigma_2^{(d)})$, such that the deinterleaved received signals are:

$$\begin{aligned} r^{(d)}(k) &= r_1^{(d)}(k) + jr_2^{(d)}(k), \\ &= y_1 \left(\left(\sigma_1^{(d)} \right)^{-1} (k) \right) + jy_2 \left(\left(\sigma_2^{(d)} \right)^{-1} (k) \right) \\ &= h_1^{(d)}(k)x_1 \left(\left(\sigma_1^{(d)} \right)^{-1} (\sigma_1^{(\tilde{d})}(k)) \right) \\ &\quad + jh_2^{(d)}(k)x_2 \left(\left(\sigma_2^{(d)} \right)^{-1} (\sigma_2^{(\tilde{d})}(k)) \right) + v^{(d)}(k), \end{aligned} \quad (3.24)$$

where $v^{(d)}(k)$ and $h_m^{(d)}$ (with the index m is in $\{1, 2\}$) have the same statistical model characteristics as $n(k)$ and $H(k)$ respectively.

Two points should be noted; first, in order to have an increased signal space diversity, the two-component interleaver $(\sigma_1^{(d)}, \sigma_2^{(d)})$ must guarantee that the I and Q components of the rotated symbol $x(k)$ experience independent fading channels. Second, in contrast to conventional QAM constellations, with a properly designed rotation angle, the I and Q components of $x(k)$ are correlated. This property inherently allows the receiver to estimate the index of the two-component interleaver used in the broadcast with no side information. Indeed, using the ML criterion, one can estimate,

among the known alphabet of two-component interleavers, the one used in the broadcast such as:

$$\begin{aligned}
\hat{d} &= \underset{d=0,1,\dots,D-1}{\operatorname{argmax}} P(\mathbf{R}^{(d)}) \\
&= \underset{d=0,1,\dots,D-1}{\operatorname{argmax}} \sum_{k=0}^{N_p-1} \log \left(P(r^{(d)}(k)) \right) \\
&= \underset{d=0,1,\dots,D-1}{\operatorname{argmax}} \sum_{k=0}^{N_p-1} \log \left(\sum_{x \in \mathbb{X}} P(r^{(d)}(k)|x) \right),
\end{aligned} \tag{3.25}$$

where $\mathbf{R}^{(d)} = (r^{(d)}(0), r^{(d)}(1), \dots, r^{(d)}(N_p - 1))^T$ and \mathbb{X} is the set of possible rotated symbols. Moreover, from (3.24) the probability $P(r^{(d)}(k)|x)$ can be developed as:

$$P(r^{(d)}(k)|x) = \frac{1}{2\pi N_0} e^{-\sum_{m=1}^2 \left| r_m^{(d)}(k) - h_m^{(d)}(k)x_m \right|^2 / 2N_0}. \tag{3.26}$$

Using the Max-Log approximation in (3.26), (3.25) can then be simply evaluated with Euclidean distances as:

$$\begin{aligned}
\hat{d} &= \underset{d=0,1,\dots,D-1}{\operatorname{argmax}} \sum_{k=0}^{N_p-1} \max_{x \in \mathbb{X}} \left\{ \log \left(P(r^{(d)}(k)|x) \right) \right\} \\
&= \underset{d=0,1,\dots,D-1}{\operatorname{argmin}} \sum_{k=0}^{N_p-1} \min_{x \in \mathbb{X}} \left\{ \sum_{m=1}^2 \left| r_m^{(d)}(k) - h_m^{(d)}(k)x_m \right|^2 \right\}.
\end{aligned} \tag{3.27}$$

After having estimated the interleaver index \hat{d} , the receiver computes the Log-Likelihood Ratio (LLR) of the mapped bits. Finally, the deinterleaved LLR values are fed to the channel decoder in order to estimate the information bits \hat{b} .

3.2.2 Detailed Proposal and Complexity Considerations

We now successively design a low-complexity MMSE-based decoder, enhance the analysis for the case of the Uniformly Projected RCQD QAM and analyze the complexity of the method proposed in section 3.2.1.

3.2.2.1 Low Complexity MMSE-based Decoder

The deinterleaved received observations $r_1^{(d)}(k)$ and $r_2^{(d)}(k)$ in (3.24) can be rewritten as:

$$\begin{pmatrix} r_1^{(d)}(k) \\ r_2^{(d)}(k) \end{pmatrix} = \begin{pmatrix} h_1^{(d)}(k) & 0 \\ 0 & h_2^{(d)}(k) \end{pmatrix} \times \begin{pmatrix} x_1 \left(\begin{pmatrix} \sigma_1^{(d)} \\ \sigma_2^{(d)} \end{pmatrix}^{-1} (\sigma_1^{(\tilde{d})}(k)) \right) \\ x_2 \left(\begin{pmatrix} \sigma_1^{(d)} \\ \sigma_2^{(d)} \end{pmatrix}^{-1} (\sigma_2^{(\tilde{d})}(k)) \right) \end{pmatrix} + \begin{pmatrix} v_1^{(d)}(k) \\ v_2^{(d)}(k) \end{pmatrix}. \quad (3.28)$$

For any interleaver index $d = \tilde{d}$, (3.28) can be developed as:

$$\begin{pmatrix} r_1^{(d)}(k) \\ r_2^{(d)}(k) \end{pmatrix} = \mathbf{A}^{(d)}(k) \times \begin{pmatrix} s_1(k) \\ s_2(k) \end{pmatrix} + \begin{pmatrix} v_1^{(d)}(k) \\ v_2^{(d)}(k) \end{pmatrix}, \quad (3.29)$$

where:

$$\mathbf{A}^{(d)}(k) = \begin{pmatrix} h_1^{(d)}(k) & 0 \\ 0 & h_2^{(d)}(k) \end{pmatrix} \begin{pmatrix} \cos(\theta) & -\sin(\theta) \\ \sin(\theta) & \cos(\theta) \end{pmatrix}. \quad (3.30)$$

With an MMSE decorrelator, we then obtain:

$$s^{MMSE}(k) = (\mathbf{A}^{(d)}(k)^T \mathbf{A}^{(d)}(k) + N_0 \mathbf{I})^{-1} \mathbf{A}^{(d)}(k)^T \begin{pmatrix} r_1^{(d)}(k) \\ r_2^{(d)}(k) \end{pmatrix}, \quad (3.31)$$

where \mathbf{I} is the identity matrix of size 2.

Thereafter, the receiver searches the closest constellation point to $s^{MMSE}(k)$ in terms of Euclidean distance and finds the corresponding rotated symbol $\hat{x}^{MMSE}(k)$.

Finally, the receiver decodes the interleaver index as:

$$\hat{d} = \underset{d=0,1,\dots,D-1}{\operatorname{argmin}} \sum_{k=0}^{N_p-1} \left\{ \sum_{m=1}^2 \left| r_m^{(d)}(k) - h_m^{(d)}(k) \hat{x}_m^{MMSE}(k) \right|^2 \right\}. \quad (3.32)$$

As shown in subsection 3.2.2.3, this algorithm reduces considerably the complexity compared to the Max-Log algorithm (compared to (3.27), there is no minimum to calculate among all the points of the rotated constellation) without any BER degradation for system operating at moderate to high SNR over fading channels; however, this method increases the noise level and its detection performance becomes poor when the 2×2 channel matrix is singular. Such is not

the case for the Uniformly Projected RCQD decoder and in the following subsection, we derive a low-complexity index interleaver decoder for the Uniformly Projected RCQD.

3.2.2.2 Low Complexity Index Estimation for the Uniformly Projected RCQD Constellations

- The Uniformly Projected RCQD transmitted signal

As we have seen in the first part of this chapter, by selecting the rotation angle $\theta = \arctan(1/\sqrt{M})$, the I (resp. Q) components of the rotated symbols are uniformly projected with a uniform minimum distance $d_{\min} = 2 \sin \theta$ along the I (resp. Q) axes. This allows to use a low-complexity demapper that takes advantage of working with integers; indeed, each constellation point x corresponds to a unique 2D integer point $(T_{x,1}, T_{x,2})$ defined as (3.9) and integer pair (p_1, p_2) determined by $T_{x,1}$ (resp. $T_{x,2}$) is (3.10) (resp. (3.11)).

- Low-complexity interleaver index estimation

The received components y_m ($m \in \{1, 2\}$) in (3.23) can first be equalized as follows:

$$y_{eq,m}(k) = T_{x,m}(k) + \frac{n_m}{2H(k) \sin \theta}. \quad (3.33)$$

Similarly to (3.24), from (3.33) the deinterleaved equalized observations can then be expressed as:

$$\begin{aligned} r_{eq}^{(d)}(k) &= h_1^{(d)}(k) T_{x,1} \left(\left(\sigma_1^{(d)} \right)^{-1} (\sigma_1^{(\tilde{d})}(k)) \right) \\ &+ j h_2^{(d)}(k) T_{x,2} \left(\left(\sigma_2^{(d)} \right)^{-1} (\sigma_2^{(\tilde{d})}(k)) \right) + \frac{v^{(d)}(k)}{2H(k) \sin \theta}. \end{aligned} \quad (3.34)$$

The distance term $|r_m^{(d)}(k) - h_m^{(d)} x_m|^2$ in (3.27), where m can either be 1 or 2, can then be rewritten as (see (3.33)):

$$\left| r_m^{(d)}(k) - h_m^{(d)}(k) x_m \right|^2 = (2 \sin \theta)^2 \left| h_m^{(d)}(k) \left(r_{eq,m}^{(d)}(k) - T_{x,m} \right) \right|^2. \quad (3.35)$$

Using (3.35), the Max-Log based decoder (3.27) becomes:

$$\hat{d} = \underset{d=0,1,\dots,D-1}{\operatorname{argmin}} \sum_{k=0}^{N_p-1} \min_{T_x \in \mathbf{T}} \left\{ \sum_{m=1}^2 \left| h_m^{(d)}(k) \left(r_{eq,m}^{(d)}(k) - T_{x,m} \right) \right|^2 \right\}, \quad (3.36)$$

where \mathbf{T} is the set of possible points $T_x = (T_{x,1}, T_{x,2})$.

Eq. (3.36) implies that one needs to find, for each d and each k , the global optimum $T_{opt} = (T_{opt,1}, T_{opt,2})$

defined as:

$$T_{opt} = \min_{T_x \in \mathbf{T}} \left\{ \sum_{m=1}^2 \left| h_m^{(d)}(k) \left(r_{eq,m}^{(d)}(k) - T_{x,m} \right) \right|^2 \right\}. \quad (3.37)$$

Among constellation points, one can easily find the local optimum $Loc_m^{(d)}(k) = (Loc_{m,1}^{(d)}(k), Loc_{m,2}^{(d)}(k))$ that minimizes $\left| h_m^{(d)}(k) \left(r_{eq,m}^{(d)}(k) - T_{x,m} \right) \right|^2$, with m being either 1 or 2, such that (see 3.33):

$$Loc_{m,m}^{(d)}(k) = \begin{cases} 0, & \text{if } r_{eq,m}^{(d)}(k) \leq 0, \\ \text{round} \left(r_{eq,m}^{(d)}(k) \right), & \text{if } 0 \leq r_{eq,m}^{(d)}(k) < (M-1), \\ M-1, & \text{if } r_{eq,m}^{(d)}(k) \geq (M-1). \end{cases} \quad (3.38)$$

For sake of complexity, instead of searching the global 2D optimum in (3.36) among all constellation points, we propose to limit the search to 1D regions centered around $r_{eq,m}^{(d)}(k)$ with radius r_a , where m is in $\{1, 2\}$. For $r_a > 0$, these regions can be expressed as $\tilde{\mathbf{T}}_m^{(d)}(k)$ (see (3.18)), whereas for radius $r_a = 0$, $\tilde{\mathbf{T}}_m^{(d)}(k)$ contains only the local optimum $Loc_m^{(d)}(k)$. Each point T_x within $\tilde{\mathbf{T}}_m^{(d)}(k)$ distinctively locates a pair (p_1, p_2) and this pair distinctively determines a constellation point (s_1, s_2) . Thus, $\tilde{\mathbf{T}}^{(d)}(k) = \tilde{\mathbf{T}}_1^{(d)}(k) \cup \tilde{\mathbf{T}}_2^{(d)}(k)$ has at most $4r_a$ constellation points. In particular, for $r_a = 0$, $\tilde{\mathbf{T}}^{(d)}(k)$ contains the two local optimum points $Loc_1^{(d)}(k)$ and $Loc_2^{(d)}(k)$ that may lead to the same constellation symbol, which is then the global optimum. To summarize, from (3.36) with $\tilde{\mathbf{T}}^{(d)}(k) = \tilde{\mathbf{T}}_1^{(d)}(k) \cup \tilde{\mathbf{T}}_2^{(d)}(k)$ and (3.18), we choose the interleaver index as:

$$\hat{d} = \underset{d=0,1,\dots,D-1}{\operatorname{argmin}} \sum_{k=0}^{Np-1} \min_{T_x \in \tilde{\mathbf{T}}^{(d)}(k)} \left\{ \sum_{m=1}^2 \left| h_m^{(d)}(k) \left(r_{eq,m}^{(d)}(k) - T_{x,m} \right) \right|^2 \right\}, \quad (3.39)$$

We now present the successive steps of the proposed algorithm:

1. For each received component, use (3.33) to transform the received components $y_m(k)$ into equalized versions $y_{eq,m}(k)$.
2. For each received component, locate the region $\tilde{\mathbf{T}}_m^{(d)}(k)$ using (3.18) with radius r_a ; then the distance from $r_{eq,m}^{(d)}(k)$ is computed for all points in $\tilde{\mathbf{T}}_m^{(d)}(k)$.
3. For each d and k , given the one dimensional (1D) distance terms already obtained in step 2, compute the missing 1D distance terms in (3.39) so as to obtain the 2D distance terms from $(r_{eq,1}^{(d)}(k), r_{eq,2}^{(d)}(k))$ for all points in $\tilde{\mathbf{T}}^{(d)}(k)$. The minimum 2D distance in (3.39) is then selected.

4. Using the minimum distances obtained in step 3, the interleaver index \hat{d} can finally be obtained (see (3.39)).

3.2.2.3 Complexity Analysis

The detailed analysis on the complexity of the proposed algorithms is evaluated in terms of Real Multiplications (RM), Real Comparisons (RC), Real Inversions (RI) and Real Sums (RS), where RS can either designate a real addition or a real subtraction.

At the transmitter side, note that no multiplication by any phase sequence is required for our proposal; this reduces the complexity burden by $4N_p(D - 1)$ RMs and $2N_p(D - 1)$ RSs compared to the SLM algorithm in [97, 98].

Furthermore, at the receiver side, the total computational complexity of the proposed MMSE-based blind detector (see equations (3.30)-(3.32)) is $38DN_p$ RMs, $15DN_p$ RSs, $(2\log_2 M - 2)DN_p$ RCs, and DN_p RIs.

We now detail the complexity of the index interleaver decoder proposed for the Uniformly Project RCQD (i.e. (3.39)):

1. Equalizing one received component $y_m(k)$ into $y_{eq,m}(k)$ (see 3.33), requires 1 RM, 1 RS and 1 RI. Therefore, equalizing the received observations requires a total of N_p RM, $2N_p$ RSs and $2N_p$ RIs (i.e. $2\sin\theta$ is a known constant term and its multiplication by $H(k)$ is performed only once).
2. Locating the region $\tilde{\mathbf{T}}_m^{(d)}(k)$ requires 2 RCs. Computing a 1D Euclidean distance requires 2RM and 1 RS. Therefore, this step takes a total of $4N_p r_a$ (resp. $2N_p$) RMs, $2N_p r_a$ (resp. N_p) RSs and $4N_p$ RCs.
3. In step 3, for each d and each k , at least $4r_a$ (resp. $2r_a$) 1D distance terms like $\left| h_m^{(d)}(k) \left(r_{eq,m}^{(d)}(k) - T_{x,m} \right) \right|^2$ have already been computed in step 2; thus computing the other $4r_a$ (resp. $2r_a$) 1D distance terms requires a total of $8r_a N_p D$ (resp. $4N_p D$) RMs and $4N_p r_a$ (resp. $2N_p$) RSs for $r_a > 0$ (resp. $(r_a = 0)$). Moreover, obtaining the 2D Euclidean distance terms requires an additional $4DN_p r_a$ (resp $2DN_p$) RS. Finally, selecting the minimum 2D Euclidean distances terms requires $DN_p(4r_a - 1)$ (resp. DN_p) RCs.
4. In step 4, performing the sum of minimum distances requires $(N_p - 1)D$ RS and selecting \hat{d} requires $D - 1$ RCs.

Two points should be noted; first, the proposed PAPR reduction algorithm can be used with any RCQD signals with inherent increased modulation diversity. Second, for the proposed blind PAPR reduction technique, the choice of the rotation angles $\theta = \arctan(1/\sqrt{M})$ lowers down the complexity twice; on one side, the soft demapper detailed in the first part of this chapter can be deployed at the receiver end, as we saw that its complexity is low; moreover, both the first and the second step of the proposed estimation technique are already necessary for the detailed UP-RCQD demapping solution; therefore, the additional complexity related to the interleaver estimation is just $8r_a N_p D$ (resp. $4N_p D$) RMs, $(8r_a + 1)N_p D - D$ (resp. $N_p D$) RSs and $(4r_a - 1)N_p D + D - 1$ (resp. $(N_p + 1)D - 1$) RCs for $r_a > 0$ (resp. for $r_a = 0$).

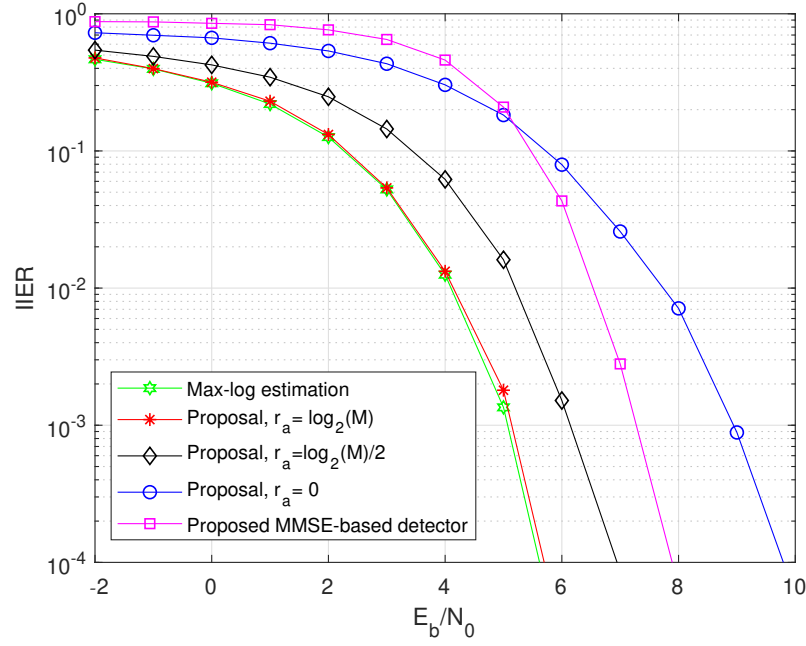


Figure 3.12: Interleaver Index Error Rate comparison between the full complexity Max-Log estimator, the proposed MMSE-based detector and the method for UP-RCQD constellations for several radii r_a (16-QAM, $N = 256$ and $D = 16$).

3.2.3 Simulation Results

Figure 3.12 presents the Interleaver Index Error Rate (IIER) obtained with the Max-Log decoder and the proposed techniques (see (3.27), (3.32), (3.36) and (3.39)) for several radii r_a without any channel coding. It can be observed that there is roughly no difference between the proposed method with $r_a = \log_2 M$ and the full complexity Max-Log decoder. Moreover, the performance deteriorates with the diminution of the radius; in particular, the proposed method with a radius $r_a = 0$ respectively loses about 4 dB compared to the full-complexity Max-Log estimation and 2 dB compared to the MMSE based detector but it still operates at rather low SNR.

In the sequel, otherwise mentioned, we fix the following parameters : $N = 256$, $D = 16$ and 64-QAM. Figure 3.13 compares the BER performance of the considered methods and the case where the receiver has an ideal SI of the interleaver index for several constellation sizes. In coherence with Figure 3.12, for a system operating at moderate to high SNR regime, the considered methods lead to a low IIER and therefore to the same overall BER performance.

Considering both the transmitting and the receiving ends, Figure 3.14 compares the total computational complexity, at both the transmitting and the receiving ends, between the Max-Log estimator, the MMSE-based detector and the proposed method for UP-RCQD constellations for several radii r_a (see Table 3.3 [52]); we assume that the cost of RC or RS is one, whereas, the cost of RM and RI are two and four respectively. First, we observe that the computational

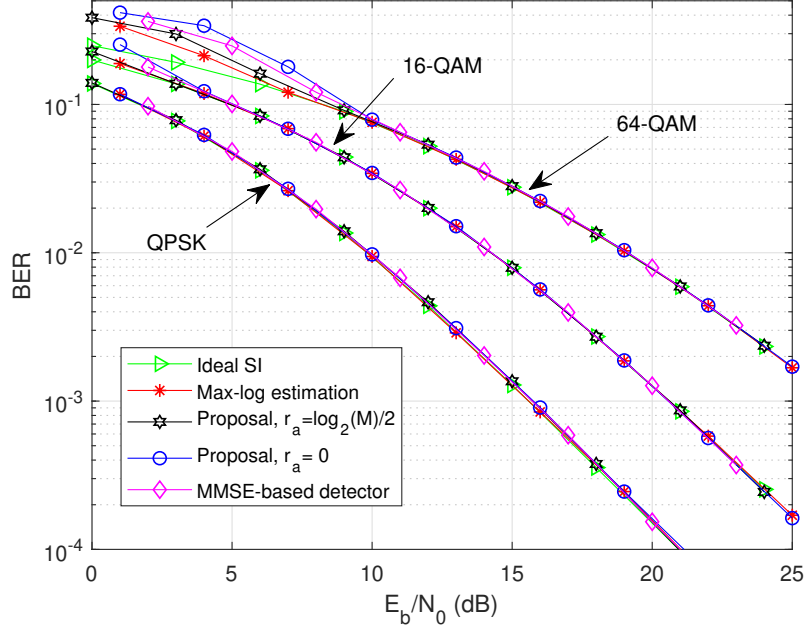


Figure 3.13: BER comparison between the ideal RSI, the full complexity Max-Log estimator, the proposed MMSE-based detector and the method for several radii r_a over the Rayleigh channel ($N = 256$, $D = 16$).

complexity of our proposal increases with the radius and that the complexity of the Max-Log estimation is much higher than that of our section 3.2.2 proposals. For $M = 256$, the MMSE-based detector achieves a 86% of complexity reduction compared to the Max-Log estimation. With the chosen system parameters, our proposal with $r_a = 0$ achieves a 96% of complexity reduction compared to the MMSE-based detector; similarly, we obtain 84% of complexity reduction for the 4-QAM.

Moreover, Figure 3.15 presents for $N_p = 128$ the Complementary Cumulative Distribution Function (CCDF) of the PAPR obtained by the proposed technique (with $D = 2, 4, 8, 16$), the TR algorithm defined in DVB-T2 [79] (with a clipping threshold of 7 dB and 16 iterations), the clipping technique (with clipping level at 75% of the maximum of the original OFDM symbols) and the optimal PTS (with $S = 16$ sub-blocks and rotation angles $\{0, \pi\}$). It can be observed that for any D larger than 2, our proposal achieves a better PAPR reduction than the TR algorithm. Note that, in contrast to the TR technique, our proposal avoids any spectral spoilage. Moreover, the proposed method outperforms the clipping technique for any D larger than 4. It is worth mentioning that the clipping technique may lead to a serious BER degradation, especially for low clipping thresholds [39]. Furthermore, the optimal PTS allows a good PAPR reduction performance; however, this gain is obtained at the expense of a high exponential complexity in S and a large side information; therefore, several low-complexity PTS schemes have been proposed but they may lead to suboptimal PAPR reduction performance [99]. Besides, when we jointly use the TR and the proposed algorithms with $D = 8$, we obtain

Table 3.3: Comparison of total computational complexities (M1: Max-Log, M2: MMSE-based detector, M3: Proposal, $r_a > 0$, M4: Proposal, $r_a = 0$ and M5: ML, blind SLM).

	RS	RC
M1	$DN_p(3M + 1) - D$	$D(N_p(M - 1) + 1) - 1$
M2	$15DN_p$	$DN_p(2\log_2 M - 2)$
M3	$(N_p(2 + r_a(2 + 8D) + D) - D$	$(4 + D(4r_a - 1))N_p + D - 1$
M3	$N_p(3 + 5D) - D$	$(N_p + 1)D - 1$
M5	$DN_p(3 + 3M)$	$D - 1$

	RM	RI
M1	$4N_pMD$	0
M2	$38N_pD$	DN_p
M3	$N_p(1 + r_a(4 + 8D))$	$2N_p$
M4	$N_p(3 + 4D)$	$2N_p$
M5	$D(N_p^4 + 2M)) + 1$	0

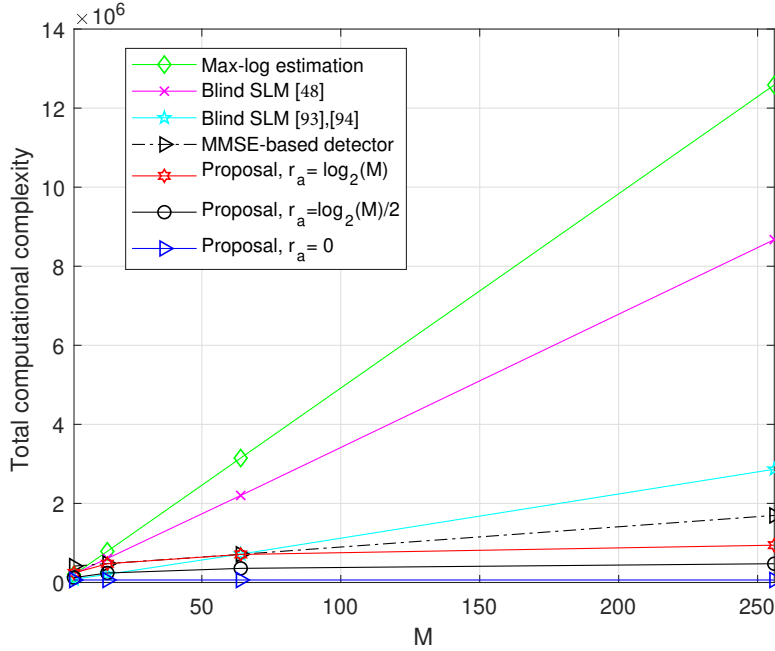


Figure 3.14: Computational complexity comparison for $N_p = 256$ and $D = 16$.

similar PAPR reduction performance to the optimal PTS with much lower computational complexity and higher spectral efficiency. Finally, when compared to the blind SLM method [97, 98], both methods have approximately the same PAPR reduction performance; however, our proposal for UP-RCQD constellations reduces considerably the computational complexity both at the transmitter and the receiver sides; in particular, in addition to the computational complexity reduction obtained for the LLR computation thanks to the use of the UP-RCQD constellation, the computational complexity is reduced, with the chosen system parameters, by 97% (see Table 3.3 and Figure 3.14).

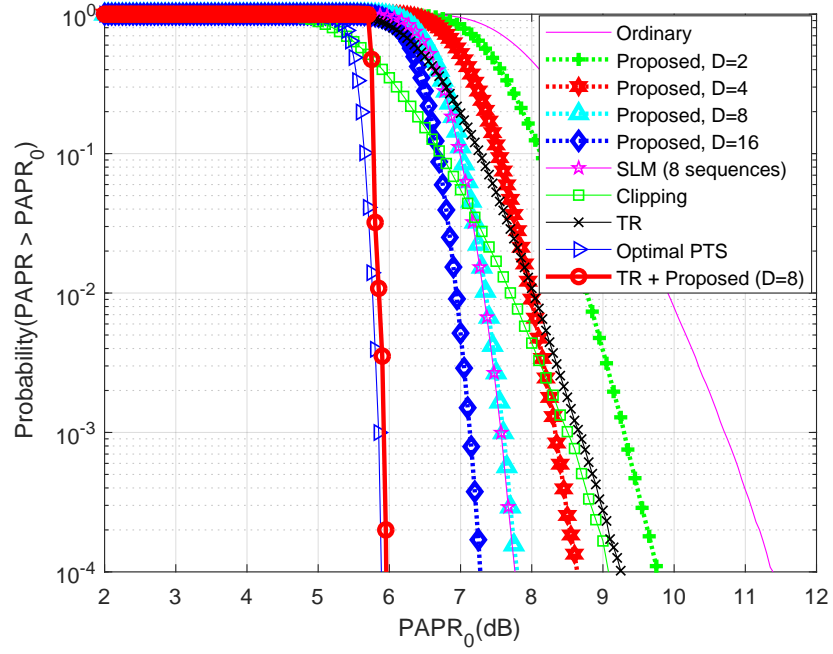


Figure 3.15: CCDFs of the PAPR for the 64-QAM constellation and $N_p = 128$.

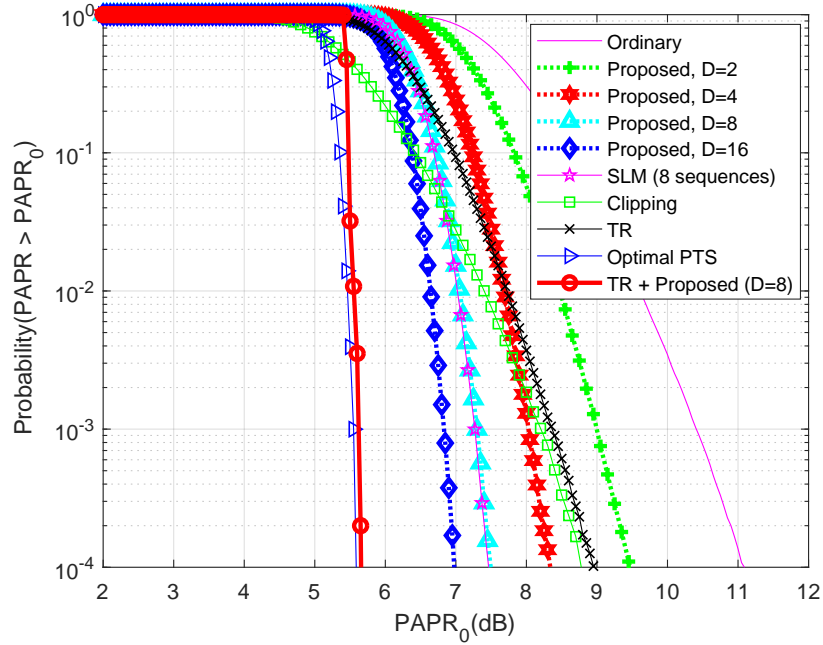


Figure 3.16: CCDFs of the PAPR for the 16-QAM constellation and $N_p = 64$.

Finally, Figure 3.16 confirms the results of Figure 3.15 for other system parameters.

3.3 Conclusion

In this chapter, we studied a series of rotation angles $\theta = \arctan(1/\sqrt{M})$ with interesting structural properties for different RCQD signals. Based on these properties, we reviewed a low complexity demapper for fading channels that gives almost the same performance as the optimal Max-Log algorithm. Thanks to the good performance of the proposed angles and the simplicity of the proposed demapper implementation, the spectral efficiency and the energy consumption of the underwater communication system can be enhanced. It is important to note that the inherent signal diversity explored without bandwidth expansion could in turn save even more bandwidth by allowing the use of a higher rate channel code.

Furthermore, this chapter proposes a new blind interleaving technique for PAPR reduction without any distortion for OFDM systems using signal space diversity. It is based on the use of rotated constellations as they allow the receiver to identify, without any SI, the two-component interleaver used in the broadcast. To lower down the complexity burden at the receiver side, an MMSE-based detector with good performance is proposed. Furthermore, in order to reduce even more the computation complexity of the demapper, we propose to use again the UP-RCQD constellation as this constellation brings many interesting structural properties that we employ to design a low-complexity interleaver index decoder. The main advantages of this technique are as following. Our proposal achieves a large PAPR reduction performance without neither BER degradation, nor any spectral spoilage. In addition, compared to the blind SLM method, the proposed technique simplifies both the transmitter and the receiver design and its low-complexity makes it particularly suited for hardware implementation.

We assumed at the beginning of the chapter that synchronization and equalization were achieved. In the next chapter we will make more proposals to improve both synchronization and equalization.

Chapter 4

Equalization techniques for the time-varying underwater acoustic channel

Contents

4.1 Low-Complexity Adaptive Turbo Equalization for Multipath Underwater Communication	97
4.1.1 System Model	98
4.1.2 Adaptive Turbo Equalization	99
4.1.2.1 Adaptive Equalizer Algorithm	99
4.1.2.2 Symbol to Bit Converter (SBC)	100
4.1.2.3 Bit to Symbol Converter (BSC)	101
4.1.3 Numerical Results	101
4.1.3.1 Complexity Analysis	101
4.1.3.2 WATERMARK	102
4.1.3.3 Time-varying Channels	104
4.2 Fully Adaptive Equalizer for Fast-varying Doubly Selective Channels	105
4.2.1 The Proposed Adaptive Turbo Equalizer	106
4.2.1.1 Equalizer Structure	106
4.2.1.2 Adaptive Step-size Optimization	108
4.2.2 Simulation Results	112
4.3 Conclusion	116

The underwater channel is one of the most challenging channels as the acoustic signal may suffer from both a very limited coherence bandwidth and from high Doppler effect. In particular the multipath propagation introduce ISI that can seriously limit the system performance. Following the discovery of turbo decoding, iterative equalization has been proposed to remove ISI, as the equalizer and the channel decoder can mutually exchange extrinsic information at each iteration so as to enhance their performances. The phase recovery is yet another issue that the receiver needs to cope with, particularly in the case of an important Doppler drift. Nevertheless, the complexity of the theoretical turbo-equalization scheme [90] grows exponentially with the communication parameters, which prohibits its use in real life applications; also, for a channel with time-varying characteristics, conventional turbo equalization algorithm using constant step-sizes are unable, by construction, to achieve some satisfying pursuit performances and thus a good trade-off between the performance and convergence speed. To cope with these issues, this chapter presents two different and original algorithms for joint equalization and phase estimation. It is divided in two main sections.

The first section proposes a sparse adaptive turbo detector with only a few taps to be updated in order to lower down the complexity burden. It is organized as follows: the first subsection introduces the adaptive turbo equalization system model; then, the adaptive equalizer structure is presented in the second subsection, the detailed analysis on the complexity of the algorithm and BER performance of the proposed algorithm on both underwater channels and a synthetic channel are given in the last subsection.

The second section of this chapter proposes an original self-optimized equalizer for which the step-sizes of both the equalizer and the phase estimator are updated adaptively and assisted by soft-information provided by the channel decoder in an iterative manner. This second section is organized as follows: the first subsection details the algorithm of the proposed technique and outlines how the proposed equalizer works; some simulation results are shown in the following subsection. Finally, we draw conclusions at the end of this chapter.

4.1 Low-Complexity Adaptive Turbo Equalization for Multipath Underwater Communication

This section proposes a low-complexity turbo equalization with only a few coefficients to be updated [100]. This is because the complexity of an ordinary filter can be prohibitive over long channel impulse responses and as many taps of the transversal filters are often useless to equalize the channel [101, 102].

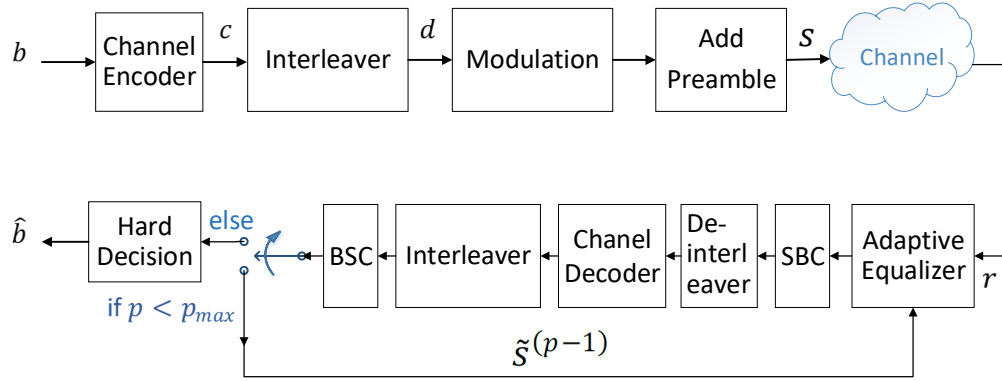


Figure 4.1: System model

4.1.1 System Model

The transmission scheme is displayed in Fig. 4.1. The channel encoder is a systematic parallel convolutional turbo code of rate $1/3$ with generator polynomials (in octal form) equal to $(5, 7)$; similar results would be obtained with polar codes, LDPC codes or product turbo codes [103–111]. This channel encoder system is used to encode at rate R_c the information bits b at the transmitter side. To increase the code diversity, the coded bits are interleaved and then each set of $m = \log_2 M$ interleaved coded bits d are mapped into an M-QAM complex symbols. It is worth mentioning that in practice a preamble, known by the receiver, is usually added at the beginning of each frame. Indeed, this preamble is essential for the frame detection and the good convergence of the adaptive synchronization and equalization. The obtained signal s is finally transmitted through the channel. The received signal at the output of the discrete time-varying channel can be written as:

$$r_k = \sum_l h_l(k) s_{k-l} + w_k, \quad (4.1)$$

where at time index k , $h_l(k)$ indicates the channel response, and w_k is a Gaussian noise with known variance σ_w^2 .

At the receiver side, several signal processing algorithms are needed in order to correctly recover the transmitted frame. In this subsection, we focus on the design of an algorithm performing jointly the equalization and the phase synchronization [112]. As detailed in the following subsection, the phase estimation is carried out separately from the equalization process as it changes more rapidly than the timing synchronization which is assumed to be perfect [113–117] in the sequel. Note that if phase synchronization [118–125] was not separated from the equalization, there would be an additional difficulty to update timely all the equalization coefficients to follow rapid channel variations; in addition, digital PLL phase synchronization techniques are able to work near optimum Cramer-Rao bounds [126–132].

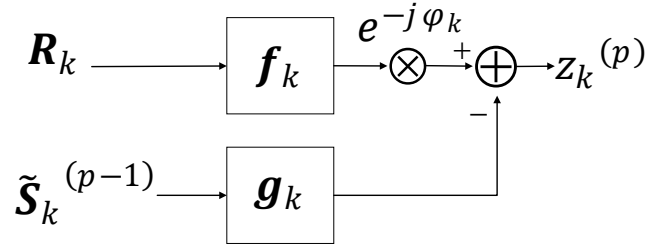


Figure 4.2: Joint equalizer and phase estimator structure

4.1.2 Adaptive Turbo Equalization

4.1.2.1 Adaptive Equalizer Algorithm

Fig. 4.2 describes a joint equalizer and phase estimator structure. It includes two transversal filters \mathbf{f}_k and \mathbf{g}_k fed in by the received signal sequence $\mathbf{R}_k = [r_{k+L_1}, \dots, r_{k-L_1}]^T$ and the symbol sequence $\tilde{\mathbf{S}}_k = [\tilde{s}_{k+L_2}, \dots, \tilde{s}_{k-L_2}]^T$ respectively for each iteration p , where \tilde{s}_k denotes either the known preamble during the training period or the soft estimated symbol at the previous iteration for $p > 1$ during the tracking period.

In order to simplify the notation, the index (p) is dropped in this subsection. The output of the equalizer can be expressed as:

$$z_k = \mathbf{f}_k^T \mathbf{R}_k e^{-j\varphi_k} - \mathbf{g}_k^T \tilde{\mathbf{S}}_k, \quad (4.2)$$

where $\mathbf{f}_k = [f_{-L_1}(k), \dots, f_{L_1}(k)]^T$ (resp. $\mathbf{g}_k = [g_{-L_2}(k), g_0(k) = 0, \dots, g_{L_2}(k)]^T$) is a transversal filter equalizer of length $2L_1 + 1$ (resp. $2L_2 + 1$), and φ_k is the estimated phase error. The coefficients of the filters are updated in order to minimize the estimated Mean-Square Error (MSE) given by:

$$J(\mathbf{f}_k, \mathbf{g}_k, \varphi_k) = \mathbb{E} \left\{ |z_k - \tilde{s}_k|^2 \right\}, \quad (4.3)$$

where $\mathbb{E}(d)$ designates the expectation of d . Similarly to [89] and [133], the derivation of J with respect to \mathbf{f}_k , \mathbf{g}_k and φ_k leads to the following gradients:

$$\begin{cases} \nabla_{\mathbf{f}_k} (|z_k - \tilde{s}_k|^2) &= 2(z_k - \tilde{s}_k) \mathbf{R}_k^* e^{j\varphi_k} \\ \nabla_{\mathbf{g}_k} (|z_k - \tilde{s}_k|^2) &= -2(z_k - \tilde{s}_k) \tilde{\mathbf{S}}_k^* \\ \nabla_{\varphi_k} (|z_k - \tilde{s}_k|^2) &= 2\Im \left(\mathbf{f}_k^T \mathbf{R}_k e^{-j\varphi_k} (z_k - \tilde{s}_k)^* \right) \end{cases}, \quad (4.4)$$

where $()^*$ designates the conjugate and $\Im(d)$ designates the imaginary part of d .

Using the gradient descent algorithm, we obtain the corresponding update coefficients expressed as:

$$\mathbf{f}_{k+1} = \mathbf{f}_k - \mu (z_k - \tilde{s}_k) \mathbf{R}_k^* e^{i\varphi_k} \quad (4.5)$$

$$\mathbf{g}_{k+1} = \mathbf{g}_k + \mu (z_k - \tilde{s}_k) \tilde{\mathbf{S}}_k^* \quad (4.6)$$

$$\varphi_{k+1} = \varphi_k - \gamma \Im \left(\mathbf{f}_k^T \mathbf{R}_k e^{-i\varphi_k} (z_k - \tilde{s}_k)^* \right), \quad (4.7)$$

where μ and γ are the appropriate step sizes. It is worth to note that the channel response of the underwater channel can be particularly large; thus, in order to have an efficient equalization, as L_1 and L_2 are proportional to the channel response and can also be large enough, equation (4.5) and (4.6) may lead to a high computational complexity.

Consequently, after the training period, we propose to keep a certain predefined percentage of the filters coefficients with the highest energy and set the others to zero. The new sparse transversal filters are labeled in the sequel as \mathbf{f}'_k and \mathbf{g}'_k .

4.1.2.2 Symbol to Bit Converter (SBC)

The role of the SBC (see Fig. 4.1) is to compute the LLR value of the coded bits from the equalized symbol z_k which will be transmitted to the soft-input soft-output channel decoder. z_k can be decomposed as the sum of two parts [134]:

$$z_k = g_0 \tilde{s}_k + \nu_k, \quad (4.8)$$

where $g_0 \tilde{s}_k$ is the desired signal with a bias factor g_0 , ν_k is the sum of the noise and residual interference at the output of the equalizer. Assuming a Gaussian distribution of the residual ISI, ν_k follows a complex Gaussian distribution with zero mean and variance $\sigma_v^2 = \sigma_s^2 g_0 (1 - g_0)$, where $0 \leq g_0 < 1$ and σ_s^2 is the signal \tilde{s} variance [89, 134]. The extrinsic LLRs of the mapped bits $l^i(s)$, ($i = 0, 1, \dots, \log_2 M - 1$) are:

$$LLR(l^i(s)) = \ln \frac{\sum_{x \in \chi_b^1} \exp \left(-\frac{|z_k - g_0 x|^2}{\sigma_v^2} \right)}{\sum_{x \in \chi_b^0} \exp \left(-\frac{|z_k - g_0 x|^2}{\sigma_v^2} \right)}, \quad (4.9)$$

where $l^i(s)$ is the i -th bit of symbol s and χ_b^i denotes the set of the constellation points whose i -th bit is $b = 1$ or 0 .

4.1.2.3 Bit to Symbol Converter (BSC)

For all $p > 1$, one calculates the estimated value $\bar{s}_k^{(p-1)}$ from the BSC using the output LLR values of the channel decoder at the iteration $p - 1$. The soft estimation \bar{s}_k is given by [134]:

$$\bar{s}_k^{(p-1)} = \sum_{x \in \chi} x \cdot \left(\prod_{i=1}^{\log_2 M} \Pr \left(l^i(s_k) = l^i(x) \right) \right), \quad (4.10)$$

where χ refers to the signal constellation set. $\Pr(d)$ represents the probability of d and the product over each bit gives the probability of the corresponding symbol. The term $\Pr \left(l^i(s_k) = j \right)$ where j can either be 0 or 1 can be written as [134]:

$$\begin{aligned} \Pr \left(l^i(s_k) = 1 \right) &= \frac{\exp \left(\text{LLR} \left(l^i(s_k) \right) \right)}{1 + \exp \left(\text{LLR} \left(l^i(s_k) \right) \right)} \\ \Pr \left(l^i(s_k) = 0 \right) &= 1 - \Pr \left(l^i(s_k) = 1 \right). \end{aligned} \quad (4.11)$$

4.1.3 Numerical Results

This subsection first presents the computational complexity of our proposed algorithm. Thereafter, we presents the performance of our algorithm in terms of BER over some underwater acoustic channels and also over a synthetic channel.

4.1.3.1 Complexity Analysis

The detailed analysis on the complexity of the algorithm is evaluated in terms of Real Multiplication (RM) and Real Sum (RS), where a RS can either be a real addition or a real subtraction.

- In equation (4.2) : Multiplying the \mathbf{f}_k vector by \mathbf{R}_k requires $3(2L_1 + 1) + 4L_1$ RSs and $4(2L_1 + 1)$ RMs, then multiplying the term $\left(\mathbf{f}_k^T \mathbf{R}_k \right)$ by $e^{-i\varphi_k}$ needs 3RSs and 4RMs. Similarly, multiplying the \mathbf{g}_k vector by $\tilde{\mathbf{S}}_k$ requires $3(2L_2 + 1) + 4L_2$ RSs and $4(2L_2 + 1)$ RMs. Therefore, equation (4.2) takes a total of $10L_1 + 10L_2 + 11$ RSs and $8L_1 + 8L_2 + 12$ RMs.
- In equation (4.5): Computing $\mu(z_k - \tilde{s}_k)$ requires 2RSs and 2RMs, multiplying it with $e^{-i\varphi_k}$ needs 3RSs and 4RMs. Multiplying the previous product by \mathbf{R}_k^* requires $3(2L_1 + 1)$ RSs and $4(2L_1 + 1)$ RMs. Thus, equation (4.5) needs globally $10L_1 + 8$ RSs and $8L_1 + 10$ RMs.

- In equation (4.6): The multiplication with \tilde{S}_k^* requires $3(2L_2 + 1)$ RSs and $4(2L_2 + 1)$ RMs. Thus, equation (4.6) requires a total of $10L_2 + 5$ RSs and $8L_2 + 4$ RMs.
- In equation (4.7): It takes 3RSs and 4RMs to multiply with $(z_k - \tilde{s}_k)^*$. Thus, equation (4.7) totally requires 4RSs and 5RMs.
- In equation (4.10): The product of the term $Pr(l^i(s_k) = l^i(x))$ needs $2M \log_2 M$ RMs. Thus, equation (4.10) requires a total amount of $2M$ RSs and $2M \log_2 M$ RMs.

Therefore, performing the full complexity equalization of a symbol globally requires $(20L_1 + 20L_2 + 28 + 2M)$ RSs and $(16L_1 + 16L_2 + 31 + 2M \log_2 M)$ RMs, while performing the sparse proposal of a symbol in tracking period requires $(20L'_1 + 20L'_2 + 28 + 2M)$ RSs and $(16L'_1 + 16L'_2 + 31 + 2M \log_2 M)$ RMs, where $(2L'_1(\text{resp. } L'_2)+1)$ is the number of non-zero coefficients of the filter f'_k (resp. g'_k).

Table 4.1 compares the complexity between the full complexity equalizer and the sparse proposal with p_{max} iterations and N_s (resp. N_{pre}) corresponds to the number of symbols transmitted (resp. preamble).

	Real Multiplications	Real Sums
Full complexity equalizer	$(16L_1 + 16L_2 + 31) N_{pre} +$ $(16L_1 + 16L_2 + 31) p_{max} (N_s - N_{pre})$ $+ 2M \log M (p_{max} - 1) N_s$	$(20L_1 + 20L_2 + 28) N_{pre} +$ $(20L_1 + 20L_2 + 28) p_{max} (N_s - N_{pre})$ $+ 2M (p_{max} - 1) N_s$
Sparse proposal	$(16L_1 + 16L_2 + 31) N_{pre} +$ $\left(16L'_1 + 16L'_2 + 31\right) p_{max} (N_s - N_{pre})$ $+ 2M \log M (p_{max} - 1) N_s$	$(20L_1 + 20L_2 + 28) N_{pre} +$ $\left(20L'_1 + 20L'_2 + 28\right) p_{max} (N_s - N_{pre})$ $+ 2M (p_{max} - 1) N_s$

Table 4.1: Complexity comparison between the proposed sparse adaptive and the full complexity equalizers

4.1.3.2 WATERMARK

In our simulations, user frames of 2048 bits are coded with a turbo code of rate 1/3 with generator polynomials equal to $(5, 7)_{octal}$. A training sequence made of 511 symbols is added before each user frame for both frame detection and convergence of the equalizer. The information is transmitted at a bit rate of roughly 2 kbit/s (QPSK) and 4 kbit/s (16-QAM) at a 14 kHz (resp. 35 kHz) carrier frequency over the channel NOF1 (resp. BCH1). At the first iteration, the number of taps for f_k and g_k are equal to 41 and 51 respectively, the central coefficient of f_k is set to 1; γ is set to 0.08 (see equation (4.7)). In the training (resp. tracking) period μ is equal to 0.003 (resp. 0.0005) (see equations (4.5))-

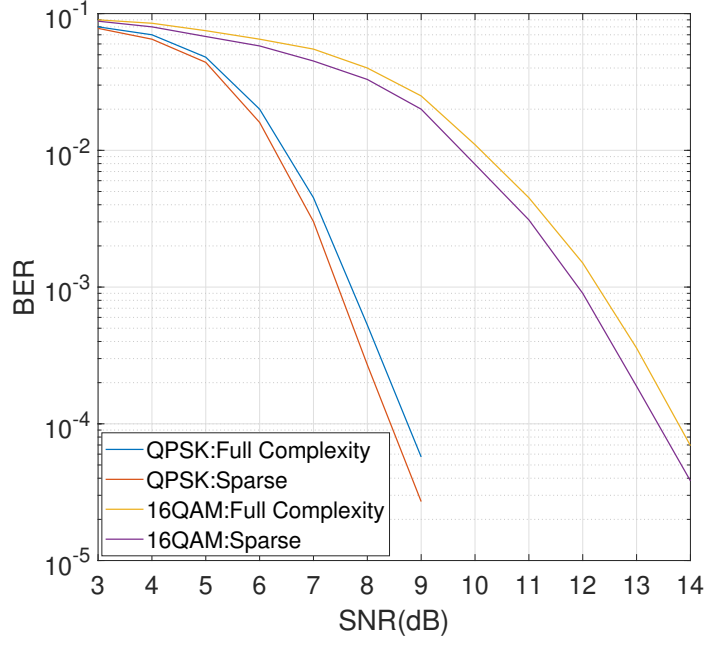


Figure 4.3: BER comparison between the full complexity equalizer and the proposed one over the channel NOF1

(4.6)). The number of turbo equalization is $p_{max}=10$. In the tracking period, the sparse equalizer turns off 30 (resp. 38) among the 41 (resp. 51) coefficients of f_k (resp. g_k).

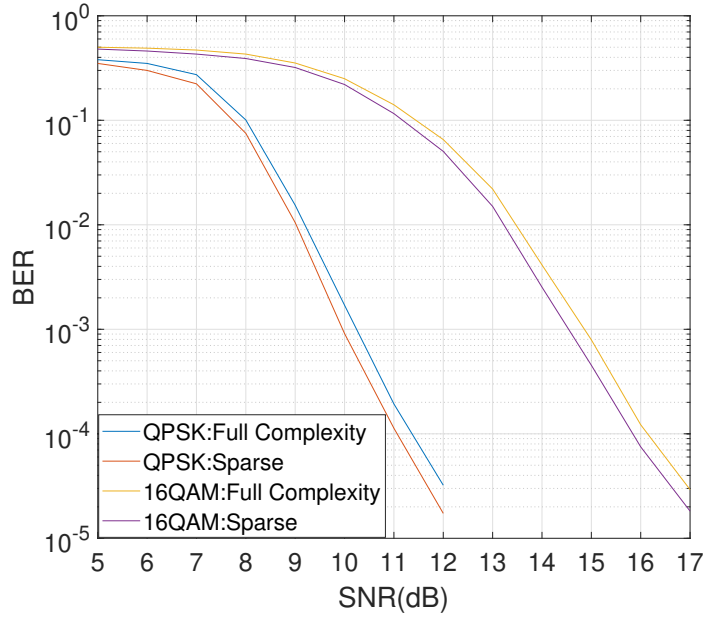


Figure 4.4: BER comparison between the full complexity equalizer and the proposed one over the channel BCH1

Fig. 4.3 (resp. Fig. 4.4) compares the BER performance between the full complexity algorithm and the sparse proposal for the QPSK and 16-QAM constellations over the channel NOF1 (resp. BCH1) (see table 3.1). The coherence time (resp. the symbol duration) is equal to 102 ms (resp. 0.35 ms) for the channel BCH1. It can be observed that our sparse proposal allows a BER performance improvement of about 0.4 (resp. 0.3) dB. This is because small coefficients of the full complexity equalizer add supplemental unwanted noise to z_k and are weakly related to the channel. Furthermore, compared to the full complexity equalizer, the computational complexity is reduced by 70%.

4.1.3.3 Time-varying Channels

We now consider the channel given by [89]:

$$h_l(k) = \sqrt{\frac{P_l}{I}} \sum_{i=1}^I e^{j(k\epsilon\pi \cos \psi_{l,i} + \zeta_{l,i})}, \quad (4.12)$$

where the Doppler shift is characterised by ϵ , P_l denotes the mean power of the l -th channel path, $\psi_{l,i}$ and $\zeta_{l,i}$ are uniform random variables over $[0, 2\pi]$; I is fixed to 10 and (4.12) has three paths having all the same mean power [89] in our simulation.

In our simulations, the information data were encoded by the same 1/3 rate turbo code, a preamble of 25 symbols is added at the beginning of each packet of 100 symbols. All packets are successively transmitted over the continuously varying Rayleigh multipath channel (4.12). At the first iteration, the number of taps for the transversal filter of received signal f_k is equal to 21, and the central coefficient of f_k is set to 1; in the training (resp. tracking) period μ is equal to 0.001 (resp. 0.0003) (see equations (4.5)- (4.6)), γ is set to 0.01 (resp. 0.006) (see equation (4.7)). After the feedback of the turbo-decoder, during each iteration, the number of taps of f_k and g_k are respectively equal to 21 and 31; in the training (resp. tracking) period μ is equal to 0.001 (resp. 0.0002), and γ is set to 0.01 (resp. 0.006). The number of turbo equalization is $p_{max} = 10$. In the tracking period, the sparse equalizer turns off 14 (resp. 21) among the 21 (resp. 31) coefficients of f_k (resp. g_k). Thus, the number of non-zero coefficients f'_k and g'_k are 7 and 9 respectively.

Fig. 4.5 compares the BER performance between the full complexity algorithm and the proposed sparse technique, with and without phase synchronization respectively, for the QPSK constellation over the Rayleigh multipath channel. It can be observed that our sparse algorithm allows a BER performance improvement of about 0.3dB compared with the full complexity algorithm, and in addition, performing phase synchronization separately with equation (4.7) allows an additional gain of 0.5dB. Finally, compared to the full complexity equalizer, the computational complexity is reduced by 60%.

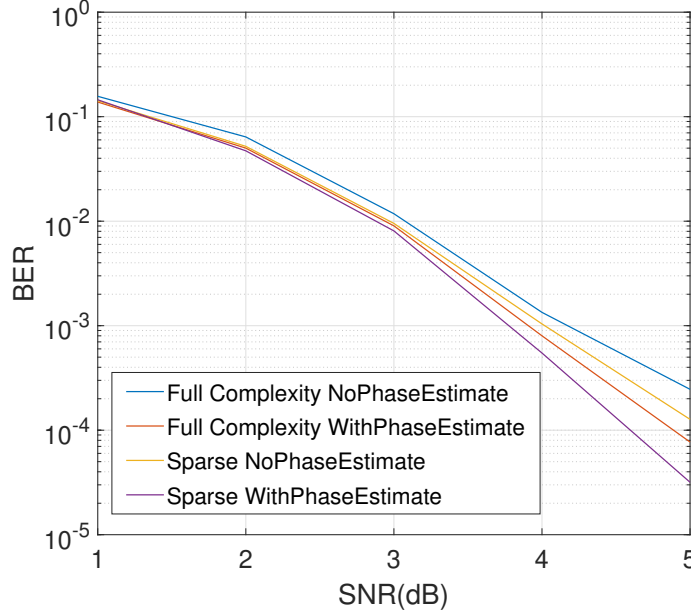


Figure 4.5: QPSK BER comparison between the full complexity equalizer and the proposed one, with and without phase synchronization over the Rayleigh multipath channel (4.12)

4.2 Fully Adaptive Equalizer for Fast-varying Doubly Selective Channels

Up to this point, our goal was to consider low-complexity algorithms for the Internet-of-Things applications. In particular, the standard iterative equalization (see chapter 2) algorithm is often used in real-time estimation thanks to its low-complexity. However, the performance of such technique depends on its constant step-size; in particular, the step-size controls both the convergence speed and the steady-state mean square error of the algorithm; if the step-size is chosen too small, the convergence speed is too slow, but if it is chosen too large, the steady state MSE is poor. In addition, it is hard to choose a constant step-size which can definitely lead to both bad initialization and poor performance, but which also might be unable to track changing channel state [135–137]. Hence it affects significantly the behaviour of the adaptive equalizer. Therefore, in this section, we present a fully adaptive iterative equalization with a joint phase estimation, using adaptive step-sizes. Similarly to [101, 102, 133], we then apply the obtained results to the underwater case in the difficult case (see section 2.3.1) of doubly selective underwater channels.

4.2.1 The Proposed Adaptive Turbo Equalizer

4.2.1.1 Equalizer Structure

The equalizer structure in this section is the same as the one used in the previous one (see Fig. 4.2), the equalized symbol z_k is given by (4.2), the coefficients of the filters are updated in order to minimize the MSE given by:

$$\begin{aligned} J(\mathbf{f}_k, \mathbf{g}_k, \varphi_k) &= \mathbb{E}_k \left(\mathbb{E}_{x \in \chi | z_k} (|x - z_k|^2) \right) \\ &= \mathbb{E}_k \left(\sum_{x \in \chi} \Pr(x | z_k) |x - z_k|^2 \right), \end{aligned} \quad (4.13)$$

where $\mathbb{E}(d)$ designates the expectation of d , $\mathbb{E}_{x \in \chi | z_k}$ is the expectation given the equalized symbol z_k , and $\Pr(x | z_k)$ can be developed as:

$$\Pr(x | z_k) = \frac{\Pr(x) \Pr(z_k | x)}{\sum_{x' \in \chi} \Pr(x') \Pr(z_k | x')}, \quad (4.14)$$

with (see equation (4.8)):

$$\Pr(z_k | \hat{x}) = \frac{1}{\pi \sigma_v^2} \exp \left(-\frac{|z_k - g_0 \hat{x}|^2}{\sigma_v^2} \right). \quad (4.15)$$

In equation (4.14), we define $A_d = \Pr(d) \Pr(z_k | d)$ where d is a constellation symbol, to simplify the notation.

Note that in contrast to previous works such as [89, 91, 133, 134, 138–140], the MSE is computed over all possible constellation points (see (4.13)) and it encompasses all synchronization modes (Data Aided (DA), Non Data Aided (NDA) and Code Aided (CA)); in particular, for the CA mode, the probability of the constellation point $x \in \chi$ can be computed by the LLR values (see (4.14)) at the output of the channel decoder.

Using the gradient descent algorithm, the filter coefficients \mathbf{f}_k , \mathbf{g}_k and the phase φ_k can be updated as:

$$\begin{cases} \mathbf{f}_{k+1} = \mathbf{f}_k - \frac{\mu}{2} \frac{\partial J}{\partial \mathbf{f}_k}, \\ \mathbf{g}_{k+1} = \mathbf{g}_k - \frac{\mu}{2} \frac{\partial J}{\partial \mathbf{g}_k}, \\ \varphi_{k+1} = \varphi_k - \frac{\gamma}{2} \frac{\partial J}{\partial \varphi_k}. \end{cases} \quad (4.16)$$

The gradient of the J (see equation (4.13)) with respect to the filter coefficients \mathbf{f}_k is:

$$\frac{\partial J}{\partial \mathbf{f}_k} = \sum_{x \in \chi} \left(\frac{\partial \Pr(x | z_k)}{\partial \mathbf{f}_k} |x - z_k|^2 + \Pr(x | z_k) \frac{\partial |x - z_k|^2}{\partial \mathbf{f}_k} \right), \quad (4.17)$$

where (see equation (4.4)):

$$\frac{\partial |x - z_k|^2}{\partial \mathbf{f}_k} = -2(x - z_k) \mathbf{R}_k^* e^{j\varphi_k}, \quad (4.18)$$

and the term $\frac{\partial \Pr(x|z_k)}{\partial \mathbf{f}_k}$ in equation (4.17) can be developed as (see equation (4.14)):

$$\frac{\partial \Pr(x|z_k)}{\partial \mathbf{f}_k} = \frac{\frac{\partial A_x}{\partial \mathbf{f}_k} \sum_{x' \in \chi} A_{x'} - A_x \frac{\partial \sum_{x' \in \chi} A_{x'}}{\partial \mathbf{f}_k}}{\left(\sum_{x' \in \chi} A_{x'} \right)^2}. \quad (4.19)$$

The term $\frac{\partial A_x}{\partial \mathbf{f}_k}$ in equation (4.19) can be developed as:

$$\frac{\partial A_x}{\partial \mathbf{f}_k} = \frac{2A_x}{\sigma_v^2} (g_0 x - z_k) \mathbf{R}_k^* e^{j\varphi_k}. \quad (4.20)$$

In order to simplify the notation, we define $B_x = g_0 x - z_k$ and $C_k = \mathbf{R}_k^* e^{j\varphi_k}$ in equation (4.20).

Similarly to equation (4.20), the term $\frac{\partial \sum_{x' \in \chi} A_{x'}}{\partial \mathbf{f}_k}$ in equation (4.19) can be written as:

$$\frac{\partial \sum_{x' \in \chi} A_{x'}}{\partial \mathbf{f}_k} = \frac{2}{\sigma_v^2} \sum_{x' \in \chi} A_{x'} B_{x'} C_k. \quad (4.21)$$

Finally, equation (4.19) can be rewritten as:

$$\frac{\partial \Pr(x|z_k)}{\partial \mathbf{f}_k} = \Delta_x C_k, \quad (4.22)$$

with:

$$\Delta_x = \frac{2A_x}{\sigma_v^2} \frac{B_x \sum_{x' \in \chi} A_{x'} - \sum_{x' \in \chi} A_{x'} B_{x'}}{\left(\sum_{x' \in \chi} A_{x'} \right)^2}. \quad (4.23)$$

Therefore, the filter coefficients \mathbf{f}_k in equation (4.16) can be updated as:

$$\begin{aligned}\mathbf{f}_{k+1} &= \mathbf{f}_k - \frac{\mu}{2} \frac{\partial J}{\partial \mathbf{f}_k} \\ &= \mathbf{f}_k - \frac{\mu}{2} \sum_{x \in \chi} \left(\Delta_x |x - z_k|^2 - 2 \Pr(x | z_k) (x - z_k) \right) \mathbf{C}_k.\end{aligned}\quad (4.24)$$

Similarly to (4.17-4.24), the filter coefficients \mathbf{g}_k in equation (4.16) are updated as:

$$\begin{aligned}\mathbf{g}_{k+1} &= \mathbf{g}_k - \frac{\mu}{2} \frac{\partial J}{\partial \mathbf{g}_k} \\ &= \mathbf{g}_k + \frac{\mu}{2} \sum_{x \in \chi} \left\{ \Delta_x |x - z_k|^2 - 2 \Pr(x | z_k) (x - z_k) \right\} \tilde{\mathbf{S}}_k^*.\end{aligned}\quad (4.25)$$

Finally, the phase error φ_k in equation (4.16) is updated as:

$$\begin{aligned}\varphi_{k+1} &= \varphi_k - \frac{\gamma}{2} \frac{\partial J}{\partial \varphi_k} \\ &= \varphi_k - \frac{\gamma}{2} \sum_{x \in \chi} \left\{ U_x |x - z_k|^2 - 2 \Pr(x | z_k) \Im(E_x) \right\},\end{aligned}\quad (4.26)$$

where we define:

$$\left\{ \begin{aligned} E_x &= \mathbf{f}_k^T \mathbf{R}_k e^{-j\varphi_k} (x + \mathbf{g}_k^T \tilde{\mathbf{S}}_k)^*, \\ D_x &= E_x - \mathbf{f}_k^T \mathbf{R}_k e^{-j\varphi_k} (1 - g_0) x^*, \\ U_x &= \frac{2A_x}{\sigma_v^2} \frac{\Im(D_x) \sum_{x' \in \chi} A_{x'} - \sum_{x' \in \chi} A_{x'} \Im(D_{x'})}{\left(\sum_{x' \in \chi} A_{x'} \right)^2}.\end{aligned} \right. \quad (4.27)$$

μ and γ in equation (4.24-4.26) are the step-sizes and to be optimized in the next subsection.

4.2.1.2 Adaptive Step-size Optimization

1. Derivation

In contrast to previous works such as [138–141], μ and γ are not constant neither during the training period nor during the tracking period; indeed, they are updated in an adaptive manner so as to minimize the MSE (see (4.13)).

Using the gradient descent algorithm, the step-size μ can be updated as:

$$\mu_{k+1} = \mu_k - \frac{\beta}{2} \frac{\partial J}{\partial \mu}, \quad (4.28)$$

where:

$$\frac{\partial J}{\partial \mu} = \sum_{x \in \chi} \left(\frac{\partial \Pr(x | z_k)}{\partial \mu} |x - z_k|^2 + \Pr(x | z_k) \frac{\partial |x - z_k|^2}{\partial \mu} \right), \quad (4.29)$$

and where:

$$\frac{\partial |x - z_k|^2}{\partial \mu} = 2\Re \left((z_k - x)^* \frac{\partial z_k}{\partial \mu} \right). \quad (4.30)$$

The term $\frac{\partial z_k}{\partial \mu}$ in equation (4.31) can be developed as :

$$\frac{\partial z_k}{\partial \mu} = \mathbf{R}_k e^{-j\varphi_k} \frac{\partial \mathbf{f}_k}{\partial \mu} - \tilde{\mathbf{S}}_k \frac{\partial \mathbf{g}_k}{\partial \mu}. \quad (4.31)$$

Using similar derivation method, we obtain:

$$\frac{\partial \Pr(x | z_k)}{\partial \mu} = \frac{2A_x}{\sigma_v^2} \left(\frac{\Re \left(B_x^* \frac{\partial z_k}{\partial \mu} \right)}{\sum_{x' \in \chi} A_{x'}} - \frac{\sum_{x' \in \chi} A_{x'} \Re \left(B_{x'}^* \frac{\partial z_k}{\partial \mu} \right)}{\left(\sum_{x' \in \chi} A_{x'} \right)^2} \right). \quad (4.32)$$

To simplify the notation, equation (4.32) is noted as: $\frac{\partial \Pr(x | z_k)}{\partial \mu} = \eta_x$.

Finally, the step-size μ_k is updated as (see equation (4.28-4.32)):

$$\mu_{k+1} = \mu_k - \frac{\beta}{2} \sum_{x \in \chi} \left(\eta_x |x - z_k|^2 + 2\Pr(x | z_k) \Re \left((z_k - x)^* \frac{\partial z_k}{\partial \mu} \right) \right). \quad (4.33)$$

The term $\frac{\partial \mathbf{f}_k}{\partial \mu}$ (resp. $\frac{\partial \mathbf{g}_k}{\partial \mu}$) in equation (4.31) noted as F_k (resp. G_k), can be updated adaptively by deriving equation (4.16) with respect to μ as:

$$\frac{\partial \mathbf{f}_{k+1}}{\partial \mu} = \frac{\partial \mathbf{f}_k}{\partial \mu} - \frac{1}{2} \frac{\partial J}{\partial \mathbf{f}_k} - \frac{\mu_k}{2} \frac{\partial \left(\frac{\partial J}{\partial \mathbf{f}_k} \right)}{\partial \mu}, \quad (4.34)$$

and

$$\frac{\partial \mathbf{g}_{k+1}}{\partial \mu} = \frac{\partial \mathbf{g}_k}{\partial \mu} - \frac{1}{2} \frac{\partial J}{\partial \mathbf{g}_k} - \frac{\mu_k}{2} \frac{\partial \left(\frac{\partial J}{\partial \mathbf{g}_k} \right)}{\partial \mu}, \quad (4.35)$$

where the term $\frac{\partial \left(\frac{\partial J}{\partial \mathbf{f}_k} \right)}{\partial \mu}$ in equation (4.34) can be developed as (see equation(4.24)):

$$\frac{\partial \left(\frac{\partial J}{\partial \mathbf{f}_k} \right)}{\partial \mu} = \sum_{x \in \chi} \left(\frac{\partial \Delta x}{\partial \mu} |x - z_k|^2 + \Delta x \frac{\partial |x - z_k|^2}{\partial \mu} - 2 \frac{\partial \Pr(x | z_k)}{\partial \mu} (x - z_k) - 2 \Pr(x | z_k) \frac{\partial (-z_k)}{\partial \mu} \right) C_k, \quad (4.36)$$

and the term $\frac{\partial \left(\frac{\partial J}{\partial \mathbf{g}_k} \right)}{\partial \mu}$ in equation (4.35) can be developed as (see equation(4.25)):

$$\frac{\partial \left(\frac{\partial J}{\partial \mathbf{g}_k} \right)}{\partial \mu} = - \sum_{x \in \chi} \left(\frac{\partial \Delta x}{\partial \mu} |x - z_k|^2 + \Delta x \frac{\partial |x - z_k|^2}{\partial \mu} - 2 \frac{\partial \Pr(x | z_k)}{\partial \mu} (x - z_k) - 2 \Pr(x | z_k) \frac{\partial (-z_k)}{\partial \mu} \right) \tilde{\mathbf{S}}_k^*. \quad (4.37)$$

Furthermore, the term $\frac{\partial \Delta x}{\partial \mu}$ in equation (4.36, 4.37) can be developed as (see equation(4.32)):

$$\begin{aligned} \frac{\partial \Delta x}{\partial \mu} = & \frac{2A_x}{\sigma_v^2 \left(\sum_{x' \in \chi} A' \right)^2} \left(\frac{2}{\sigma_v^2} \left(\Re \left(B_x^* \frac{\partial z_k}{\partial \mu} \right) - \frac{2 \sum_{x' \in \chi} A' \Re \left(B_{x'}^* \frac{\partial z_k}{\partial \mu} \right)}{\sum_{x' \in \chi} A'} \right) \left(B_x \sum_{x' \in \chi} A' - \sum_{x' \in \chi} A' B_{x'} \right) \right. \\ & \left. + \frac{2B_x}{\sigma_v^2} \sum_{x' \in \chi} A' \Re \left(B_{x'}^* \frac{\partial z_k}{\partial \mu} \right) - \sum_{x' \in \chi} A' \frac{\partial z_k}{\partial \mu} - \sum_{x' \in \chi} A' \left(\frac{2B_{x'}}{\sigma_v^2} \Re \left(B_{x'}^* \frac{\partial z_k}{\partial \mu} \right) - \frac{\partial z_k}{\partial \mu} \right) \right). \end{aligned} \quad (4.38)$$

Similar to (4.28-4.38), using the gradient descent algorithm, the step-size γ can be updated as:

$$\gamma_{k+1} = \gamma_k - \frac{\alpha}{2} \frac{\partial J}{\partial \varphi_k} \frac{\partial \varphi_k}{\partial \gamma}, \quad (4.39)$$

where the term $\frac{\partial \varphi_k}{\partial \gamma}$ can be updated as (see equation(4.26)):

$$\frac{\partial \varphi_{k+1}}{\partial \gamma} = \frac{\partial \varphi_k}{\partial \gamma} - \frac{1}{2} \frac{\partial J}{\partial \varphi_k} - \frac{\gamma_k}{2} \frac{\partial \left(\frac{\partial J}{\partial \varphi_k} \right)}{\partial \gamma}, \quad (4.40)$$

and where $\frac{\partial \left(\frac{\partial J}{\partial \varphi_k} \right)}{\partial \gamma}$ can be developed as (see equation(4.26)):

$$\begin{aligned} \frac{\partial \left(\frac{\partial J}{\partial \varphi_k} \right)}{\partial \gamma} = \sum_{x \in \chi} \left\{ \frac{2A_x}{\sigma_v^2} \left(\frac{\left(\frac{2}{\sigma_v^2} \Im^2(D_x) - \Re(D_x) \right)}{\sum_{x' \in \chi} A_{x'}} - \frac{\frac{4}{\sigma_v^2} \Im(D_x) \sum_{x' \in \chi} A_{x'} \Im(D_{x'}) + \sum_{x' \in \chi} A_{x'} \left(\frac{2}{\sigma_v^2} \Im^2(D_{x'}) - \Re(D_{x'}) \right)}{\left(\sum_{x' \in \chi} A_{x'} \right)^2} \right. \right. \\ \left. \left. + \frac{4}{\sigma_v^2} \frac{\left(\sum_{x' \in \chi} A_{x'} \Im(D_{x'}) \right)^2}{\left(\sum_{x' \in \chi} A_{x'} \right)^3} \right) |x - z_k|^2 - 4U_x \Im(E_x) + 2 \Pr(x | z_k) \Re(E_x) \right\} \frac{\partial \varphi_k}{\partial \gamma}. \end{aligned} \quad (4.41)$$

It is worth mentioning that, in contrast to state-of-the-art solutions [89, 134], the proposed adaptive step-sizes are continuously and blindly updated on the whole information burst; this contributes to obtain a good equalization - phase error estimation performance. We should also mention that the step sizes should be constrained to belong to a finite interval where the maximum values prevents the divergence of the algorithm and the minimum value prevents its from staying still [142, 143].

2. Proposal Outline

Gathering the previous results (4.17-4.41), we now summarize the proposed Fully Adaptive (FA) step-size equalizer:

$$z_k = \mathbf{f}_k^T \mathbf{R}_k e^{-j\varphi_k} - \mathbf{g}_k^T \tilde{\mathbf{S}}_k. \quad (4.42)$$

For each iteration k , the values of the filter coefficients \mathbf{f}_k , \mathbf{g}_k and their adaptive step-size μ_k are updated as:

$$\begin{cases} \mathbf{f}_{k+1} = \mathbf{f}_k - \frac{\mu_k}{2} \sum_{x \in \chi} \left(\Delta x |x - z_k|^2 - 2 \Pr(x | z_k) (x - z_k) \right) C_k, \\ \mathbf{g}_{k+1} = \mathbf{g}_k + \frac{\mu_k}{2} \sum_{x \in \chi} \left(\Delta x |x - z_k|^2 - 2 \Pr(x | z_k) (x - z_k) \right) \tilde{\mathbf{S}}_k^*, \\ \mu_{k+1} = \mu_k - \frac{\beta}{2} \sum_{x \in \chi} \left(\eta x |x - z_k|^2 + 2 \Pr(x | z_k) \Re \left(\left(z_k^* - x^* \right) \frac{\partial z_k}{\partial \mu} \right) \right), \\ F_{k+1} = F_k - \frac{1}{2} \frac{\partial J}{\partial \mathbf{f}_k} - \frac{\mu_k}{2} \frac{\partial \left(\frac{\partial J}{\partial \mathbf{f}_k} \right)}{\partial \mu}, \\ G_{k+1} = G_k - \frac{1}{2} \frac{\partial J}{\partial \mathbf{g}_k} - \frac{\mu_k}{2} \frac{\partial \left(\frac{\partial J}{\partial \mathbf{g}_k} \right)}{\partial \mu}. \end{cases} \quad (4.43)$$

Finally, φ_k and its adaptive step-size γ_k are updated as:

$$\begin{cases} \varphi_{k+1} = \varphi_k - \frac{\gamma_k}{2} \sum_{x \in \mathcal{X}} \left\{ U_x |x - z_k|^2 - 2 \Pr(x | z_k) \Im(E_x) \right\}, \\ \gamma_{k+1} = \gamma_k - \frac{\alpha}{2} \sum_{x \in \mathcal{X}} \left\{ U_x |x - z_k|^2 - 2 \Pr(x | z_k) \Im(E_x) \right\} \frac{\partial \varphi_k}{\partial \gamma}, \\ \frac{\partial \varphi_{k+1}}{\partial \gamma} = \frac{\partial \varphi_k}{\partial \gamma} - \frac{1}{2} \frac{\partial J}{\partial \varphi_k} - \frac{\gamma_k}{2} \frac{\partial \left(\frac{\partial J}{\partial \varphi_k} \right)}{\partial \gamma}. \end{cases} \quad (4.44)$$

4.2.2 Simulation Results

In our simulations, source information are coded with a turbo code of rate 1/3 with generator polynomials equal to $(5, 7)_{octal}$; the coded bits are then interleaved and first transformed into a sequence of BPSK symbols. A training sequence of 100 symbols is transmitted before each user frame. At the receiver side, the number of iterations (i.e. equalization/channel decoder) p_{max} is fixed to 10. We consider the synthetic channel given by equation (4.12), we evaluate the performance of our proposal by considering the scenario for which the initial Doppler shift is equal to 0.001 and increases to reach the maximum value $\epsilon_{max} = 0.005$ at the end of the received block. The number of taps for f_k and g_k are equal to 13 and 19 respectively, the central coefficient of f_k is set to 1. It is worth mentioning that for the adaptive step-size equalizer, the values of the second-order step-sizes α and β do not influence considerably the system performance, and can therefore be chosen in a large range.

Fig. 4.6 presents an example of an impulse response over the multipath channel (4.12); it illustrates that the impulse response gradually accelerates, which makes the equalization and phase estimation difficult to achieve with conventional algorithms. Fig. 4.7 and Fig. 4.8 depict the step-size and MSE curves of the proposed fully adaptive step-size algorithm for different iterations, averaged over 1000 Monte Carlo simulations, it can be observed that a maximum of 5 iterations is sufficient to obtain a stability of the adaptive step-size behaviour. Fig. 4.9 (reps. Fig. 4.10) compares the BER performance between the proposed fully adaptive step-size algorithm, the so-called "CS tracking" algorithm for which the step-size is adaptively updated over the preamble, followed by a tracking period with a constant step-size obtained at the end of the (100 symbols) preamble, and finally the algorithm for which the step size is fixed to the initial value $\mu = 0.015$ for all symbols transmitted over the time varying channel (4.12) for the BPSK (resp. QPSK) constellation. We can observe that the conventional algorithm for which the step size remain constant in the tracking period penalizes considerably the overall performance.

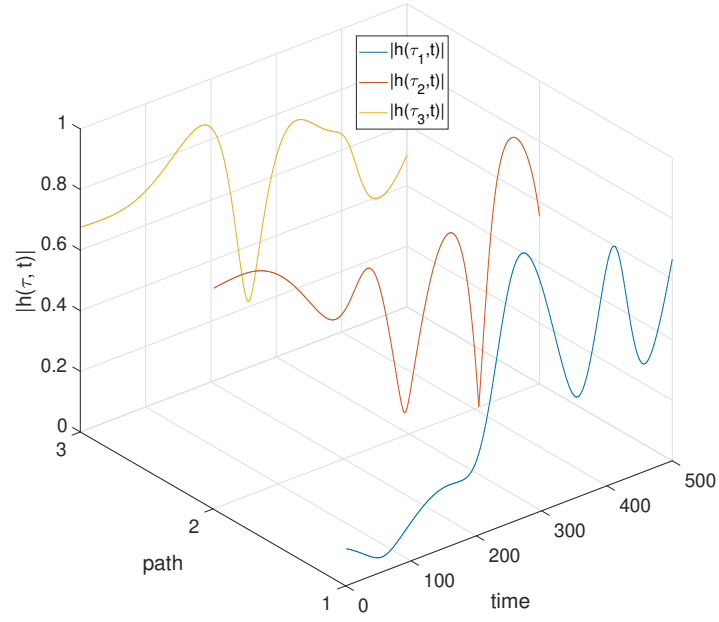


Figure 4.6: Impulse response over the Rayleigh multipath channel (4.12) for $\epsilon_{max} = 0.005$.

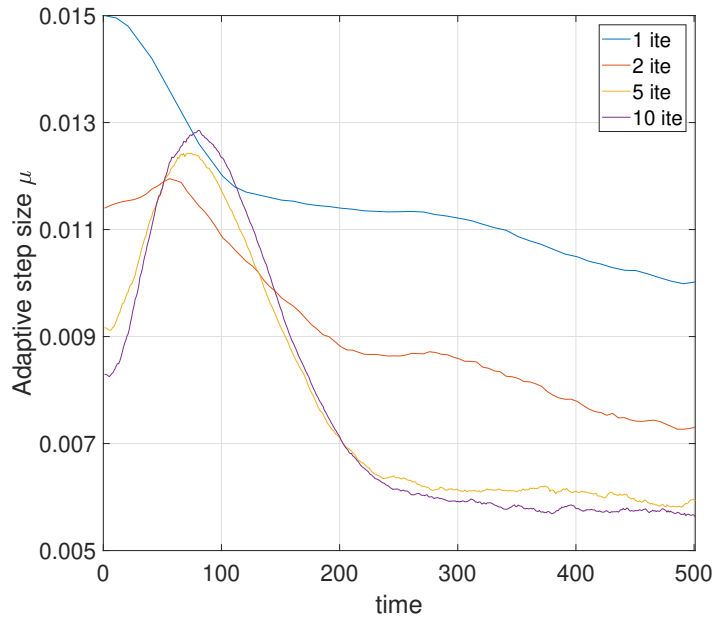


Figure 4.7: Adaptive step-size μ over the channel (4.12) for $\epsilon_{max} = 0.005$ at different iterations and for the BPSK constellation at 6 dB.

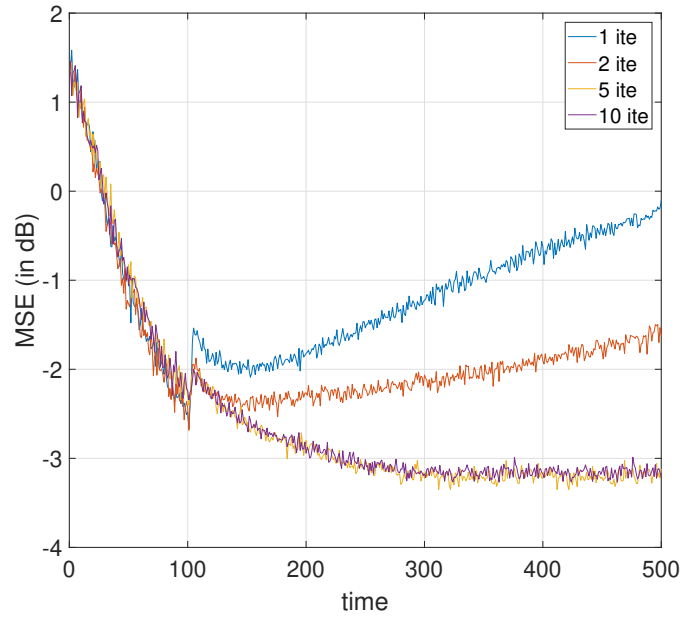


Figure 4.8: MSE curve over the channel (4.12) for $\epsilon_{max} = 0.005$ for the fully adaptive step-size algorithm at different iterations and for the BPSK constellation at 6 dB.

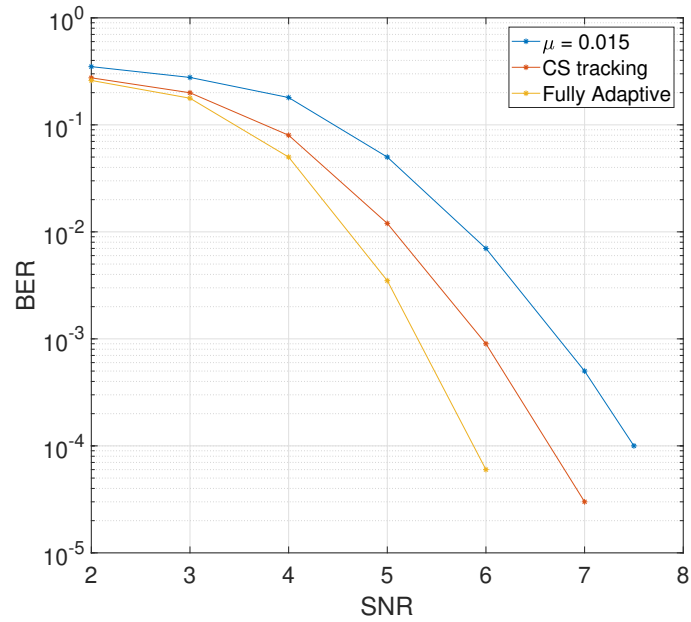


Figure 4.9: BER comparison over the channel (4.12) for $\epsilon_{max} = 0.005$ and for the BPSK constellation

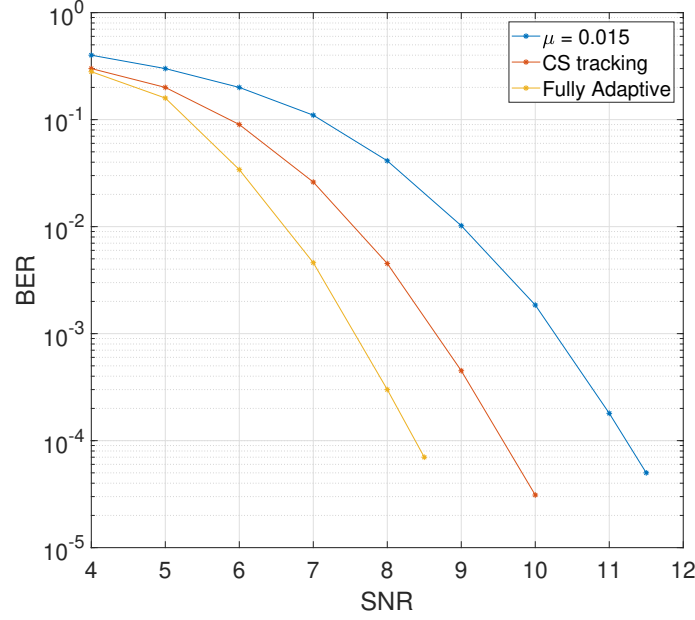


Figure 4.10: BER comparison over the channel (4.12) for $\epsilon_{max} = 0.005$ and for the QPSK constellation

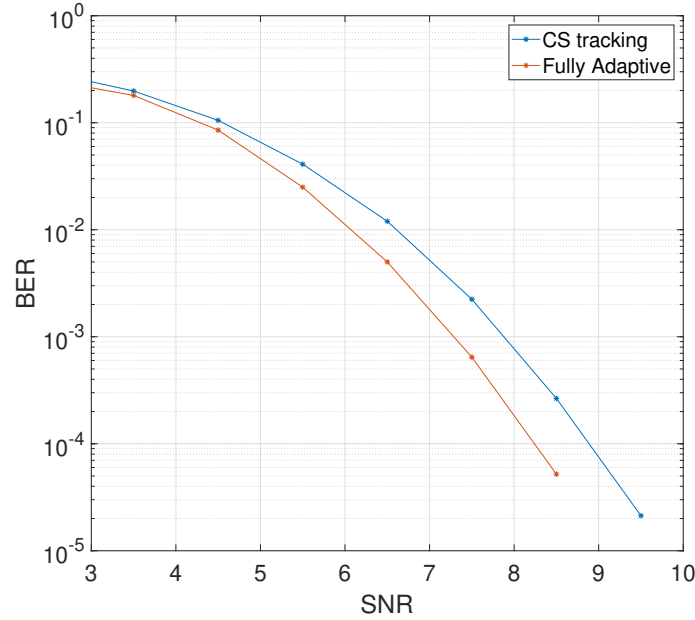


Figure 4.11: BER comparison between the fully adaptive step-size algorithm and the CS tracking one over the channel BCH1 of Watermark for the QPSK constellation.

For example at a $BER = 10^{-4}$, it can be observed for the BPSK (resp. QPSK) constellation on Fig. 4.9 (resp. Fig. 4.10) that the proposed fully adaptive step-size algorithm achieves roughly a 0.8 dB (resp. 1.3 dB) BER performance

gain compared to the CS tracking algorithm and the CS tracking algorithm achieves around a 1 dB (resp. 1.6 dB) BER performance gain compared to the algorithm for which the step-size μ is fixed to $\mu = 0.015$ for all symbols transmitted. This is a positive result for a channel that can be considered as difficult (see chapter 2). Finally, Fig. 4.11 compares the BER performance for the fully adaptive step-size algorithm and the CS tracking one over the channel BCH1 of the Watermark simulator for the QPSK constellation; it can be observed that the proposed fully adaptive step-size algorithm has an advantage of about 0.6 dB. The gain is smaller than the one observed on the synthetic channel because BCH1 is not a fast-varying channel.

4.3 Conclusion

In this chapter, a fully adaptive low complexity joint iterative channel equalization and channel decoding process is first proposed; indeed, with this proposal, only a small number of coefficients need to be updated. The equalizer was successfully tested over Rayleigh time-varying and over some recorded multipath underwater channels. The good performance and the simplicity of our proposal make it very attractive for practical implementation, in particular for underwater communication systems for which a large number of taps is usually needed.

This chapter also proposes a new joint equalizer - phase estimator algorithm with adaptive step-sizes. It leads to good BER performance by achieving a good trade-off between the convergence speed and MSE minimization over time-varying channels. Simulation results of our proposals show a significant BER improvement compared to the conventional solutions currently used in practice for doubly selective channels with high and varying Doppler shifts.

General Conclusion

In a context where bandwidth is limited, the environment is dynamic and communications systems operate outside a standardized framework, the realization of the IoT and its need of low complexity algorithms and energy efficiency, is particularly difficult. The research work of this thesis, in the context of the underwater acoustic channel that is time and frequency selective, focused on the study of low-complexity rotated constellations and adaptive turbo equalization. Indeed, rotated constellations allow better performance than the conventional ones and adaptive turbo equalization algorithm is effective in removing ISI over multi-paths channels. These techniques nevertheless suffer from several limitations and this thesis, therefore, consisted in proposing practical solutions to overcome those limitations.

We started by presenting in detail the main characteristics of the underwater acoustic channel and the general model of a digital communication transmission chain. We then introduced OFDM modulation and we noted its large PAPR problem and its impact on the energy efficiency of the transmitter. We illustrated that diversity is a factor that considerably affects the performance of wireless communication systems over fading channels. We then presented the rotated constellations with its inherent diversity and described several methods proposed in the literature for the selection of the rotation angle as well as for the soft demodulation of the rotated signals. In addition, we have formalized the equalization problem and underlined the impact of this task over the overall performance of communication systems. The main contributions of this thesis with regard to the objectives set are contained in the following chapters.

Chapter 3 first reviewed the properties of the UP-RCQD constellations that enables to design a low- complexity demapper for fading channels that gives almost the same performance as the Max-Log algorithm. We have also underlined the good performances of these constellations: indeed, the UP-RCQD constellations allow better performances on several underwater acoustic channels. In addition, we have proposed a PAPR reduction method for OFDM systems testing several two-dimensional interleavers and a single rotation angle ; the best OFDM symbol in terms of PAPR reduction is selected on the transmitter side and the index of the two-dimensional interleaver is not sent to the receiver in order

to preserve the spectral efficiency of the system. Unlike conventional constellations, the receiver is able to identify the interleaver used with the Max-Log estimator that we have proposed. In addition, we again relied on the structural properties of the UP-RCQD constellations in order to design a low complexity estimator; it is able to reduce the complexity of estimating the interleaver index by more than 98% compared to the Max-Log solution.

Finally, in the last chapter, we first proposed a fully adaptive low-complexity joint iterative channel equalization and channel decoding process. Indeed, for our proposal, a sparse adaptive turbo detector with only a small number of coefficient updates is proved on one side, to enable a large reduction of the overall computational complexity by more than 60% and, on the other side, to achieve better performance compared to the conventional one, which makes the low complexity equalizer suited for real-time processing. Furthermore, we proposed an original adaptive step-size iterative MSE equalizer where the soft-information exchanged between the equalizer and the channel decoder can also be used for adjusting the adaptive step-size, as it is an appealing indicator of the symbol reliability. The proposed algorithm for joint phase recovering and equalization allows fast convergence, a better tracking performance over time varying channel and a lower mean square error compared to the constant step-size case.

Perspectives

A short-term objective is to develop adaptive step-size algorithms for synchronization and for channel estimation. In this thesis, we have focused on the case of two-dimensional rotated constellations. Middle term objectives concern further development of those rotated constellations.

On one side, it seems interesting to design a particular rotation matrix for the multidimensional case, which would give similar properties to that of UP-RCQD constellations. The design of a low-complexity soft demapper for this case would then be possible in a similar way.

On the other side, dedicated signal processing algorithms, such as channel attenuation estimation or synchronization, should specifically be adapted to the special case of rotated constellations. They are still to be invented and could take advantage of the particular a priori of this type of modulation.

Finally a long-term objective is to develop a platform to test those algorithms in a real environment and then have them embarked on real autonomous objects.

Résumé

La terre est recouverte d'environ 70% d'eau et environ 95% des océans et 99% des fonds marins restent inexplorés. En d'autres termes, la majeure partie de notre planète bleue et de ses ressources reste à découvrir. D'une certaine manière, l'hostilité de l'environnement sous-marin a intrinsèquement protégé ce monde secret jusqu'à récemment. Mais l'intérêt pour le monde marin, illustré d'une part par le lien entre la fonte arctique et la montée des eaux et d'autre part par la compétition pour l'exploitation des ressources énergétiques sous-marines, ouvre la question éthique de savoir comment trouver un équilibre satisfaisant entre les besoins toujours croissants de l'humanité et la fragilité de notre écosystème face à une population humaine toujours plus nombreuse.

Les recherches visant à comprendre le milieu sous-marin et à exploiter ses riches ressources ont conduit à l'essor de l'exploration sous-marine à des fins d'abord militaires, puis scientifiques et économiques. Pour être en mesure d'observer, de surveiller et d'explorer les océans, nous pouvons utiliser des observatoires des fonds marins, des réseaux de capteurs ou des véhicules sous-marins, soit télécommandés (Remotely Operated Vehicles - ROV), soit autonomes (Autonomous Underwater Vehicles - AUV).

Tous ces systèmes d'exploration et d'observation nécessitent des moyens de communication avec la surface pour l'instrumentation et le contrôle, ou pour le transfert de données. En milieu sous-marin, cette communication peut être réalisée par voie filaire au moyen de câbles (mais souvent équipés de fibre optique) ; c'est le cas des observatoires filaires comme NEPTUNE (Ifremer) situé sur le plateau tectonique de Juan de Fuca, au large du Canada. C'est également le cas des ROVs pour lesquels l'ombilical est utilisé pour contrôler le robot et récupérer les données acquises. L'intérêt de la communication par câble réside dans sa vitesse (jusqu'à plusieurs PetaBits/s pour les câbles sous-marins intercontinentaux) et sa très faible latence, cependant, son prix est très élevé (jusqu'à 600 k€/km) et la maintenance de tels systèmes est complexe. En outre, la communication filaire pose de sérieux problèmes de mobilité, comme on l'a observé avec les ROVs.

Une autre approche est la communication sous-marine sans fil qui ne nécessite pas de lien physique entre l'émetteur et le récepteur, et donc un coût d'installation et de maintenance plus faible. Cependant, comme nous le verrons dans la

suite, la fiabilité et le taux de transmission sont plus faibles par rapport à la communication filaire. Pour transmettre des informations sans fil dans un environnement sous-marin, les supports classiques sont les ondes de radiofréquence, les ondes optiques et enfin les ondes acoustiques.

Les ondes RF sont très fortement atténuées par l'eau (de l'ordre de 3 à 5 dB/m selon la fréquence), elles nécessitent donc une puissance de transmission élevée et/ou des transducteurs de grande taille. Les communications RF sous-marines peuvent donc être intéressantes pour transmettre à haut débit (de l'ordre du Mbit/s) sur une très courte distance (jusqu'à 10 m). A plus haute fréquence, les ondes optiques permettent de communiquer à très haut débit (jusqu'à quelques Gbit/s) mais subissent rapidement des phénomènes de diffusion et d'absorption dus à l'eau (1 dB/m et jusqu'à 11 dB/m en eau trouble) limitant la portée de la communication à quelques dizaines de mètres. L'alignement des faisceaux lumineux entre l'émetteur et la réception est également un problème important pour ces systèmes de communication. L'intérêt des ondes optiques se révèle lorsque l'on souhaite transférer rapidement un grand volume de données sur une courte distance, notamment au moyen de robots sous-marins.

Enfin, les ondes acoustiques subissent une atténuation relativement faible dans l'eau (de l'ordre de 0,1 à 4 dB/km) et permettent de communiquer sur des distances relativement importantes (de quelques kilomètres à plusieurs centaines de kilomètres). Ceci a contribué à faire des ondes acoustiques, le vecteur de transmission le plus utilisé dans un environnement sous-marin. Les communications acoustiques sous-marines sont cependant fortement perturbées par les atténuations des ondes acoustiques, le bruit, le phénomène des trajets multiples, l'étalement temporel du canal, et enfin par l'effet Doppler. Tous ces effets combinés rendent le canal acoustique sous-marin unique puisqu'il est variable dans le temps, la fréquence et l'espace limitant ainsi les débits de transmission (selon la fréquence) à quelques dizaines de kbit/s par kilomètre. Enfin, la vitesse des ondes sonores dans l'eau (environ 1500 m/s en fonction de divers paramètres physiques) entraîne une latence importante dans la communication.

Les techniques modernes de communications acoustiques sous-marines ont commencé à être développées à des fins militaires pendant la Seconde Guerre mondiale. En 1945, le premier système de communication sous-marine a vu le jour aux États-Unis d'Amérique afin d'établir une liaison de communication entre les sous-marins. Ce premier modem utilisait la modulation Single Side Band (SSB) dans la bande de fréquence 8 - 11 kHz pour une distance de plusieurs kilomètres. Jusqu'à la fin des années 1970, d'autres modems acoustiques ont été référencés dans la littérature, tous basés sur des techniques de transmission analogiques, ce qui constitue une sérieuse limitation face aux distorsions apportées par le canal acoustique sous-marin. A partir des années 1980, avec le développement des circuits électroniques hautement intégrés, Very-Large-Scale Integration (VLSI) et l'avènement des processeurs DSP compacts à consommation réduite, il est devenu possible d'implémenter, au sein des émetteurs/récepteurs immergés, des algorithmes complexes de traitement du signal ouvrant la voie aux technologies de transmission numérique. Ainsi,

au cours de ces quarante dernières années, des progrès considérables ont été réalisés dans le développement des modems acoustiques, tant en termes de portée de communication que de vitesse de transmission.

Dans cette thèse, nous nous intéressons au contexte scientifique du projet européen H2020 appelé Bridges pour lequel les laboratoires UME et U2IS de l'ENSTA Paris ont tous deux été impliqués. Dans ce projet, un planeur (un AUV plutôt non coûteux de moins de 2 mètres de long) navigue et échange des informations avec différents capteurs déployés dans un cercle d'environ moins de 1 km de rayon. Dans ce contexte d'Internet des objets (IoT) sous-marin, nous nous concentrons sur les problèmes de communication numérique soulevés par l'environnement acoustique et nous gardons ainsi à l'esprit que la complexité est un problème clé pour ces objets autonomes économes en énergie.

Dans un contexte où la bande passante est limitée, l'environnement est dynamique et les systèmes de communication fonctionnent en dehors d'un cadre standardisé, la réalisation de l'IoT et son besoin d'algorithmes à faible complexité et d'efficacité énergétique, est particulièrement difficile. Les travaux de recherche de cette thèse, dans le contexte du canal acoustique sous-marin sélectif en temps et en fréquence, se sont focalisés sur l'étude des constellations tournantes à faible complexité et de la turbo égalisation adaptative. En effet, les constellations tournantes permettent d'obtenir de meilleures performances que les constellations conventionnelles et l'algorithme de turbo égalisation adaptative est efficace pour supprimer l'ISI sur les canaux multi-trajets. Ces techniques souffrent néanmoins de plusieurs limitations et cette thèse a donc consisté à proposer des solutions pratiques pour surmonter ces limitations.

Nous avons commencé par présenter en détail les principales caractéristiques du canal acoustique sous-marin. Le chapitre 1 rappelle les propriétés de l'environnement de propagation sous-marine. Nous passons en revue les dégradations apportées par le canal à grande et petite échelle et leur impact sur les canaux de communication. Nous illustrons également la double sélectivité du canal acoustique.

L'objectif d'un système de communication numérique est de transmettre des informations des émetteurs aux récepteurs, sous forme de symboles ou de bits binaires, à un rythme généralement mesuré en symboles ou en bits par seconde. Cette transmission s'effectue dans un environnement qui dicte les lois de propagation des ondes qui transportent les signaux d'information. Ces signaux correspondent aux symboles contenant l'information et occupent une largeur de bande déterminée dans le spectre des fréquences, autour d'une ou plusieurs fréquences porteuses. L'environnement physique est appelé canal de communication. Les canaux de communication ont une capacité exprimée en nombre de symboles par seconde qui peuvent être transmis avec un taux d'erreur arbitrairement bas. Lorsqu'une communication est établie par un canal, une certaine ressource physique de ce canal est utilisée : typiquement, une certaine bande de fréquences est utilisée par un système pendant une certaine période de temps. L'un des principaux problèmes lors de la conception de réseaux de communication est le partage des ressources disponibles pour établir des transmissions

fiables entre chaque élément du réseau. Lorsque plusieurs systèmes non coopératifs se disputent l'utilisation d'une ressource, ils interfèrent au détriment de leur robustesse et de leur fiabilité.

Outre le cas des très courtes distances (moins de 100 m), les ondes électromagnétiques ne sont pas adaptées aux communications sous-marines, car l'eau est un milieu conducteur qui absorbe rapidement la majeure partie de l'énergie transmise. En revanche, les propriétés physiques du milieu sous-marin permettent aux ondes acoustiques de se propager sur de longues distances. Les ondes acoustiques sous-marines sont donc le support privilégié des signaux de communication dans cet environnement. Cependant, la physique se présente également comme un facteur limitant les performances des modems de communication acoustique sous-marine qui fonctionnent à des débits de données très faibles par rapport aux modems à radiofréquence. Ces différences de performance reflètent les différences en ordres de grandeur entre certains paramètres physiques de base des deux milieux de propagation. Par exemple, le rapport entre la vitesse de l'onde électromagnétique dans l'air et celle de l'onde acoustique sous-marine est de 10^5 ($3 \cdot 10^8$ m/s contre environ 1500 m/s, respectivement). La fréquence porteuse des communications RF peut atteindre quelques gigahertz (10^9 Hz), alors que pour les communications acoustiques sous-marines, elle ne dépasse pas quelques dizaines de kilohertz. La bande passante dans ce milieu est strictement limitée, surtout lorsque la distance de transmission augmente. Par conséquent, le canal de communication acoustique sous-marin est souvent considéré comme étant à large bande, la fréquence porteuse et la largeur de la bande de transmission ayant le même ordre de grandeur. La limite de performance actuelle des modems acoustiques sous-marins se traduit par un produit vitesse de transmission-distance généralement inférieur à $40 \text{ kbits/s} \times \text{km}$. D'une part, en raison du manque d'interopérabilité, et d'autre part, en raison du manque de ressources disponibles pour communiquer sans interférence entre les utilisateurs, la coexistence de sources acoustiques d'origines différentes dans le même canal est également difficile. Ceci, couplé aux longs délais de propagation, entraîne des difficultés dans la conception de protocoles fiables et efficaces adaptés aux réseaux de communication. Enfin, l'environnement sous-marin présente une variabilité et une hétérogénéité à plusieurs échelles spatiales et temporelles, ce qui nécessite une certaine flexibilité et la capacité d'adapter les modems acoustiques sous-marins à l'environnement dynamique dans lequel ils fonctionnent.

L'objectif du premier chapitre est de présenter en détail les particularités de l'environnement acoustique sous-marin, considéré comme le canal de communication, afin de permettre au lecteur de mieux comprendre les différentes hypothèses de travail qui seront présentées dans les chapitres suivants. Tout d'abord, les propriétés physiques importantes du canal acoustique sous-marin sont introduites, puis la distorsion subie par le signal de communication sous-marin est expliquée en détail. Le canal de communication acoustique sous-marin est souvent présenté comme difficile, en raison de ses caractéristiques physiques et des hétérogénéités du milieu. Ces difficultés sont l'une des principales raisons pour lesquelles le développement des communications acoustiques sous-marines a été plus lent que celui des

communications par radiofréquence, car les techniques utilisées dans ce domaine ne peuvent être transposées directement au milieu sous-marin. La large bande du canal, les différentes échelles de variabilité de l'environnement, ainsi que l'absence de protocoles de réseau normalisés et d'infrastructures pour organiser l'accès au canal, posent de grands défis. Le chapitre suivant rappelle comment les systèmes de communications numériques tentent de relever ces défis.

Le chapitre 2 est un chapitre classique qui synthétise plusieurs solutions de communication numérique pour faire face aux dégradations de canaux. Nous avons d'abord rappelé quelques bases élémentaires des communications numériques, puis présenté les principales caractéristiques des canaux à évanouissement. Ce chapitre présente le modèle général d'une chaîne de communication numérique et précise le cadre dans lequel ce travail de thèse a été mené.

La première section présente les composants de la chaîne de transmission et ce chapitre s'intéresse tout d'abord aux paramètres de l'émetteur. La modulation d'amplitude en quadrature (QAM) numérique est d'abord utilisée comme véhicule de l'information numérique à travers le canal de transmission. Le démodulateur cohérent est utilisé dans la suite de ce travail. La partie suivante de ce chapitre introduit la modulation OFDM (Orthogonal Frequency Division Multiplexing) et le problème du PAPR (Peak-to-Average Power Ratio) est présenté. En général, les signaux provenant de plusieurs trajets peuvent s'additionner de manière constructive ou destructive ; les canaux à évanouissement sont donc peu fiables, ce qui rend nécessaire l'utilisation de techniques de diversité. De plus, lorsque la liaison est sélective en fréquence, le signal transmis sur ce type de canal suit des trajets différents pour arriver au récepteur sur des symboles successifs, une égalisation côté récepteur est donc nécessaire. Enfin, ce chapitre présente plusieurs égaliseurs proposés dans la littérature, l'algorithme LMS, l'égaliseur MMSE et la turbo égalisation. La troisième section de ce chapitre illustre comment un système de communication numérique fait face à la dégradation du canal, le concept de diversité est introduit et la dernière section présente le concept d'égalisation.

Dans le troisième chapitre, nous développons davantage un angle spécial pour obtenir la diversité des signaux. Cette diversité de signaux ne gâche aucune ressource du canal, ce qui est particulièrement intéressant pour le canal acoustique sous-marin pour lequel la bande passante est particulièrement limitée.

Le canal acoustique sous-marin varie dans le temps et sa bande passante est particulièrement limitée. Cela rend difficile l'établissement de communications fiables et limite le taux d'information. La constellation tournée est une technique efficace qui économise à la fois la bande passante et l'énergie, car elle permet de tirer parti de la diversité du canal et donc d'améliorer les performances des constellations tournées sur certains canaux à évanouissement tels que les canaux acoustiques sous-marins. Cependant, le coût réel de cette technique est la grande complexité de la démodulation qui a empêché son utilisation à grande échelle. Pour faire face à ce problème, ce chapitre propose de se concentrer sur la modulation M-QAM en utilisant une série d'angles de rotation $\theta = \arctan(1/\sqrt{M})$ qui introduit plusieurs

propriétés structurelles pouvant être utilisées pour faciliter considérablement le processus de démodulation.

Comme nous l'avons montré au chapitre 2, les constellations tournées apportent une diversité inhérente à un système sans perte de spectre. La norme DVB-T2 a été la première norme industrielle à utiliser des constellations M-QAM tournées qui, en théorie, donnent de meilleurs résultats que les constellations M-QAM classiques sur les canaux à évanouissement. Néanmoins, cette solution augmente considérablement la complexité du côté du récepteur. En effet, les démodulateurs bidimensionnels proposés dans la littérature ont une complexité de calcul élevée qui a un impact non négligeable sur la conception du récepteur.

Dans la première section, nous avons étudié une série d'angles de rotation $\theta = \arctan\left(1/\sqrt{M}\right)$ présentant des propriétés structurelles intéressantes pour différents signaux RCQD (Rotated and Cyclically Q-Delayed). Sur la base de ces propriétés, nous avons étudié un démodulateur à faible complexité pour les canaux à évanouissement qui donne presque les mêmes performances que l'algorithme optimal Max-Log. Grâce aux bonnes performances des angles proposés et à la simplicité de la mise en œuvre du démodulateur proposé, l'efficacité spectrale et la consommation d'énergie du système de communication sous-marin peuvent être améliorées. Il est important de noter que la diversité inhérente du signal explorée sans expansion de la bande passante pourrait à son tour économiser encore plus de bande passante en permettant l'utilisation d'un code de canal à plus haut débit. En s'appuyant sur celles-ci, nous détaillerons un démodulateur de faible complexité dédié à ces angles et le testerons sur deux canaux sous-marins.

Comme nous l'avons rappelé au chapitre 2, la solution OFDM peut être une alternative aux communications sous-marines monoporteuses pour les canaux stables à courte portée (quelques centaines de mètres) ; en effet, sa bonne efficacité spectrale est payée au prix d'une grande sensibilité aux problèmes de synchronisation et de PAPR. Le PAPR élevé des signaux OFDM entraîne une sérieuse dégradation des performances du système, ce qui limite en particulier la portée de la communication.

Pour contourner ce problème, plusieurs algorithmes ont été proposés dans la littérature (voir chapitre 2) pour réduire la PAPR, mais ils souffrent souvent de multiples limitations ; en particulier, le principal problème des techniques d'entrelacement est la perte d'efficacité spectrale, car la transmission d'une information latérale (SI) est généralement requise.

Contrairement aux travaux précédents, cette section propose une technique d'entrelacement aveugle pour les systèmes OFDM avec diversité d'espace de signal (SSD). En effet, avec les constellations RCQD, les composantes en phase (I) et en quadrature (Q) des symboles de constellations sont corrélées, ce qui permet au récepteur d'estimer l'indice d'entrelacement sans aucun SI. De plus, pour réduire la charge de complexité du côté du récepteur, nous concevons d'abord un décodeur aveugle basé sur le critère d'erreur quadratique moyenne minimale (MMSE), puis nous proposons un décodeur à faible complexité pour la QAM à projection uniforme RCQD (UP-RCQD), car nous

avons montré dans la première partie de ce chapitre que cette constellation possède plusieurs propriétés structurelles intéressantes et permet d'obtenir des performances de taux d'erreur binaire (TEB) presque optimales.

La deuxième section propose une nouvelle technique d'entrelacement aveugle pour la réduction du PAPR sans aucune distorsion pour les systèmes OFDM utilisant la diversité d'espace de signal. Elle est basée sur l'utilisation de constellations tournantes car elles permettent au récepteur d'identifier, sans aucun SI, l'entrelaceur à deux composantes utilisé dans la diffusion. Pour réduire la charge de complexité du côté du récepteur, un détecteur basé sur le MMSE avec de bonnes performances est proposé. De plus, afin de réduire encore plus la complexité de calcul du démappeur, nous proposons d'utiliser à nouveau la constellation UP-RCQD car cette constellation apporte de nombreuses propriétés structurelles intéressantes que nous employons pour concevoir un décodeur d'index d'entrelacement à faible complexité. Les principaux avantages de cette technique sont les suivants. Notre proposition permet d'obtenir une réduction importante du PAPR sans dégradation du TEB, ni altération spectrale. En outre, par rapport à la méthode SLM aveugle, la technique proposée simplifie la conception de l'émetteur et du récepteur et sa faible complexité la rend particulièrement adaptée à une mise en œuvre matérielle.

Le chapitre 4 est consacré au problème de l'égalisation. Le canal sous-marin est l'un des canaux les plus difficiles car le signal acoustique peut souffrir à la fois d'une largeur de bande de cohérence très limitée et d'un effet Doppler élevé. En particulier, la propagation par trajets multiples introduit une ISI qui peut sérieusement limiter les performances du système. Après la découverte du turbo-décodage, l'égalisation itérative a été proposée pour éliminer l'ISI, car l'égaliseur et le décodeur de canal peuvent échanger mutuellement des informations extrinsèques à chaque itération afin d'améliorer leurs performances. La récupération de la phase est encore un autre problème auquel le récepteur doit faire face, en particulier dans le cas d'une importante dérive Doppler. Néanmoins, la complexité du schéma théorique de turbo égalisation croît exponentiellement avec les paramètres de communication, ce qui interdit son utilisation dans des applications réelles. Comme la réponse impulsionnelle du canal peut être très longue en raison de la célérité relativement faible des ondes acoustiques, nous proposons un égaliseur sparse avec récupération de phase conjointe. De plus, pour un canal dont les caractéristiques varient dans le temps, les algorithmes conventionnels de turbo égalisation utilisant des pas constants sont incapables, par construction, d'atteindre des performances de poursuite satisfaisantes et donc un bon compromis entre la performance et la vitesse de convergence, donc nous présentons également une architecture entièrement adaptative avec une taille de pas adaptative. Pour faire face à ces problèmes, ce chapitre présente deux algorithmes différents et originaux pour l'égalisation et l'estimation de phase conjointes. Il est divisé en deux sections principales.

La première section propose un détecteur turbo adaptatif sparse avec seulement quelques taps à mettre à jour afin de réduire la charge de complexité. Elle est organisée comme suit : la première sous-section présente le modèle de

système d'égalisation turbo adaptatif ; ensuite, la structure de l'égaliseur adaptatif est présentée dans la deuxième sous-section, l'analyse détaillée de la complexité de l'algorithme et la performance TEB de l'algorithme proposé sur les canaux sous-marins et un canal synthétique sont données dans la dernière sous-section.

Nous avons d'abord proposé un processus d'égalisation et de décodage de canal itératif conjoint entièrement adaptatif et à faible complexité. En effet, pour notre proposition, un détecteur turbo adaptatif sparse avec seulement un petit nombre de mises à jour de coefficients s'est avéré, d'une part, permettre une réduction importante de la complexité de calcul globale de plus de 60% et, d'autre part, obtenir de meilleures performances par rapport au détecteur conventionnel, ce qui rend l'égaliseur à faible complexité adapté au traitement en temps réel. L'égaliseur a été testé avec succès sur des canaux de Rayleigh variant dans le temps et sur certains canaux sous-marins à trajets multiples enregistrés. Les bonnes performances et la simplicité de notre proposition la rendent très intéressante pour une mise en œuvre pratique, en particulier pour les systèmes de communication sous-marins pour lesquels un grand nombre de prises est généralement nécessaire.

Jusqu'à présent, notre objectif était de considérer des algorithmes peu complexes pour les applications de l'Internet des objets. En particulier, l'algorithme standard d'égalisation itérative est souvent utilisé dans l'estimation en temps réel grâce à sa faible complexité. Cependant, les performances de cette technique dépendent de sa taille de pas constante ; en particulier, la taille de pas contrôle à la fois la vitesse de convergence et l'erreur quadratique moyenne en régime permanent de l'algorithme ; si la taille de pas est choisie trop petite, la vitesse de convergence est trop lente, mais si elle est choisie trop grande, l'erreur quadratique moyenne en régime permanent est faible. En outre, il est difficile de choisir une taille de pas constante qui peut certainement conduire à une mauvaise initialisation et à des performances médiocres, mais qui pourrait également être incapable de suivre l'évolution de l'état du canal. Cela affecte donc de manière significative le comportement de l'égaliseur adaptatif. Par conséquent, dans cette section, nous présentons une égalisation itérative entièrement adaptative avec une estimation de phase conjointe, en utilisant des pas adaptatifs. Nous appliquons ensuite les résultats obtenus au cas sous-marin dans le cas difficile des canaux sous-marins doublement sélectifs.

La deuxième section de ce chapitre propose un égaliseur original auto-optimisé pour lequel les pas de l'égaliseur et de l'estimateur de phase sont mis à jour de manière adaptative et assistés par des informations souples fournies par le décodeur de canal de manière itérative. Cette deuxième section est organisée comme suit : la première sous-section détaille l'algorithme de la technique proposée et décrit le fonctionnement de l'égaliseur proposé ; certains résultats de simulation sont présentés dans la sous-section suivante.

Il convient de noter que, contrairement aux travaux précédents, l'erreur quadratique moyenne est calculée sur tous les points de constellation possibles et englobe tous les modes de synchronisation (Data Aided (DA), Non Data Aided

(NDA) et Code Aided (CA)); en particulier, pour le mode CA, la probabilité du point de constellation peut être calculée par les valeurs LLR à la sortie du décodeur de canal. Contrairement aux travaux précédents, les tailles de pas ne sont pas constantes, ni pendant la période d'apprentissage, ni pendant la période de suivi ; en effet, elles sont mises à jour de manière adaptative afin de minimiser l'erreur quadratique moyenne. Il convient de mentionner que, contrairement aux solutions de pointe, les tailles de pas adaptatives proposées sont mises à jour de manière continue et aveugle sur l'ensemble de la salve d'informations, ce qui contribue à obtenir de bonnes performances en matière d'égalisation et d'estimation des erreurs de phase. Nous devrions également mentionner que les tailles de pas devraient être contraintes à appartenir à un intervalle fini où les valeurs maximales empêchent la divergence de l'algorithme et la valeur minimale l'empêche de rester immobile.

Le nouvel algorithme conjoint d'égaliseur et d'estimateur de phase avec des pas adaptatifs permet d'obtenir de bonnes performances en termes de TEB en réalisant un bon compromis entre la vitesse de convergence et la minimisation de l'erreur quadratique moyenne sur des canaux variant dans le temps. Les résultats de simulation de nos propositions montrent une amélioration significative du TEB par rapport aux solutions conventionnelles actuellement utilisées dans la pratique pour les canaux doublement sélectifs avec des décalages Doppler élevés et variables.

Bibliography

- [1] Pierre-Jean Bouvet. *Communications acoustiques pour les réseaux sous-marins sans fils*. Habilitation à diriger des recherches, UBO Brest, November 2020.
- [2] A. Quazi and W. Konrad. Underwater acoustic communications. *IEEE Communications Magazine*, 20(2):24–30, Mar. 1982.
- [3] D. B. Kilfoyle and A. B. Baggeroer. The state of the art in underwater acoustic telemetry. *IEEE Journal of Oceanic Engineering*, 25(1):4–27, Jan. 2000.
- [4] Herman Medwin and Clarence S. Clay. *Fundamentals of Acoustical Oceanography*. Applications of Modern Acoustics. Academic Press, San Diego, 1998.
- [5] Antony Pottier. *Méthodes décentralisées d'allocation des ressources dans le canal d'interférence acoustique sous-marin*. Theses, Ecole nationale supérieure Mines-Télécom Atlantique, Nov. 2018.
- [6] Xavier Lurton. *An Introduction to Underwater Acoustics: Principles and Applications*. Springer, 2010.
- [7] Robert J. Urick. *Principles of Underwater Sound 3rd Edition*. Peninsula Pub, 1983.
- [8] Lurton Xavier. *Acoustique sous-marine : présentation et applications*. Ifremer, Bibliothèque de Brest, 1998.
- [9] Coates R.F.W. *Noise and Reverberation*. In: *Underwater Acoustic Systems*. Palgrave, London, 1990.
- [10] R. S. Alford O. Knudsen and J. W. Emling. Underwater ambient noise. *Journal of Marine Research*, 1948.
- [11] R.J. Urick and United States. Naval Sea Systems Command. Undersea Warfare Technology Office. *Ambient Noise in the Sea*. Undersea Warfare Technology Office, Naval Sea Systems Command, Department of the Navy, 1984.
- [12] Gordon M. Wenz. Review of underwater acoustics research: Noise. *The Journal of the Acoustical Society of America*, 51(1010), 1972.

- [13] M. Stojanovic and J. Preisig. Underwater acoustic communication channels: Propagation models and statistical characterization. *IEEE Communications Magazine*, 47(1):84–89, Feb. 2009.
- [14] A. Mahmood, M. Chitre, and M. A. Armand. PSK communication with passband additive symmetric α -stable noise. *IEEE Transactions on Communications*, 60(10):2990–3000, Jul. 2012.
- [15] G. Loubet, J.L. Lacoume, B. Faure, and F. Vial. Effet de la dispersion sur la propagation acoustique sous-marine. *Journal de Physique Colloques*, 51(C2):C2–945–C2–948, Feb. 1990.
- [16] Robert G. Gallager. *Principles of Digital Communication*. Cambridge University Press, 2008.
- [17] Proakis. *Digital Communications 5th Edition*. McGraw Hill, 2007.
- [18] B. S. Sharif, J. Neasham, O. R. Hinton, and A. E. Adams. A computationally efficient doppler compensation system for underwater acoustic communications. *IEEE Journal of Oceanic Engineering*, 25(1):52–61, Jan. 2000.
- [19] P. Bello. Characterization of randomly time-variant linear channels. *IEEE Transactions on Communications Systems*, 11(4):360–393, Dec. 1963.
- [20] P. V. Walree. Channel sounding for acoustic communications : techniques and shallow-water examples. Norwegian Defence Research Establishment (FFI), Apr. 2011.
- [21] F.X. Socheleau, C. Laot, and J. Passerieux. Stochastic replay of non-wssus underwater acoustic communication channels recorded at sea. *IEEE Transactions on Signal Processing*, 59(10):4838–4849, Jun. 2011.
- [22] P. Qarabaqi and M. Stojanovic. Statistical characterization and computationally efficient modeling of a class of underwater acoustic communication channels. *IEEE Journal of Oceanic Engineering*, 38(4):701–717, Sep. 2013.
- [23] P. A. van Walree and R. Otnes. Ultrawideband underwater acoustic communication channels. *IEEE Journal of Oceanic Engineering*, 38(4):678–688, Jun. 2013.
- [24] Wen-Bin Yang and Tsih Yang. High-frequency channel characterization for M-ary frequency-shift-keying underwater acoustic communications. *Acoustical Society of America Journal*, 120:2615–, 11 Nov. 2006.
- [25] I. Boyd and R.L. Brownell. *The Effects of Anthropogenic Sound on Marine Mammals: A Draft Research Strategy*. ESF Marine Board position paper. European Science Foundation. Marine Board, 2008.
- [26] McCarthy. *International Regulation Of Underwater Sound : Establishing Rules and Standards to Address Ocean Noise Pollution*. Kluwer Academic Publishers, 2004.

- [27] CMRE PAO. *JANUS, the CMRE underwater communication protocol, becomes a NATO Standard*. Centre for Maritime Research Experimentation NATO, April 2017.
- [28] J. Potter, J. Alves, D. Green, G. Zappa, I. Nissen, and Kim McCoy. The janus underwater communications standard. *2014 Underwater Communications and Networking (UComms)*, pages 1–4, Sept. 2014.
- [29] Christophe Vanstraceele. *Turbo codes et estimation paramétrique pour les communications à haut débit*. Theses, École normale supérieure de Cachan - ENS Cachan, January 2005.
- [30] Tarak Arbi. *Les constellations tournées pour les réseaux sans fil et l'internet des objets sous-marins*. Theses, Institut Polytechnique de Paris, February 2020.
- [31] Richard van Nee and Ramjee Prasad. *OFDM for Wireless Multimedia Communications*. Artech House, USA, 1st edition, 2000.
- [32] C. E. Shannon. Communication in the presence of noise. *Proceedings of the IRE*, 37(1):10–21, Jan. 1949.
- [33] J. Yang, B. Geller, and T. Arbi. Proposal of a multi-standard transceiver for the wban internet of things. In *2016 International Symposium on Signal, Image, Video and Communications (ISIVC)*, pages 369–373, 2016.
- [34] J. Yang, B. Geller, and T. Arbi. Récepteur multi-normes pour les réseaux de capteurs de l'iot médical. *Internet des objets*, 2017.
- [35] T. Arbi and B. Geller. Multi-standard receiver for medical iot sensor networks. In *Challenges of the internet of things : technique, use, ethics*, Wiley-ISTE, pages 105–121, 2018.
- [36] H. Sari, G. Karam, and I. Jeanclaude. Transmission techniques for digital terrestrial tv broadcasting. *IEEE Communications Magazine*, 33(2):100–109, Feb. 1995.
- [37] Y. Liu, X. Chen, Z. Zhong, B. Ai, D. Miao, Z. Zhao, J. Sun, Y. Teng, and H. Guan. Waveform design for 5g networks: Analysis and comparison. *IEEE Access*, 5:19282–19292, Feb. 2017.
- [38] Jorge Luis Gulfo Monsale. *GreenOFDM a new method for OFDM PAPR reduction*. Theses, Université Grenoble Alpes, Oct. 2019.
- [39] T. Jiang and Y. Wu. An overview: Peak-to-average power ratio reduction techniques for ofdm signals. *IEEE Transactions on Broadcasting*, 54(2):257–268, May. 2008.
- [40] P. P. Ann and R. Jose. Comparison of papr reduction techniques in ofdm systems. In *2016 International Conference on Communication and Electronics Systems (ICCES)*, pages 1–5, Oct. 2016.

- [41] Zhuo Wang, Enchang Sun, and Yanhua Zhang. An overview of peak-to-average power ratio reduction techniques for ofdm signals. *International Journal of Mobile Network Communications Telematics*, 6:1–20, Jun. 2016.
- [42] D. Lim, S. Heo, and J. No. An overview of peak-to-average power ratio reduction schemes for ofdm signals. *Journal of Communications and Networks*, 11(3):229–239, Jun. 2009.
- [43] Hangjun Chen and A. Haimovich. An iterative method to restore the performance of clipped and filtered ofdm signals. In *IEEE International Conference on Communications*, volume 5, pages 3438–3442, May. 2003.
- [44] T. G. Pratt, N. Jones, L. Smee, and M. Torrey. Ofdm link performance with companding for papr reduction in the presence of non-linear amplification. *IEEE Transactions on Broadcasting*, 52(2):261–267, Jun. 2006.
- [45] T. Jiang, W. Xiang, P. C. Richardson, D. Qu, and G. Zhu. On the nonlinear companding transform for reduction in papr of mcm signals. *IEEE Transactions on Wireless Communications*, 6(6):2017–2021, Aug. 2007.
- [46] Tao Jiang, Yang Yang, and Yong-Hua Song. Exponential companding technique for papr reduction in ofdm systems. *IEEE Transactions on Broadcasting*, 51(2):244–248, May. 2005.
- [47] A. E. Jones, T. A. Wilkinson, and S. K. Barton. Block coding scheme for reduction of peak to mean envelope power ratio of multicarrier transmission schemes. *Electronics Letters*, 30(25):2098–2099, Dec. 1994.
- [48] D. Wulich. Reduction of peak to mean ratio of multicarrier modulation using cyclic coding. *Electronics Letters*, 32(5):432–, 1996.
- [49] A. D. S. Jayalath and C. Tellambura. Slm and pts peak-power reduction of ofdm signals without side information. *IEEE Transactions on Wireless Communications*, 4(5):2006–2013, Nov. 2005.
- [50] J. Ji, G. Ren, and H. Zhang. A semi-blind slm scheme for papr reduction in ofdm systems with low-complexity transceiver. *IEEE Transactions on Vehicular Technology*, 64(6):2698–2703, Jun. 2015.
- [51] M. Sghaier, F. Abdelkefi, and M. Siala. Efficient embedded signaling through rotated modulation constellations for slm-based ofdm systems. In *2013 IEEE International Conference on Communications (ICC)*, pages 5252–5256, Jun. 2013.
- [52] A. Boonkajay and F. Adachi. 2-step phase rotation estimation for low-papr signal transmission using blind selected mapping. In *2017 IEEE 28th Annual International Symposium on Personal, Indoor, and Mobile Radio Communications (PIMRC)*, pages 1–5, Oct. 2017.

- [53] A. D. S. Jayalath and C. Tellambura. The use of interleaving to reduce the peak-to-average power ratio of an ofdm signal. In *Globecom '00 - IEEE. Global Telecommunications Conference. Conference Record (Cat. No.00CH37137)*, volume 1, pages 82–86 vol.1, Nov. 2000.
- [54] H. Ryu, S. Kim, and S. Ryu. Interleaving method without side information for the papr reduction of ofdm system. In *2007 International Symposium on Communications and Information Technologies*, pages 72–76, Oct. 2007.
- [55] S. Y. Le Goff, S. S. Al-Samahi, B. K. Khoo, C. C. Tsimenidis, and B. S. Sharif. Selected mapping without side information for papr reduction in ofdm. *IEEE Transactions on Wireless Communications*, 8(7):3320–3325, Jul. 2009.
- [56] S. S. K. C. Bulusu, M. Crussière, J.F. Héland, R. Mounzer, Y. Nasser, O. Rousset, and A. Untersee. Quasi-optimal tone reservation papr reduction algorithm for next generation broadcasting systems: A performance/complexity/latency tradeoff with testbed implementation. *IEEE Transactions on Broadcasting*, 64(4):883–899, Dec. 2018.
- [57] N. Jacklin and Z. Ding. A linear programming based tone injection algorithm for papr reduction of ofdm and linearly precoded systems. *IEEE Transactions on Circuits and Systems I: Regular Papers*, 60(7):1937–1945, Mar. 2013.
- [58] K. Bae, J. G. Andrews, and E. J. Powers. Adaptive active constellation extension algorithm for peak-to-average ratio reduction in ofdm. *IEEE Communications Letters*, 14(1):39–41, Jan. 2010.
- [59] R. van Nee and R. Prasad. *OFDM for Wireless Multimedia Communications*. Artech House Universal Persona. Artech House, 2000.
- [60] Bernard Sklar. *Digital Communications: Fundamentals and Applications, 2nd Edition*. Pearson Education, 2001.
- [61] David Tse and Pramod Viswanath. *Fundamentals of Wireless Communication*. Cambridge University Press, 2005.
- [62] K. Boulle and J. Belfiore. Modulation schemes designed for the rayleigh channel. 1992.
- [63] J. Boutros and E. Viterbo. Signal space diversity: a power- and bandwidth-efficient diversity technique for the rayleigh fading channel. *IEEE Transactions on Information Theory*, 44(4):1453–1467, Jul. 1998.
- [64] J. Boutros, E. Viterbo, C. Rastello, and J. . Belfiore. Good lattice constellations for both rayleigh fading and gaussian channels. *IEEE Transactions on Information Theory*, 42(2):502–518, Mar. 1996.

- [65] Catherine Lamy. *Communications à grande efficacité spectrale sur le canal à évanouissements*. Theses, Télécom ParisTech, Apr. 2000.
- [66] Mohammad Ali Khalighi and Laurent Ros. Delayed two-streams division, a diversity technique to improve signal transmission in relatively fast flat fading channels. *Signal Processing*, 85(4):705–715, Apr. 2005.
- [67] S. Benedetto, E. Biglieri, and V. Castellani. *Digital Transmission Theory*. Prentice-Hall, 1987.
- [68] X. Giraud, E. Boutillon, and J. C. Belfiore. Algebraic tools to build modulation schemes for fading channels. *IEEE Transactions on Information Theory*, 43(3):938–952, May. 1997.
- [69] M. N. Khormuji, U. H. Rizvi, G. J. M. Janssen, and S. B. Slimane. Rotation optimization for MPSK/MQAM signal constellations over rayleigh fading channels. In *2006 10th IEEE Singapore International Conference on Communication Systems*, pages 1–5, Nov. 2006.
- [70] J. Kim and I. Lee. Analysis of symbol error rates for signal space diversity in rayleigh fading channels. In *2008 IEEE International Conference on Communications*, pages 4621–4625, May. 2008.
- [71] Q. Xie, J. Song, K. Peng, F. Yang, and Z. Wang. Coded modulation with signal space diversity. *IEEE Transactions on Wireless Communications*, 10(2):660–669, Feb. 2011.
- [72] C. Abdel Nour and C. Douillard. Rotated QAM constellations to improve bicm performance for DVB-T2. In *2008 IEEE 10th International Symposium on Spread Spectrum Techniques and Applications*, pages 354–359, Aug. 2008.
- [73] A. Abdmouleh, E. Boutillon, L. Conde-Canencia, C. A. Nour, and C. Douillard. On signal space diversity for non binary coded modulation schemes. In *2016 23rd International Conference on Telecommunications (ICT)*, pages 1–5, May. 2016.
- [74] S. Jeon, J. Choi, Z. Yim, and J. Seo. Error floor analysis of signal space diversity schemes under erasure effect in single frequency network. *IEEE Transactions on Broadcasting*, 58(3):508–513, Sep. 2012.
- [75] J. Kim, W. Lee, J. . Kim, and I. Lee. On the symbol error rates for signal space diversity schemes over a rician fading channel. *IEEE Transactions on Communications*, 57(8):2204–2209, Aug. 2009.
- [76] N. Tran, H. Nguyen, and T. Le-Ngoc. Performance analysis and design criteria of bicm-id with signal space diversity for keyhole nakagami-m fading channels. *IEEE Transactions on Information Theory*, 55:1592–1602, Mar. 2009.

- [77] N. H. Tran, H. H. Nguyen, and Tho Le-Ngoc. Application of signal space diversity over multiplicative fading channels. In *2008 24th Biennial Symposium on Communications*, pages 221–225, Mar. 2009.
- [78] *Digital Video Broadcasting (DVB); frame structure, channel coding and modulation for a second generation digital terrestrial television broadcasting system (DVB-T2)*. European Tele. Standard Institute ETSI Yotk EN 302 755 VI.1.1., Sep. 2009.
- [79] *Implementation guidelines for a second generation digital terrestrial television broadcasting system (DVB-T2)*. European Telecom. Standard Institute ETSI TR 102 831 VI.1.1, Oct. 2010.
- [80] M. Li, C. Abdel Nour, C. Jégo, J. Yang, and C. Douillard. Efficient iterative receiver for bit-interleaved coded modulation according to the DVB-T2 standard. In *2011 IEEE International Conference on Acoustics, Speech and Signal Processing (ICASSP)*, pages 3168–3171, May. 2011.
- [81] Kyeongyeon Kim, Kitaek Bae, and Ho Yang. One-dimensional soft-demapping using decorrelation with interference cancellation for rotated QAM constellations. In *2012 IEEE Consumer Communications and Networking Conference (CCNC)*, pages 787–791, Jan. 2012.
- [82] M. Li, C. A. Nour, C. Jégo, and C. Douillard. Design of rotated QAM mapper/demapper for the DVB-T2 standard. In *2009 IEEE Workshop on Signal Processing Systems*, pages 018–023, Oct. 2009.
- [83] S. Tomasin and M. Butussi. Low complexity demapping of rotated and cyclic q delayed constellations for DVB-T2. *IEEE Wireless Communications Letters*, 1(2):81–84, Apr. 2012.
- [84] D. Perez-Calderon, V. Baena-Lecuyer, A. C. Oria, P. Lopez, and J. G. Doblado. Simplified rotated constellation demapper for second generation terrestrial digital video broadcasting. *IEEE Transactions on Broadcasting*, 59(1):160–167, Mar. 2013.
- [85] J. Yang, M. Li, M. Li, C. A. Nour, C. Douillard, and B. Geller. Max-log demapper architecture design for DVB-T2 rotated QAM constellations. In *2015 IEEE Workshop on Signal Processing Systems (SiPS)*, pages 1–6, Oct. 2015.
- [86] Peng Xue, Kitaek Bae, Kyeongyeon Kim, and Ho Yang. \sqrt{M} -best candidates based soft-demapper for rotated m-QAM constellation. *2014 IEEE 11th Consumer Communications and Networking Conference (CCNC)*, pages 623–628, Jan. 2014.
- [87] Mohammad-Ali Khalighi and Laurent Ros. Delayed two-streams division, a diversity technique to improve signal transmission in relatively fast flat fading channels. *Signal Processing*, 85:705–715, 2005.

- [88] Gregory E. Bottomley. *Channel Equalization for Wireless Communications: From Concepts to Detailed Mathematics*. Wiley-IEEE Press, 1st edition, 2011.
- [89] C. Laot, A. Glavieux, and J. Labat. Turbo equalization: adaptive equalization and channel decoding jointly optimized. *IEEE Journal on Selected Areas in Communications*, 19(9):1744–1752, Sep. 2001.
- [90] Catherine Douillard, Michel Jezequel, Claude Berrou, Annie Picart, and Pierre Didier. Iterative correction of intersymbol interference: turbo-equalization. *European Transactions on Telecommunications*, 6(5):507–512, Sep. 1995.
- [91] M. Tuchler, R. Koetter, and A. C. Singer. Turbo equalization: principles and new results. *IEEE Transactions on Communications*, 50(5):754–767, May. 2002.
- [92] T. Arbi, B. Geller, J. Yang, C. Abdel Nour, and O. Rioul. Uniformly projected rcqd QAM: A low-complexity signal space diversity solution over fading channels with or without erasures. *IEEE Transactions on Broadcasting*, 64(4):803–815, Dec. 2018.
- [93] B. Hassibi and H. Vikalo. On the sphere-decoding algorithm I. Expected complexity. *IEEE Transactions on Signal Processing*, 53(8):2806–2818, Aug. 2005.
- [94] P. A. van Walree, F.X. Socheleau, R. Otnes, and T. Jenserud. The watermark benchmark for underwater acoustic modulation schemes. *IEEE Journal of Oceanic Engineering*, 42(4):1007–1018, Oct. 2017.
- [95] Z. Ye, T. Arbi, F.X. Socheleau, and B. Geller. Fast soft demapping for underwater acoustic communications with signal space diversity. In *OCEANS 2018 MTS/IEEE Charleston*, pages 1–6, Dec. 2018.
- [96] T. Arbi, Z. Ye, and B. Geller. Low-complexity blind papr reduction for ofdm systems with rotated constellations. In *IEEE Transactions on Broadcasting*, Accepted Dec. 2020.
- [97] T. Arbi and B. Geller. Joint ber optimization and blind papr reduction of ofdm systems with signal space diversity. *IEEE Communications Letters*, 23(10):1866–1870, Jul. 2019.
- [98] T. Arbi, I. Nasr, and B. Geller. Near capacity rcqd constellations for papr reduction of ofdm systems. In *ICASSP 2020 - 2020 IEEE International Conference on Acoustics, Speech and Signal Processing (ICASSP)*, pages 5110–5114, May. 2020.
- [99] Y. A. Jawhar, L. Audah, M. A. Taher, K. N. Ramli, N. S. M. Shah, M. Musa, and M. S. Ahmed. A review of partial transmit sequence for papr reduction in the ofdm systems. *IEEE Access*, 7:18021–18041, Feb. 2019.

- [100] Z. Ye, T. Arbi, and B. Geller. Low complexity adaptive turbo equalization for multipath underwater communication. In *OCEANS 2019 - Marseille*, pages 1–5, Jun. 2019.
- [101] B. Geller, J. M. Broissier, and V. Capellano. Equalizer for high data rate transmission in underwater communications. In *Proceedings of OCEANS'94*, volume 1, pages I/302–I/306 vol.1, Sept. 1994.
- [102] B. Geller, V. Capellano, and G. Jourdain. Equalizer for real time high rate transmission in underwater communications. In *1995 International Conference on Acoustics, Speech, and Signal Processing*, volume 5, pages 3179–3182 vol.5, May. 1995.
- [103] W. Ryan and S. Lin. *Channel Codes: Classical and Modern*. Cambridge University Press, 2009.
- [104] C. Berrou. *Codes and turbo codes*. Collection IRIS. Springer Paris, 2011.
- [105] S. Lin and D.J. Costello. *Error Control Coding: Fundamentals and Applications*. Pearson education. Pearson-Prentice Hall, 2004.
- [106] T.K. Moon. *Error Correction Coding: Mathematical Methods and Algorithms*. Wiley, 2005.
- [107] Richard E. Blahut. *Algebraic Codes on Lines, Planes, and Curves: An Engineering Approach*. Cambridge University Press, 2008.
- [108] E. Arikan. Channel polarization: A method for constructing capacity-achieving codes for symmetric binary-input memoryless channels. *IEEE Transactions on Information Theory*, 55(7):3051–3073, Jul. 2009.
- [109] R. M. Pyndiah. Near-optimum decoding of product codes: block turbo codes. *IEEE Transactions on Communications*, 46(8):1003–1010, Aug. 1998.
- [110] J. Yang, B. Geller, C. Herzet, and J.M. Brossier. Smoothing PLLs for QAM dynamical phase estimation. In *IEEE International Conference on Communications*, pages 1–5, Jun. 2009.
- [111] Diatta, D. De Geest, and B. Geller. Reed solomon turbo codes for high data rate transmission. In *2004 IEEE 59th Vehicular Technology Conference. VTC 2004-Spring (IEEE Cat. No.04CH37514)*, volume 2, pages 1023–1027 Vol.2, 2004.
- [112] D. D. Falconer. Jointly adaptive equalization and carrier recovery in two-dimensional digital communication systems. *The Bell System Technical Journal*, 55(3):317–334, Mar. 1976.
- [113] U. Mengali. *Synchronization Techniques for Digital Receivers*. Applications of Communications Theory. Springer US, 1997.

- [114] I. Nasr, L. Najjar Atallah, S. Cherif, and B. Geller. Near map dynamical delay estimator and bayesian crb for coded QAM signals. *IEEE Transactions on Wireless Communications*, 17(1):636–651, Jan. 2018.
- [115] F.M. Gardner. *Demodulator Reference Recovery Techniques Suited for Digital Implementation*. Gardner Research Comp., 1988.
- [116] I. Nasr, B. Geller, L. Najjar Atallah, and S. Cherif. Performance study of a near maximum likelihood code-aided timing recovery technique. *IEEE Transactions on Signal Processing*, 64(3):799–811, Feb. 2016.
- [117] I. Nasr, L. Najjar Atallah, S. Cherif, B. Geller, and J. Yang. A soft maximum likelihood technique for time delay recovery. In *Fourth International Conference on Communications and Networking, ComNet-2014*, pages 1–5, Mar. 2014.
- [118] H. Meyr and G. Ascheid. *Synchronization in Digital Communications, Volume 1: Phase-, Frequency-Locked Loops, and Amplitude Control*. Wiley Series in Telecommunications and Signal Processing. Wiley, 1990.
- [119] R. Best. *Costas Loops: Theory, Design, and Simulation*. Springer International Publishing, 2017.
- [120] J.M. Brossier, P.O. Amblard, and B. Geller. Self-adaptive PLL for general QAM constellations. In *2002 11th European Signal Processing Conference*, pages 1–4, Sept. 2002.
- [121] C. Herzet, N. Noels, V. Lottici, H. Wymeersch, M. Luise, M. Moeneclaey, and L. Vandendorpe. Code-aided turbo synchronization. *Proceedings of the IEEE*, 95(6):1255–1271, Jun. 2007.
- [122] J. Yang and B. Geller. Near optimum low complexity smoothing loops for dynamical phase estimation—application to BPSK modulated signals. *IEEE Transactions on Signal Processing*, 57(9):3704–3711, Sept. 2009.
- [123] Fuyun Ling and John Proakis. *Synchronization in Digital Communication Systems*. Cambridge University Press, 2017.
- [124] B. Geller, I. Diatta, J. P. Barbot, C. Vanstraceele, and F. Rambeau. Block turbo codes: From architecture to application. In *2006 IEEE International Symposium on Information Theory*, pages 1813–1816, Jul. 2006.
- [125] B. Geller. Advanced synchronization techniques for the internet of things. In *2016 International Symposium on Signal, Image, Video and Communications (ISIVC)*, pages 180–184, Nov. 2016.
- [126] R. A. Fisher. On the mathematical foundations of theoretical statistics. *Philosophical Transactions of the Royal Society of London. Series A, Containing Papers of a Mathematical or Physical Character*, 222:309–368, 1934.

- [127] H.L. Van Trees and K.L. Bell. *Bayesian Bounds for Parameter Estimation and Nonlinear Filtering/Tracking*. Wiley, 2007.
- [128] S. Bay, C. Herzet, J.M. Brossier, J.P. Barbot, and B. Geller. Analytic and asymptotic analysis of bayesian cramér–rao bound for dynamical phase offset estimation. *IEEE Transactions on Signal Processing*, 56(1):61–70, Jan. 2008.
- [129] J. Yang, B. Geller, and S. Bay. Bayesian and hybrid cramér–rao bounds for the carrier recovery under dynamic phase uncertain channels. *IEEE Transactions on Signal Processing*, 59(2):667–680, Feb. 2011.
- [130] Steven M. Kay. *Fundamentals of Statistical Processing, Volume I: Estimation Theory*. Prentice-Hall, USA, 1993.
- [131] S. Bay, B. Geller, A. Renaux, J.P. Barbot, and J.M. Brossier. On the hybrid cramér rao bound and its application to dynamical phase estimation. *IEEE Signal Processing Letters*, 15:453–456, May. 2008.
- [132] J. Yang, B. Geller, and A. Wei. Approximate expressions for cramer-rao bounds of code aided QAM dynamical phase estimation. In *2009 IEEE International Conference on Communications*, pages 1–5, Jun. 2009.
- [133] B. Geller, V. Capellano, J.M. Broissier, A. Essebbar, and G. Jourdain. Equalizer for video rate transmission in multipath underwater communications. *IEEE Journal of Oceanic Engineering*, 21(2):150–155, Apr. 1996.
- [134] C. Laot and R. L. Bidan. Adaptive mmse turbo equalization with high-order modulations and spatial diversity applied to underwater acoustic communications. In *17th European Wireless 2011 - Sustainable Wireless Technologies*, pages 1–6, Apr. 2011.
- [135] Albert Benveniste, Pierre Priouret, and Michel Métivier. *Adaptive Algorithms and Stochastic Approximations*. Springer-Verlag, Berlin, Heidelberg, 1990.
- [136] R. H. Kwong and E. W. Johnston. A variable step size lms algorithm. *IEEE Transactions on Signal Processing*, 40(7):1633–1642, Jul. 1992.
- [137] T. Aboulnasr and K. Mayyas. A robust variable step-size lms-type algorithm: analysis and simulations. *IEEE Transactions on Signal Processing*, 45(3):631–639, Mar. 1997.
- [138] B. Benammar, N. Thomas, C. Poulliat, M. Boucheret, and M. Dervin. On linear mmse based turbo-equalization of nonlinear volterra channels. In *2013 IEEE International Conference on Acoustics, Speech and Signal Processing*, pages 4703–4707, May. 2013.

- [139] J. W. Choi, T. J. Riedl, K. Kim, A. C. Singer, and J. C. Preisig. Adaptive linear turbo equalization over doubly selective channels. *IEEE Journal of Oceanic Engineering*, 36(4):473–489, Oct. 2011.
- [140] H. Lou and C. Xiao. Soft-decision feedback turbo equalization for multilevel modulations. *IEEE Transactions on Signal Processing*, 59(1):186–195, Jan. 2011.
- [141] M. Tüchler and A. C. Singer. Turbo equalization: An overview. *IEEE Transactions on Information Theory*, 57(2):920–952, Feb. 2011.
- [142] R. Gerzaguet, L. Ros, F. Belveze, and J.M. Brossier. On multiplicative update with forgetting factor adaptive step size for least mean-square algorithms. In *2018 25th International Conference on Telecommunications (ICT)*, pages 588–592, Jun. 2018.
- [143] S. B. Gelfand, Yongbin Wei, and J. V. Krogmeier. The stability of variable step-size lms algorithms. *IEEE Transactions on Signal Processing*, 47(12):3277–3288, Dec. 1999.

Titre: Traitement statistique de l'information et du signal pour l'internet des objets sous-marins

Mots clés: algorithmes adaptatifs, communications numériques sans fil, communications acoustiques sous-marines

Résumé: On assiste au développement des activités humaines liées au monde océanique, mais aucune norme n'a encore émergé pour l'Internet des objets appliqué aux objets autonomes marins. Bien qu'elle possède une bande passante limitée, l'onde acoustique est le seul moyen de communiquer sur des distances importantes et elle est donc utilisée par de nombreux systèmes sous-marins pour communiquer, naviguer ou déduire des informations sur l'environnement. Cela a conduit à une forte demande de réseaux sans fil qui nécessitent à la fois une bonne efficacité spectrale et énergétique avec la faible complexité des algorithmes associés. Par conséquent, au cours de ce doctorat, nous avons proposé plusieurs solutions originales pour relever le défi de développer des techniques numériques, capables de faire face au canal acoustique.

En raison d'une diversité inhérente d'espace du signal (SSD), les constellations tournées permettent de meilleures performances théoriques que les constellations conventionnelles et ce, sans détérioration

spectrale. Nous passons en revue les propriétés structurelles des constellations tournées M-QAM uniformément projetées, afin de proposer une technique de demapping souple à faible complexité pour les canaux à fading. Puis, nous proposons une technique originale de réduction du PAPR pour les systèmes OFDM utilisant les constellations tournées. Afin de réduire la complexité du décodage aveugle, nous nous appuyons sur les propriétés des constellations tournées M-QAM uniformément projetées, pour concevoir un estimateur de faible complexité. De plus, pour faire face à la sélectivité du canal acoustique, nous avons proposé un turbo-détecteur parcimonieux adaptatif avec seulement quelques coefficients à mettre à jour afin de réduire la complexité. Enfin, nous avons proposé un algorithme original auto-optimisé pour lequel les tailles de pas de l'égaliseur sont mises à jour de manière adaptative et assistées par des informations souples de manière itérative, afin de répondre à l'exigence de convergence rapide et de faible erreur quadratique sur des canaux variant rapidement dans le temps.

Title: Statistical information and signal processing for the underwater internet of things.

Keywords: adaptive algorithms, wireless digital communications, underwater acoustic communications

Abstract: There has been recently a large development of human activities associated with the ocean world, where no standard has emerged for the Internet of Things (IoT) linked to marine autonomous objects. Though it has a limited bandwidth, the acoustic wave is the only way to communicate over average to large distances and it is thus used by many underwater systems to communicate, navigate, or infer information about the environment. This led to high demand for wireless networks that require both spectral efficiency and energy efficiency with the associated low-complexity algorithms. Therefore, in this Ph.D. thesis, we proposed several original solutions to face this challenge.

Indeed, due to the inherent Signal Space Diversity (SSD), rotated constellations allow better theoretical performance than conventional constellations with no spectral spoilage. We review the structural properties of uniformly projected rotated M-QAM constellations, so

as to propose a low complexity soft demapping technique for fading channels. Then, we present an original blind technique for the reduction of the PAPR for OFDM systems using the rotated constellations with SSD. In order to reduce the complexity of blind decoding for this technique, we again rely on the properties of uniformly projected M-QAM rotated constellations to design a low-complexity estimator. Moreover, to face the selectivity of the acoustic channel, we suggest a sparse adaptive turbo detector with only a few taps to be updated in order to lower down the complexity burden. Finally, we have proposed an original self-optimized algorithm for which the step-sizes of both the equalizer and the phase estimator are updated adaptively and assisted by soft-information in an iterative manner, so as to meet the requirement of fast convergence and low MSE over time-varying channels.